Modelling Gamma-Ray Absorption at Cosmic Distances

Ayman Mohamed Eladi Mohamed Kudoda

School of Physics

University of the Witwatersrand

A thesis submitted for the degree of

Doctor of Philosophy

2018

Declaration

I declare that this Theses '*Modelling Gamma-Ray Absorption at Cosmic Distances'* is my own, unaided work. It is being submitted for the Degree of Doctor of Philosophy in Physics at the University of the Witwatersrand, Johannesburg. It has not been submitted before for any degree or examination at any other University.

List of publications during the PhD

- Kudoda A. M., Faltenbacher A., 2017, MNRAS, 467, 2896 - presented in Chapter 3
- Kudoda A. M., Faltenbacher A., 2018, MNRAS, 481, 405 - presented in Chapter 4
- Kudoda A. M., Faltenbacher A., 2017, The Proceedings of SAIP2017, the 62^{nd} Annual Conference of the SAIP, 62 , 252

The work presented in Chapter 3 is an extension of my master work titled *'Modelling the Inhomogeneities of the Extragalactic Background Light'* submitted in August 2015.

I declare that this thesis has not been submitted to any university for a degree, and work in this thesis save for that which is properly acknowledged is my own.

Ayman Kudoda,

Abstract

Extragalactic background light (EBL) is the integrated light from all resolved and unresolved extragalactic sources since the recombination era. Its spectrum extends from infrared to ultraviolet ($0.001-10\,\mathrm{eV}$). Due to the expansion of the Universe photons emitted from early structures, that are not observable yet individually with the current technology, are redshifted to longer wavelengths in the EBL regime. These photons, therefore, carry a wealth of information about the formation and evolution of the Universe. Studying these photons is crucial in understanding the different stages the Universe went through. In addition, low energy EBL photons play a significant role in the propagation of the very high energy γ-ray photons from extragalactic sources. Where they interact with the γ-ray producing electron-positron pair, thereby attenuating the γ-ray photons. This attenuation can be observed as a steepening in the index of the VHE spectrum of the extragalactic γ-ray sources such as Blazars. The main focus of this thesis is to study the EBL fluctuation in the Universe and its impact on the VHE γ-ray spectrum.

The EBL fluctuations is investigated in three different ways. First, we study the spatial fluctuations in the Universe analytically (Kudoda & Faltenbacher, 2017). This was done through computing the fluctuations in the star formation rate (SFR) using the millennium simulation run 7 (MR7) galaxy catalogue. Then using the fluctuations in the SFR, we set upper and lower limits for the EBL following a forward EBL modelling approach. Our results show $\pm 50\%$ SFR fluctuation around the mean with a small ($\pm 1\%$) effect on the EBL. The fluctuations in the EBL, however, lead to $\pm 10\%$ variation in the γ-ray transmissivity in extreme cases, while its impact on the spectral index Γ of the VHE tail of the γ-ray spectrum is $\pm 1\%$.

Second, we investigate the fluctuations of the EBL in the γ-ray path from cosmological sources such as Blazars. In this part of the study we model the γ-ray path using a light cone. We develop a hybrid model of the EBL, where we combine the previous analytic model (Kudoda & Faltenbacher, 2017) with a numerical approach. By simulating the γ-ray path between $z = 0$ and $z = 0.5$ as cylinder with a radius of 50 Mpc (Kudoda & Faltenbacher, 2018). In this approach we divide the EBL in two parts: local (within the 50 Mpc) and homogeneous background. This was done to study and evaluate the impact of the presence of large scale structures along the γ-ray path. One order of magnitude fluctuation in the local EBL density is confirmed. However, in the total EBL this work is in agreement with our previous work ($\pm 1\%$ fluctuation). In addition, we investigate the situation when the γ-ray encounter a galaxy in its path. We find the presence of a galaxy with stellar masses of $M > 10^{11}$ $M_\odot$ will have a significant effect on the γ-ray absorption, thus, the spectral index of the VHE sources.

In the last part of this thesis we investigate the correlation between the power spectra of the EBL and the underlying matter (dark matter) distribution. This investigation was done by computing the power spectrum for the bolometric intensity of the EBL, and derive the bias between the two power spectra. If the EBL distribution is absolutely homogeneous, one expects the power spectrum to be flat. We confirm that the amplitude of the EBL fluctuations in general is small compared to the corresponding fluctuations in the matter distribution. However, on the scale of superclusters and voids (> 100 Mpc), it is more than two orders of magnitudes higher than small scales (< 10 Mpc). This is owing to the $1/r^2$ profile of the light distribution about point sources (i.e. galaxies), that flushes out the small fluctuations amplitudes.

Dedication

I dedicate this work to my family. To my mother, Fatma Ali, whose love, support, patience and guidance kept me focused and motivated. She made it her top priority to see us achieve our goals. To my three brothers, Ashraf, Ahmed and Khalid, who encouraged me in their own way to complete this work. And finally, to my late father, Mohamed Elhadi, who planted in me the yearning for knowledge, science and reasoning from an early age.

Ayman.

Acknowledgment

I would like first to express my sincere gratitude to my supervisor, Prof. Andreas Faltenbacher, for his patient guidance, support, and continuous encouragement through my PhD. I'm eternally grateful for his commitment to me and this project, since he was always available for consultation while he was still at the University of the Witwatersrand, and thereafter being available in an online capacity.

I am especially grateful to my friend Nebiha Shafi for her invaluable time and advice. She helped me to shape my ideas and thinking and greatly assisted me with crafting my thesis.

I would like to thank Paolo Marchegiani, Sultan Hassan, Geoff Beck, Dmitry Prokhorov, Yabebal Fantaye, and Warren Carlson for their invaluable time and insight during discussion and comments and their input greatly improved my manuscript. I would sent my gratitude to Marike Kluyts, who was the best editor and spell-checker I could have asked for.

I would like to thank all my teachers during all my years of studying. Special thank to my undergraduate supervisor at University of Khartoum, Dr. Sharief Abd Alla Hamed who made studying easy for me. Then, I would like to thank Dr. Luis Balona, my honours degree supervisor at the University of Cape Town. He believed in me, was very patient, and made me fall in love with coding. Finally, I am grateful to Dr. Ihab Riad for the interesting research completed in my masters degree.

I am also grateful to my colleagues and office mates and friends at the School of Physics, WITS University for all the fun we have had in the last four years, which made the stressful time of the research bearable.

I would like to acknowledge the German Academic Exchange Service (DAAD) for their generous financial support throughout my PhD degree at University of the Witwatersrand. I would also like to extend my gratitude to the National Astrophysics and Space Science Program (NASSP) for giving me the opportunity to join this wonderful program.

I would like to thank the International Centre for Theoretical Physics, Italy, for the opportunity to attend the Summer School during 2016.

I would like to thank the German Astrophysical Virtual Observatory (GAVO) for providing access to the Millennium Simulation (MR7) databases used in this thesis.

Last but not the least, I must express my very profound gratitude to my mother, Fatma Ali and brothers for supporting me spiritually throughout this thesis and my life in general. I also thank my brothers for giving me encouragement and encouragement endless amounts of pleasure.

Contents

Chapter 1

INTRODUCTION

When we look at the night sky, we wonder why celestial bodies appear as they do. This mystery has been studied for millennia as humanity tried to paint a consistent picture of the Universe. One of the oldest cosmological simple questions that can help us understand an important basic property of the universe is the question raised by the German astronomer Heinrich Wilhelm Olbers. The question is commonly known as Olbers' Paradox and is stated simply: Why is the night sky dark? Olbers argument was as follows: if the Universe is full of stars and infinite in size and age, then the light from these stars should have enough time to reach us and the sky should be infinitely bright day and night (e.g. Albrecht Unsöld, 2002). Olbers paradox challenges the conjecture that the Universe is static, infinite and homogeneous. This paradox plays an important role in the history of cosmology. While we now have answers for Olber's Paradox, it took us a long time to understand the nature of the Universe and solve this paradox.

A dramatic revolution in our understanding of the Universe happened in the last century when Edwin Hubble discovered that the Universe is expanding, providing observational confirmation for George Lemaître's theory, who was the first to propose an expanding model for the universe (Lemaître, 1927; Hubble, 1929; Lemaître, 1931). This discovery led to the development of the current standard model for the Universe called the 'Big Bang' model. The Big Bang model states that the Universe has expanded from an initially hot, smooth and dense state to its current cool, clumpy and low-density state, and that the expansion is ongoing.

Using experiments and observations, scientists are now able to explain how the Universe gained its current shape following the Big Bang. It was only about $400,000$ years after the Big Bang that the universe has cooled enough for light to be able to pass through (e.g. MacCallum, 2012). This primeval light has had its wavelengths stretched due to the expansion of the Universe, and can now be observed as a specific background radiation, namely, cosmic microwave background radiation (CMB). However, after this point, the Universe underwent the 'dark ages' until the formation of the first structures a few hundred million years later. The formation of structure in the universe represents a crucial transition in the evolution of the universe from its initial state to the state observed today. The earliest structures are believed to have formed from the growth of (linear) density perturbations generated by quantum fluctuations in the early Universe. The relic radiation of structure formation processes is believed to be captured as the second strongest background radiation after CMB: extragalactic background light (EBL). The EBL encodes all the energy released from all stars and galaxies since the formation of the first stars. However, many details of this epoch are still unclear, because direct observation is beyond the sensitivities of instruments, even with the current most powerful instruments.

The Big Bang model provided a satisfactory solution for Olbers' paradox by introducing a finite age of the Universe, which implies that photons from very distant sources do not have sufficient time to reach the Earth. The night sky in fact is not completely dark, it is brightened by several sources. In addition to the stars in the Milky Way the sky is filled with diffuse extragalactic background radiation fields across the entire electromagnetic spectrum, which include the CMB and EBL. While Olbers was mainly concerned with the optical darkness of the sky, in recent years we have discovered that the Universe is full of blazing sources of light even at highest energies (γ-ray). γ-ray sources provide an excellent laboratory to study and test fundamental physics through the most energetic processes in the Universe. On their own, γ-ray photons also interact with the EBL on their way to the observer.

In this thesis we will focus on the consequences of this interaction and the impact of the variation in EBL densities on the γ-ray path. Since the EBL is the remnant of the thermal and nuclear processes that accompanied structure formation and evolution, the interaction with the γ-ray photons provides an additional link between high energy astrophysics and structure formation and evolution in the Universe.

In the following sections we will layout some of the basic concepts of standard cosmology leading to structure formation, and provide brief descriptions of the observed diffuse background light at different wavelengths before moving onto the EBL and γ-ray astrophysics in the next chapter.

1.1 COSMOLOGICAL FRAMEWORK

In the late 1920s George Lemaître proposed a theoretical model of an expanding Universe, which was observationally confirmed by Edwin Hubble three years later. This discovery revealed that galaxies are moving away from us with a velocity (v) that is proportional to their distance (d), which is traditionally known as Hubble's law (Lemaître, 1927; Hubble, 1929; Lemaître, 1931):

$$v = H_0 d, \tag{1.1}$$

where $H_0 \sim 70\,\mathrm{km\ s^{-2} Mpc^{-1}}$ is the Hubble constant. This relation implies that the Universe began from a single point, which we now think is 14 billion years ago. One of the most important theories in cosmology is the Theory of General Relativity (GR) formulated by Albert Einstein in 1915 (Einstein, 1915). This theory describes the gravitational force as a curvature of space-time. Combining GR with the cosmological principle (i.e. the Universe is homogeneous and isotropic on cosmological scales) offers a framework that describes the Universe as a whole. Our understanding of the Universe through general relativity is based on the solutions of Einstein's field equation, which relate matter/energy and geometry:

$$G_{\mu\nu} \equiv R_{\mu\nu} - \frac{1}{2} R g_{\mu\nu} = \frac{8\pi G}{c^4} T_{\mu\nu}, \tag{1.2}$$

where $G_{\mu\nu}$ is the Einstein tensor, $R_{\mu\nu}$, R, $T_{\mu\nu}$ and G are the Ricci curvature tensor, Ricci scalar, the energy-momentum tensor and Newton gravitational constant, respectively. In a homogeneous and isotropic Universe the proper interval between two points can be written in the form of the Freidmann-Lemaître-Robertson-Walker (FLRW) metric (Friedmann, 1922):

$$ds^2 = -dt^2 + a^2(t) \left[\frac{dr^2}{1 - kr^2} + r^2(d\theta^2 + \sin^2\theta d\phi^2) \right], \tag{1.3}$$

where $a(t) = R(t)/R$ is the scale factor, it is the ratio between the distance scaled at the time t, $R(t)$, to the distance scaled at the present time R_0. The scale factor characterizes the relative size of a volume element as a function of time. r, θ and ϕ are spherical coordinates and k is a constant parametrizing the curvature of the Universe, with three possible values: $k = 1$ for a closed universe where the expansion stops and the universe will collapse; $k = 0$ is for a flat universe where the universe will expand forever at a decreasing rate; k=-1 for an open universe where it expands forever. It is necessary to determine the scale factor in order to describe the evolution of the universe completely. Following the cosmological principle Freidmann solved the Einstein field equation and obtained a set of two equations. The first equation relates the curvature and the energy density of the Universe with time derivative of the scale factor $\dot{a}$ (Weinberg, 1972):

$$H^2(t) = \left(\frac{\dot{a}}{a}\right)^2 = \frac{8\pi G}{3}\rho - \frac{kc^2}{a^2} + \frac{\Lambda c^2}{3}, \tag{1.4}$$

where ρ is the energy density and Λ is the cosmological constant that represents the vacuum energy. The second equation relates the energy density, the curvature and pressure p to the acceleration of the expansion, $\ddot{a}$ (second time derivative of the scale factor):

$$\frac{\ddot{a}}{a} = -\frac{4\pi G}{3}\left(\rho + \frac{3p}{c^2}\right) + \frac{\Lambda c^2}{3}. \tag{1.5}$$

The total energy density parameter ρ consists of contributions from three components: vacuum energy density or cosmological constant (ρ_Λ), matter density (both luminous and dark matter, ρ_m) and radiation energy density (ρ_r). This can be written in a more convenient form using the dimensionless notation:

$$\Omega = \Omega_r a^{-4} + \Omega_m a^{-3} + \Omega_\Lambda, \tag{1.6}$$

where (Ω_m, Ω_r , Ω_Λ) are the dimensionless matter, radiation and dark energy densities, respectively, and $\Omega = \rho/\rho_{\text{crit}}$ is the total energy density[1]. Fig. 1.1 shows the percentages of the different densities at the present time.

The expansion of the Universe impacts observational quantities in many ways. For example, the emitted frequency of a photon from a distant object is shifted to lower frequency, because light waves stretch with the cosmic expansion where all objects are moving farther from each other. This shift in waves

[1] $\rho_{\text{crit}} = 3H^3/8\pi G$ is the critical density, which is the density that is required to keep the Universe flat.

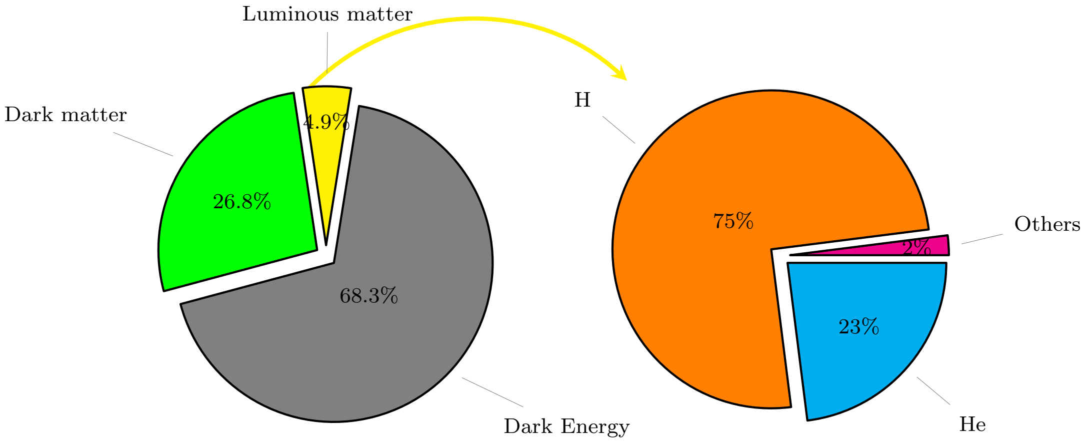

Figure 1.1: The percentages of the energy density at $z = 0$ and the abundance of the elements in the Universe (Planck Collaboration et al., 2014b).

is called *redshift* and it is related to the scale factor by:

$$1 + z = \frac{\lambda_\mathrm{o}}{\lambda_\mathrm{e}} = \frac{a_0}{a}, \tag{1.7}$$

where λ_o and λ_e are the observed and emitted wavelengths, respectively. The equation that relates the contribution from each component and scale factor of the universe is:

$$H(z) = H_0[(1+z)^4\Omega_r + (1+z)^3\Omega_m + (1+z)^2\Omega_k + \Omega_\Lambda]^{1/2}, \tag{1.8}$$

where $\Omega_k \equiv -k/H_0^2$ represents the curvature. In an expanding Universe it is important to differentiate between the *comoving distances* (D_C), which refers to the distance between two points measured by a ruler at the time of the observation, and the *luminosity distance* (D_L), the distance that light travel in an expanding universe:

$$D_L \equiv \sqrt{\frac{L}{4\pi S}}, \tag{1.9}$$

where L and S are the bolometric luminosity[2] and flux, respectively. We can write the relation between the D_L and D_C as (e.g. Hogg, 1999):

$$D_L = (1+z)D_C, \tag{1.10}$$

[2]bolometric luminosity: is the energy per time, bolometric means the radiant energy over a wide wavelength band

The FRW metric together with the density parameters ($\Omega_{M,\Lambda,r,k}$) and the Hubble parameter H are the basis of the current structure formation model known as lambda cold dark matter (ΛCDM) model. The ΛCDM model provides a good description of the origin of the Universe that is consistent with cosmological observations. In the following section we will give a description of structure formation from the ΛCDM point of view.

1.2 ΛCDM STRUCTURE FORMATION

The cosmological principle discussed above only applies on large scales, however, on small scales matter tend to cluster. In order for matter to clump and later form structure in a homogeneous universe, small perturbation is required. In the following we will discuss the initial conditions that led to structure formation.

1.2.1 Initial conditions

It is believed that the first structures arose due to perturbations as a result of quantum fluctuations that were dominant at the early Universe. As a result of these perturbations small, over-dense regions emerge and over time evolve by accumulating more matter due to gravitational force. When the amplitude of the perturbation reaches a certain density contrast (~ 1), the over-dense regions will detach form the expansion and collapse. Density perturbations and gravitational instabilities are believed to be the seeds for large scale structure. The properties of these gravitational instabilities and the consecutive structures formations are mainly dependent on the choice of cosmological model (Mo et al., 2010).

The initial perturbations in the ΛCDM universe consist of collisionless dark matter and baryonic matter (gas). The dark matter that was formed in the over-dense regions collapse and relax, forming a dark matter halo (Mo et al., 2010). While the gas falling into a dark matter halo shocks to a virial temperature[3] and slowly cools into hydrostatic equilibrium inside the gravitational potential well formed by the dark matter halo.

Cooling is an important process in galaxy formation, and depends on the density and temperature of the gas. Several mechanisms can be responsible for cooling the gas (e.g. radiative cooling processes). If the cooling time is

[3] $T_{vir} = (\mu m_p/2k_B)V_{vir}^2$ where μ is the mean molecular weight `http://iopscience.iop.org/article/10.1086/523623/fulltext/71240.text.html`

short, the gas will decouple from the dark matter halo and fall into the centre of the halo and form a 'protogalaxy' at the centre of the halo before it reaches hydrostatic equilibrium. During the cooling process, the angular momentum of the gas and halo may be conserved, causing the gas to spin up as it falls onto the centre of the halo. This infalling gas then forms a cold disk or a disk galaxy while settling into centrifugal equilibrium (e.g. Mo et al., 2010).

1.2.2 Galaxy formation

Galaxies are the fundamental visible components of the large scale structure that reveal the underlying distribution of gravitational matter in the Universe. From the previous discussion we know that the Universe started with a very dense and almost uniform state with tiny fluctuations that grow with time via gravitational attraction, and eventually form a galaxy. The first galaxies are believed to have formed around 13 billion years ago (e.g. FRAS, 2007).

As mentioned earlier in Section 1.2.1, the structure of a galaxy depends on the angular momentum and cooling time of the gas cloud. While clouds with higher angular momentum form a disc structure, clouds with lower angular momentum form a spheroidal shape (elliptical shape) (Fall & Efstathiou, 1980). The atoms in these clouds interact through collisions and eventually collapse to the centre by the emission of photons and thus radiates energy away. The dark matter component does not interact in this manner and keeps orbiting in the halo and does not collapse. In principle it should be possible to observe the photons emitted by the first galaxies. However, these photons are very faint and distant, so we have not yet been able to detect them. The galaxies that we observe are the result of the evolution of these protoglaxies.

In order to verify the theory of galaxy formation and evolution, we need to understand the properties of galaxies at different evolutionary epochs. There are many internal and external factors that affect the properties of galaxies at different epochs. Among the internal factors are physical processes related to the baryonic matter composition, such as the expulsion of gas and metals due to activities related to star formation and black hole growth (i.e. feedback processes) Mo et al. (2010). External factors such as merger (e.g., Toomre & Toomre, 1972; Conselice, 2003), galaxy harassment (e.g., Moore et al., 1996) and striping (tidal and ram pressure) (e.g., Spitzer & Baade, 1951; Gunn & Gott, 1972) also affect the gas content and morphology of galaxies. There are different types of galaxies ranging form dwarf to giant elliptical depending on their morphology and stellar content. Furthermore, galaxies are commonly found in groups of various sizes (small groups and clusters) (Sepp & Gramann, 2013).

There are may uncertainties in the models of galaxy formation and evolution. As primordial fluctuations become non-linear, analytical descriptions of structure formations become much more complicated with lesser predictive power. Therefore, it is necessary to simulate the non-linear phase of structure formation given by different models.

Simulations There are many algorithms that simulate the cosmic evolution and predict galaxy formation. Two physically motivated approaches that have been used to simulate structure formation are: hydrodynamical simulations and semi-analytical models. The hydrodynamical simulations start by setting up the initial density fields for the baryonic and the dark matter and track their evolution and interaction through cosmic time (e.g. Cen & Ostriker, 1993; Springel & Hernquist, 2002). Although they are very successful in predicting observation, they could be computationally expensive because of the calculations involved in solving all non-linear equations of hydrodynamics, gravity, etc. simultaneously. The second approach is the semi-analytic models (SAMs) (e.g. Kauffmann et al., 1993; Cole et al., 1994; Kauffmann et al., 1999; Cole et al., 2000; Somerville et al., 2001). SAMs are built on dark matter simulations, which are very inexpensive to run. SAMs model mass accretion history of the dark matter halo by *'merger trees'*. By using physically motivated recipes for gas cooling, star formation, chemical enrichment and feedback from black holes and supernova, SAMs reproduce most of the galaxy properties. SAMs do not have an explicit dynamic range [4], so they are powerful to produce the average and global quantities. One can use the outcome of the simulation together with the stellar population synthesis to compute the spectrum of the galaxies. The predictions of SAM have been shown to be in-line with observations particularly in the UV-optical regime, making these models crucial in understanding galaxy foWe can talk in one hour 23.00 my time on whatsapp rmation. However, SAMs have difficulties in modelling the photons absorption and re-emission (the infra red region) by the dust. This is due to the fact that the dust emission depends on many factors including the

[4] Numerical simulations have an explicit dynamic range that is set by the simulation volume and resolution that is set by the cell size. While they are limited to these scales, they are able to study into details the local fluctuations and environmental dependencies that SAM isn't able to capture due to the lack of such confined volume with detailed processes on different scales Somerville & Primack (1999).

geometry and composition. Also, SAMs cannot track the internal structure of the galaxies and their morphology. One way to tackle these issues, is to combine the prediction from SAM with radiative transfer codes that numerically solve the absorption and re-emission issue (Granato et al., 2000; Baugh et al., 2005; Fontanot et al., 2007). The disadvantage of this method is that it uses a simplified geometry for the different types of galaxies. In particular, the luminous and ultra-luminous IR galaxy, like objects that are known to be merger systems are not well modelled. Furthermore, many free parameters in the model must be fine-tuned to fit the observation, which may vary with evolution of the galaxies over time.

An alternative approach to treat the dust emission is to estimate the star light fraction that is absorbed by the dust either analytically or semi-analytically, at each galaxy in the simulation. This can be done based on stellar metallicity, stellar populations and geometry of every galaxy. There are many approaches to this treatment. For example one might assume that the column density of the metals in the gas phase is proportional to the optical depth in the face-on V or B-band of the dust in the disk, and the inclination of the disk modelled using a simple slab model that assume that the stars and dust are uniformly distributed, and the dependence of the wavelength can be calculated by a fixed attenuation law (e.g. the attenuation law by Calzetti et al. (2000) of the Milky Way or that of the starburst galaxy) (Guiderdoni & Rocca-Volmerange, 1987; Lacey et al., 1993; Guiderdoni et al., 1998; Kauffmann et al., 1999; Somerville & Primack, 1999; Devriendt & Guiderdoni, 2000). De Lucia & Blaizot (2007) used two models, the first is a slab model for the 'cirrus' component[5] and Charlot & Fall (2000) model for the younger stars. Fontanot et al. (2009) after testing a different analytic approaches with a full radiative transfer code concluded that there are a good agreement between the SAMs model that treat the dust analytically with the full radiative transfer in most of the properties, such as luminosity functions with less computational power. Moreover, one can use the observational data to constrain the amount of the energy absorbed and then remitted by the dust. This can be done by using the calibrated spectral energy distributions (SEDs) template to evaluate the wavelength dependence in the dust emission (Devriendt et al., 1999; Chary & Elbaz, 2001; Dale & Helou, 2002; Lagache et al., 2004; Rieke et al., 2009).

[5]Galactic cirrus clouds are thin and wispy clouds that surround Milky Way, partially block and confuse our extragalactic view.

1.2.3 Star formation

Star formation begins when the gas in the dark matter halo cools down collisionally and collapses gravitationally. As it collapses the gas cloud will fragment into small pieces and form stars. There are two widely accepted modes of star formation: the quiescent mode and the starburst mode. The quiescent mode describes the formation in an isolated and rotationally supported disk, with a fixed critical surface density above which the stars will form (Kennicutt, 1998). In the starburst mode stars are formed in relativity small regions ('starbursting' regions) in an episodic manner. In this mode the star formation is triggered by dynamic instabilities and interactions (merger) (Somerville et al., 2008).

The details of the processes involved in star formation are not clearly understood. A key ingredient in the star formation processes that is still unclear is the initial mass function (IMF). The IMF describes the distribution of mass between stars born at the same epoch, and plays an essential role in the determination of the relative importance of two star formation modes (e.g. Salpeter, 1955; Miller & Scalo, 1979).

Despite the incomplete understanding of stellar formation, stellar evolution is fairly well understood. Stars are big nuclear reactors, which convert lighter elements to heavier elements at their core through nuclear fusion.

The evolution of stars can be described by their positions on a graph known as the Hertzsprung-Russell (HR) diagram. The HR diagram shows that when the luminosity of stars are plotted against their temperature, the stars tend to fall into different groups in different regions of the diagram. Stars with common properties share the same region (see Fig. 1.2). As stars evolve (the temperature and luminosity of the stars changes) over time, their positions on the HR diagram change. Measuring the properties of stars at different regions of the HR diagram allows us to determine their age, mass and metallicity, which in turn tell us about the star formation history of a galaxy.

Taking a given IMF and the known evolutionary tracks, we can predict the spectrum of the stellar population by adding the individual spectra of the stars (stellar population synthesis). Using evolutionary tracks models (e.g., Eggleton et al., 1989) the spectrum of the population at any time can be obtained. By superpositioning the spectra of different stellar populations in a galaxy we can compute its overall spectrum. There are different stellar population spectrum libraries that provide spectra for different metallicities and ages (e.g.,

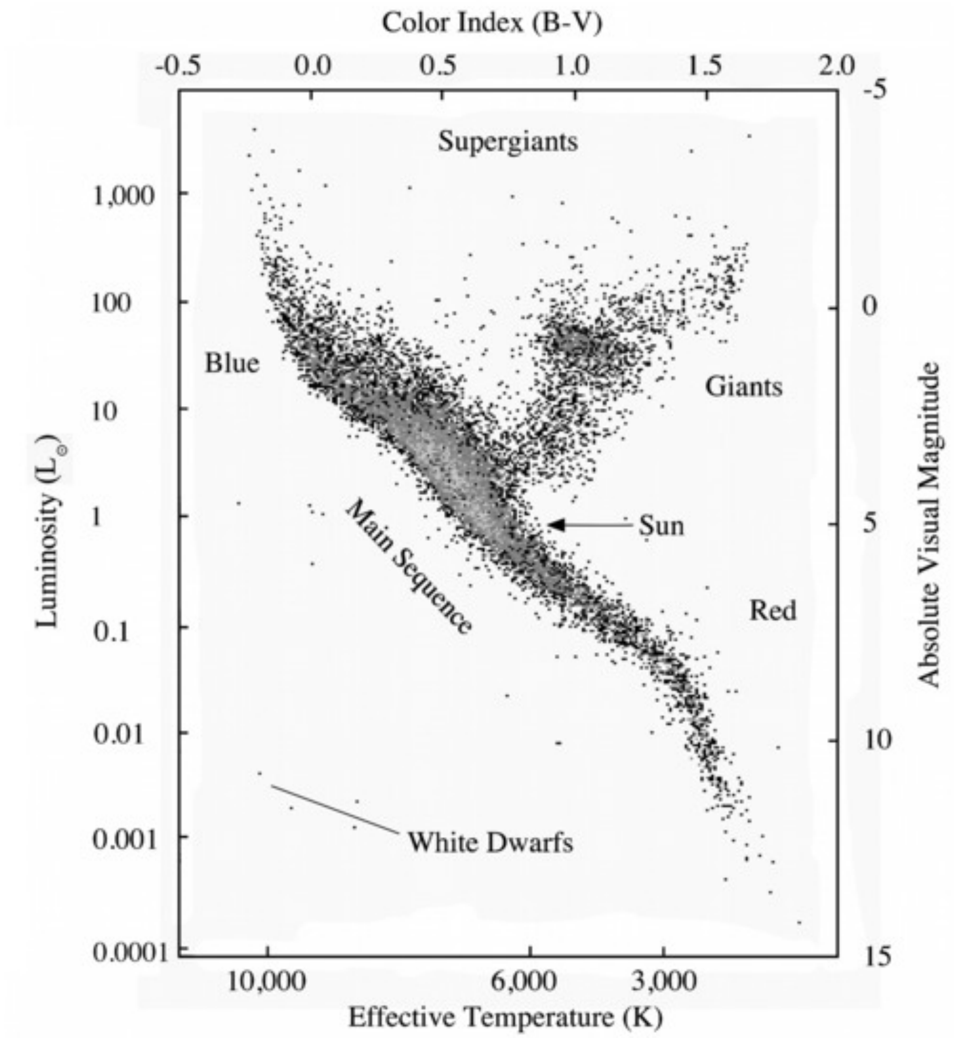

Figure 1.2: The Hertzsprung-Russell (HR) diagram, illustrates the evolution of the stars. Most stars, like our Sun, are found on the main sequence. The main sequence evolve in the diagonal from bottom right (low temperature, red stars) to top left (high temperature, blue-white) of the diagram. Sun-like stars evolve into red giants located at the top right of the diagram, burning helium. Supergiants, which are very rare and luminous, are located above the giants. White dwarf stars, which are faint and hot, are found in the lower left of the diagram. Figure taken from: `https://ase.tufts.edu/cosmos/view_picture.asp?id=1404`.

Bruzual & Charlot, 2003; Maraston, 2005). The simplest galaxy spectrum can be obtained by assuming a single stellar population (SSP).

1.3 DIFFUSE EXTRAGALACTIC BACKGROUND RADIATION FIELDS

The diffuse extragalactic background radiation (hereafter DEBRA) is the diffuse radiation which originated outside of the Milky Way, that fills the universe. The DEBRA has an extended spectrum that ranges from 10^{-7} eV to 100 GeV (Hauser & Dwek, 2001). The DEBRA provides a unique window to study fundamental concepts in cosmology and astrophysics, because of the information that is embedded in it. The DEBRA is also a very important tool to test and verify the theories about the origin and evolution of the Universe. There are two possible origins for the DEBRA: from resolved point sources or from a diffuse emission mechanisms. The DEBRA may also originate from a combination of the two mechanisms. Fig. 1.3 shows a schematic representation of the entire DEBRA spectrum in units of intensity (the data in this figure were taken form Hauser & Dwek (2001)).

Determining the DEBRA is challenging as it requires a careful accounting of the foreground Galactic diffuse emission and the emission from our solar system (Hauser & Dwek, 2001). In addition, we need to understand and model the different emission mechanisms at different parts of the spectrum.

To clearly identify the origin of the DEBRA, detailed observations and modelling of all the possible radiative processes (point or extended sources) in the sky is needed. This process mostly depends on the telescope and detector capabilities and technology. If the DEBRA is due to unresolved point sources, higher angular resolution telescopes are needed to resolve the larger number of point sources that possibly contribute to the DEBRA. On the other hand if the DEBRA is of diffuse origin, a precise DEBRA spectrum is needed to reveal the physical process involved in its production.

Another important aspect in DEBRA study is the intensity and angular fluctuations in its spectrum. Small or large scale fluctuations detections can be used to verify its cosmological origin. Large isotropy can indicate cosmological origin (e.g. CMB) and can be used to disentangle the DEBRA from the galactic diffuse emission (e.g. Hauser & Dwek, 2001). In addition, the angular fluctuations in the spectrum can be compared with the angular fluctuations in the observed sky map or the expected different sources. This will help us determine the contribution of the DEBRA from different sources of radiation.

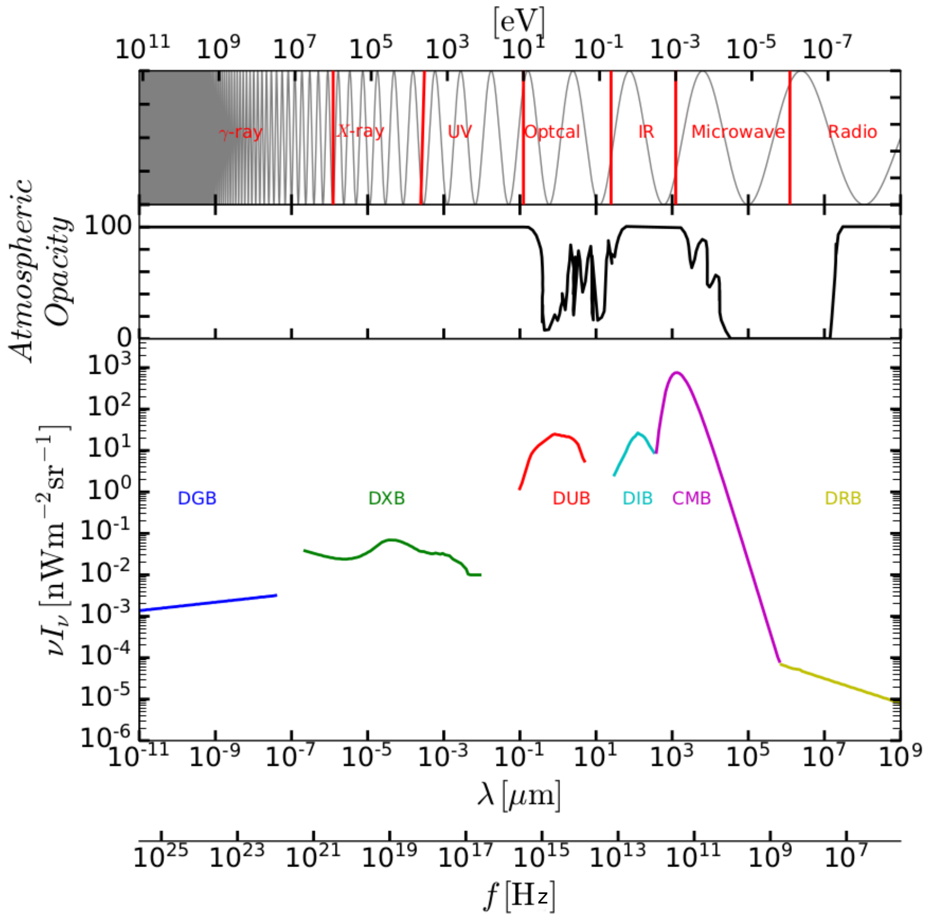

Figure 1.3: The top panel shows the different energy ranges in the electromagnetic spectrum, the middle panel show the Earth's atmosphere opacity at different wavelengths. The bottom panel is a representation of the DEBRA showing the intensity different in each part of the spectrum. The blue line is the extragalactic γ-ray background EGB, the green is the diffuse X-ray background (CXB), the red and cyan represent the EBL spectrum, the CMB is in magenta, the cosmic radio background (CRB) is in yellow. The data for these lines are taken form Hauser & Dwek (2001) using WebPlotDigitizer 3.8. `https://apps.automeris.io/wpd/`

In the following sections we will provide brief descriptions of the different DEBRA spectrum regimes starting form the highest energy. We will further discuss the EBL (comprising of the diffuse Ultraviolet, optical and Infra-red extragalactic background) in the next chapter.

1.3.1 The cosmic γ-rays background

The Cosmic γ-ray background (CGB) is observed in the highest energy regime of the DEBRA above 0.1 GeV. Since the Stratosphere is completely opaque in this regime, it is observationally the most challenging part of the DEBRA, and it can only be observed using high-altitude balloons or from space.

Recent observations suggest that the CGB spectrum is a superposition of unresolved extragalactic point sources and diffuse emission mechanisms. Observations by Fermi-LAT shown that the CGB between $0.1 - 820\,\mathrm{GeV}$ is well represented by a power law with a cut-off above $\sim 300\,\mathrm{GeV}$ (Ackermann et al., 2015), see Fig. 1.4. The main contribution to the CGB may come from unresolved AGNs (Fermi LAT Collaboration, 2010), star-forming galaxies (Fields et al., 2010) plus γ-ray bursts. Millisecond pulsars are believed to have a small contribution to the CGB (Siegal-Gaskins et al., 2011). On the other hand, emissions from dark matter annihilation (Pieri et al., 2008) and from interaction of very high energy cosmic rays with other parts of the DEBRA spectrum could account for the diffuse origin. Other emission mechanisms are discussed in Dermer (2007).

1.3.2 The cosmic X-ray background

The cosmic X-ray background (CXB) was discovered in a rocket experiment designed to study the X-ray fluorescence from the moon (Giacconi et al., 1962). The realization of the extragalactic origin of the CXB came from the high isotropy in all direction of the sky. The CXB energy range starts at 0.1 keV and extends up to 511 keV, however, its commonly grouped into two sub-regions: soft X-ray $< 1\,\mathrm{keV}$, and hard X-ray $> 1\,\mathrm{keV}$.

Deep surveys in the X-ray such as Chandra and XMM-Newton have shown that all CXB less than $\sim 2\,\mathrm{keV}$ originate from AGNs emissions that contain super-massive black holes (Giacconi et al., 2002; Alexander et al., 2003; Hasinger, 2004). However, about 50% of the CXB at higher energies ($\sim 6\,\mathrm{keV}$) are still unresolved (Worsley et al., 2005). Possible contributors to the unresolved part of the CXB could be from the emissions by undetected populations

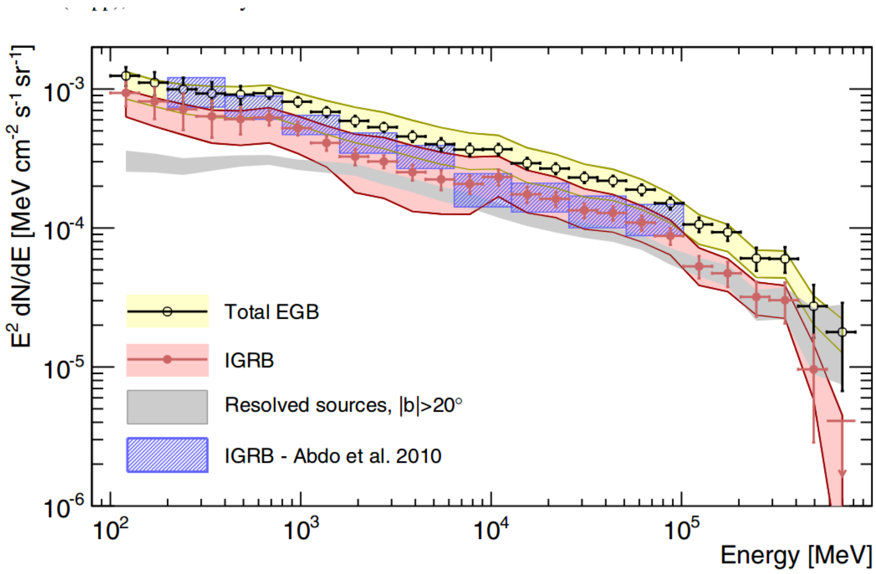

Figure 1.4: The measured intensity of the Cosmic γ-ray background (isotropic γ-ray background (IGRB) plus intensity of detected sources) by Fermi-LAT. The figure was adopted from Ackermann et al. (2015).

of highly absorbed AGNs (e.g. Zamorani, 1995; Schmidt et al., 1998). Other possible contributions might come from hot gas in galaxy clusters, supernova remnants, and massive X-ray binary systems. Fig. 1.5 shows a combination of observations of the CXB from different instruments.

1.3.3 The diffuse ultraviolet, optical and infra-red backgrounds

The ultraviolet spectral range extends from 0.001 μm to 0.3 μm. The Ozone layer (at $\sim$ 30 km above the sea level) absorbs all the energy below 0.285 μm, so the atmosphere of Earth is opaque in this region. Observation of the diffuse ultraviolet background (DUB) must be conducted from the space. Although the intensity of the zodiacal light[6] becomes considerably small in the ultraviolet regime, the Earth's atmosphere absorbs DUB below 912 Å due to the Lyman limit of neutral Hydrogen. Therefore, direct measurements of the DUB below this limit are impossible (Hauser & Dwek, 2001).

The diffuse optical background (DOB) spectrum covers the wavelength range from 300 μm up to 1000 μm. Although observation of this part of the DEBRA is the oldest in the history of astronomy, the CXB was the first DEBRA to be detected. Due to the strong foreground that consist the zodiacal

[6]Zodiacal light: refers to sunlight that has been scattered by the interplanetary dust.

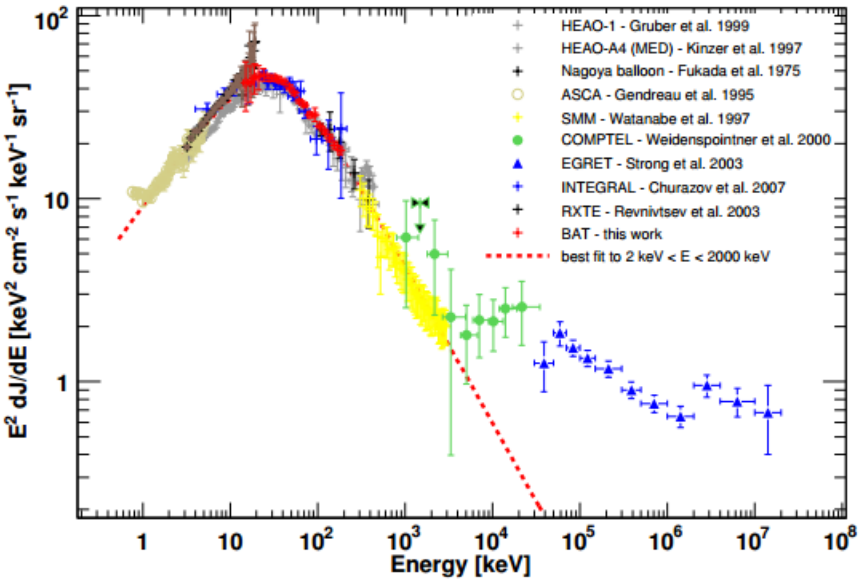

Figure 1.5: The diffuse X-ray background measurements, the red dashed line represents the best fit between 2 keV and 2 MeV. The figure was adopted from Ajello et al. (2008).

light, airglow[7], bright stars and the diffuse emission from our Galaxy, direct measurements of the DOB is extremely difficult (Hauser & Dwek, 2001).

The cosmic infra-red background (CIB) spectrum lies between 1 μm and 400 μm. This part of the DEBRA is of great importance in cosmology as it is believed to be the accumulated emission form the earliest structures and galaxies. This makes CIB observations an important tool for probing the very early universe (Bond et al., 1986; Hauser, 1995; Lonsdale, 1995). The CIB is generally divided into three subranges: near infra-red from $1-5\,\mu$m, mid infra-red from $5-50\,\mu$m and far infra-red $50-400\,\mu$m.

The CIB together with the DUB and DOB radiations form what is conventionally known as the EBL. The EBL is an important tool used to constrain the gas, dust and metal content of the Universe. It also provides important constraints on the integrated cosmological star formation history of the universe (Dwek & et al., 1998), see the next chapter for more details.

[7]Airglow: is a faint emission from the Earth atmosphere, that is caused by the recombination of atoms that are ionized by the Sun light or cosmic rays, in addition to the chemiluminescence interaction between of Oxygen and Nitrogen with hydroxy ions (e.g. Roach & Gordon, 1973).

1.3.4 The cosmic microwave background

The cosmic microwave background (CMB) was serendipitously discovered by Arno Penzias and Robert Wilson in 1965 (Dicke et al., 1965). Their discovery was a milestone in cosmology and a puzzle piece that perfectly fit the story of the Big Bang theory. The CMB is the brightest component of the DEBRA, and has the most perfect blackbody-like spectrum observed in nature, at a temperature of $\sim 3\,\mathrm{K}$. The intensity of the spectrum peaks at $\sim 1.0\,\mathrm{mm}$, where the atmospheric emission makes accurate measurements of the CMB from the ground impossible. Therefore, studies of the CMB spectrum are done using space satellite missions. The first mission dedicated to study the CMB spectrum was the Cosmic Background Explorer (COBE) in 1989, which measured the radiation spectrum between $1\,\mu\mathrm{m}$ and $1\,\mathrm{cm}$ over the whole Sky. COBE revealed a blackbody spectrum at $2.725\,\mathrm{K}$ with very small anisotropies (in the order of $10^{-5}\mathrm{K}$), mimicking the prediction of thermal variations produced by the quantum fluctuations expected from matter in a small volume that had expanded into the size of the current Universe. The Wilkinson Microwave Anisotropy Probe (WMAP) mission in 2001 and the Planck mission in 2009 followed COBE. Fig. 1.6 and 1.7 shows the measured CMB spectrum by COBE and power spectrum of the CMB as measured by Planck (Planck Collaboration et al., 2014a).

1.3.5 The cosmic radio background

The history of radio astronomy started in the third decade of the 20^{th} century when Karl G. Jansky discovered that the Milky Way had radio emissions. The Cosmic Radio Background (CRB) is found in the lowest energy band of the DEBRA where wavelengths range above $1\,\mathrm{m}$. The CRB spectrum shape was first determined by Clark et al. (1970).

Synchrotron emission from the Milky Way dominants measurements of the CRB. To overcome this challenge and separate the CRB from the synchrotron emission, one may map the sky in different wavelengths, assuming that foreground emission has the same spectrum shape in all directions and extract the the intensity of the CRB. Observation shows that above $10\,\mathrm{MHz}$ CRB spectrum is steeper than the galactic synchrotron spectrum (Longair, 1995), and can be fitted using a power law with a clear cut off below $\sim 4\,\mathrm{MHz}$. The cut off is due to synchrotron self-absorption in the resolved sources (Simon, 1977).

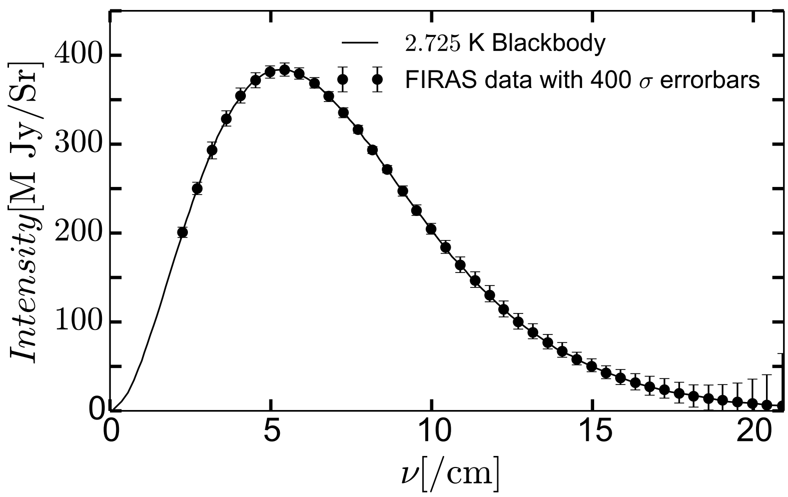

Figure 1.6: The spectrum of the CMB observed by the COBE-FIRAS instrument, showing its perfect blackbody shape at $T = 2.725 \pm 0.001\,\mathrm{K}$. Figure is replotted from (Bartelmann, 2008).

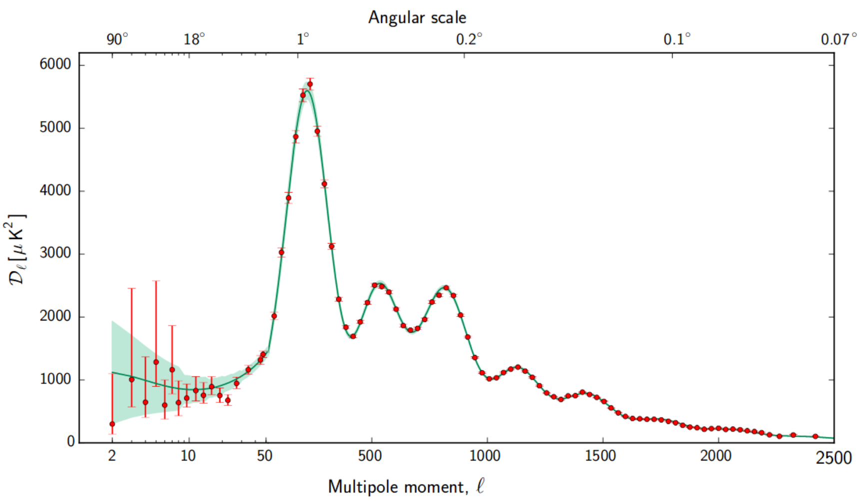

Figure 1.7: The CMB angular power spectrum as seen by Planck. The red dots with the error bars represents the data points and the green line is ΛCDM theoretical model fit. The green shaded area represents the cosmic variance. The position of the first peak reflects the geometry of the Universe, while the second and third peaks provide information about the matter content in the Universe. Figure taken from (Planck Collaboration et al., 2014a).

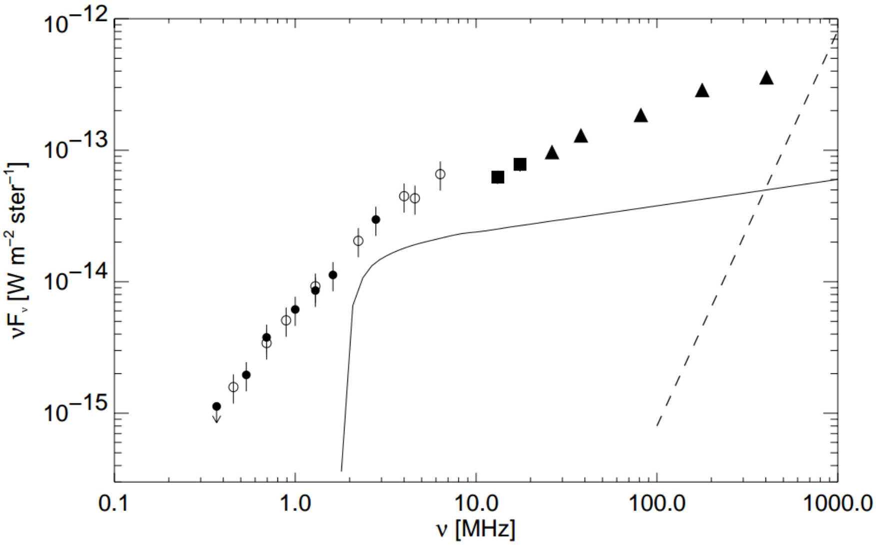

Figure 1.8: Total radio emission spectrum observed close to the north galactic pole. The solid line represents the CRB as estimated by Simon (1977) and Peacock (1995). While the filled triangles and filled squares are from Purton (1966); Bridle (1967), respectively, the filled and open circles are from Alexander et al. (1969). The figure is adopted from (Weidenspointner, 1999).

Fig. 1.8 shows the spectrum of the CRB together with the total radio background measured at the north galactic pole. The intensity of the CRB is the superposition of extragalactic radio sources. Therefore, by observing the CRB we can study the potential sources that may contribute to the CRB and their evolution. Different populations of galaxies are considered to be contributors to the CRB (Peacock, 1995).

Another important aspect of observing the CRB is the possible detection of high redshift neutral hydrogen at the 21 cm emission line, which can provide a useful tool to constrain the evolution of galaxy formation (Peacock, 1995). In addition, the spatial distribution of the CRB can be used to map the large scale structure in the universe (Wall, 1990).

1.4 OUTLINE

Chapter two of this thesis is dedicated to the discussion of the EBL and γ-ray astrophysics. I will also discuss the relation between the EBL and very high energy (VHE) γ-ray in more detail.

In Chapter three, I will provide a robust EBL model and analytical description of the EBL fluctuations which has been published in Kudoda & Faltenbacher (2017). For the EBL model I applied Razzaque et al. (2009) model for the stellar emission and added the dust emission following the model by Finke et al. (2010). I introduced a special fluctuation in the star formation rate (SFR) using the millennium simulation run 7 (MR7) (Lemson & Virgo Consortium, 2006; Guo et al., 2013). This work is a continuation of ongoing research (Kudoda, 2015; Kudoda & Faltenbacher, 2016).

In Chapter four, I will discuss a new hybrid EBL model combining two EBL modelling approaches: semi-analytic and forward models as recently published in Kudoda & Faltenbacher (2018). The main goal of this work is to study the effect of the large scale structure on the γ-ray spectrum. In addition, I will investigate the effect of a close galaxy encounter to the γ-ray path. The results of this work confirm the previous work and presents a new tool that can be used in further γ-ray studies.

In Chapter five, I will present a different way to study the EBL fluctuations by looking at the power spectrum of the bolometric intensity of the EBL and its correlation with the underlying matter distribution. This is done by computing the bias between the EBL power spectrum and the dark matter power spectrum. The underlying EBL model is based on the model presented in the fourth chapter (a hybrid EBL model). Conclusion and future work will be presented in Chapter six.

Chapter 2

THE EXTRAGALACTIC BACKGROUND LIGHT AND γ-RAY ASTROPHYSICS

2.1 EXTRAGALACTIC BACKGROUND LIGHT

Extragalactic background light (EBL) is the integrated light from resolved and unresolved extragalactic sources plus the emission from any diffused mechanism since the recombination era. This initial radiation from the formations of stars and galaxies was redshifted to a longer wavelength due to cosmic expansion, which was subsequently absorbed by dust and re-emitted in IR regime. Hence, the EBL encodes fundamental information about star formation and the evolutionary history of the Universe and cosmology.

The EBL spectrum is characterized by two distinct peaks. The first peak between 0.1 and 10 μm is believed to be due to stellar contribution, and provides ample information about the baryons and neucleosynthesis across cosmic time. While the second peak between 10 and 1000 μm is associated mainly with dust emission. Fig. 2.1 shows a schematic representation of typical spectral energy distribution (SED) of the EBL in comparison with the CMB.

There are several processes responsible for the production of EBL. Major sources of the EBL include thermonuclear processes, dust emission, and emission from early structure formation (Hauser & Dwek, 2001; Dwek & Krennrich, 2013). The total spectrum of the EBL lies between 0.1 and 1000 μm. Accurate measurements of the EBL are important to constrain the physical processes involved in its formation and evolution. Since the radiation field itself is redshifted due to cosmic expansion, a detailed study of the EBL can provide

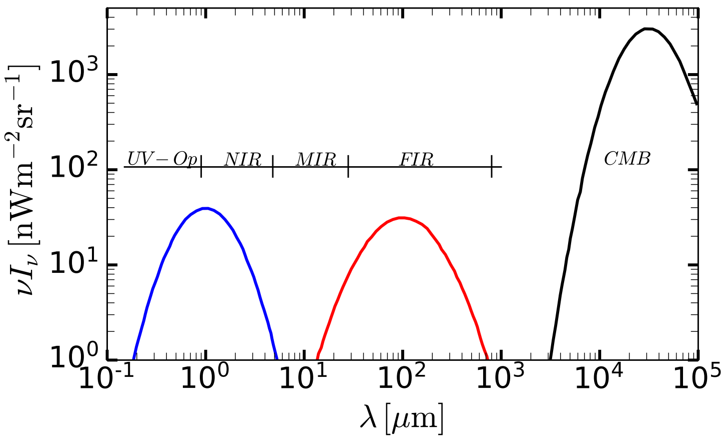

Figure 2.1: The schematic shows a snapshot of the EBL and CMB spectra at the present time ($z = 0$). The spectrum in blue is the stellar emission in the UV, optical, and NIR, the dust emission between MIR and FIR is shown in red, and the CMB spectrum is shown in black.

additional constraints on both the SED of individual sources as well as their redshift distribution. Furthermore, the EBL is also a source of opacity for VHE photons. It interacts with these photons as they propagate through the Universe from distant sources. This interaction can be used to constrain both the density of the EBL and the intrinsic spectrum of very high energy (VHE) γ-ray sources.

2.1.1 EBL contributors

A better understanding of all the sources that contribute to the EBL can lead to a fair prediction of its emission mechanisms, and thus its density. The main contributors to the EBL in the UV and optical ranges are stellar emissions, while the IR regime is dominated by dust emission. However, there are also other sources of EBL such as AGN and exotic sources.

2.1.1.1 Stellar emission

The main contribution of the EBL in the UV and optical ranges comes from the energy generated by nuclear fusion of lighter elements into heavier ones within stars. Stars are generally classified into three populations according to their metal content ($Z \geqslant 2$)[8]. **Population III** (Pop III) constitute a theoretically

[8] Z≡ is the atomic number or the number of protons in the atom.

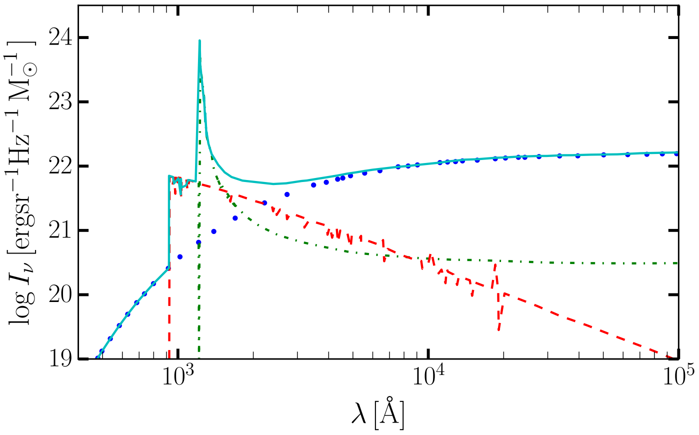

Figure 2.2: The expected spectrum of Pop III stars as a function of wavelength is shown by the cyan line. The red dashed, blue doted, and green dashed-doted from the nebula surrounding the star lines represent the emission from the star with a cut off at shorter wavelengths due to the Lyman limit, bremsstrahlung emission (free-free), and Lyα recombination emission in the nebula, respectively. The spectra are at the rest frame of the star. The figure is replotted from Santos et al. (2002)

predicted population, not observed yet. They are the first stars formed in the Universe and thus are assumed to be comprise of only Hydrogen, Helium and a very small amount of Lithium. The metallicity[9] of Pop III stars is very low, typically $\sim 10^{-4} Z_\odot$ ($Z_\odot$ is the solar metallicity; Schneider et al., 2002). Pop III stars are formed by the collapse of the primordial gas clouds. Due to the high temperature of the gas in that era, and the lack of metals (which prohibits cooling through radiative de-excitation of collisionally excited metal transitions) the cooling process, which is molecular cooling (Saslaw & Zipoy, 1967), was very slow, halting the fragmentation of the gas. Therefore, Pop III stars are expected to be massive (around several hundred solar masses (Bromm et al., 1999; Abel et al., 2000)), evolve quickly and explode as Type-II supernovae (core-collapse supernova). Because of the subsequent enrichment of the ISM with metals (Abel et al., 2002), these stars are believed to be the progenitors of the later, metallicity enriched populations. Fig. 2.2 shows the expected spectrum for Pop III stars.

The supernovae from Pop III stars may reheat its surroundings, and even expel some of the gas from the protogalaxy. The increase of metals in the ISM

[9]Metellicity is the fraction of heavy elements compare to the Hydrogen in the star

allows more efficient cooling processes to take place and provides an opportunity for smaller masses to fragment and form stars, i.e, **population II** (Pop II). The metallicities of Pop II stars are in the range of $10^{-3} - 10^{-1}\, Z_{\odot}$. These stars can presently be observed as cool stars in the halos of spiral galaxies and galaxy bulges (Prialnik, 2000).

Population I (Pop I) stars are the youngest, longer-lived, less massive, hottest and highest metellicity ($\geq 10^{-1} Z_{\odot}$) stars. These stars (e.g. our Sun) can be found today in the discs of spiral galaxies (e.g. Prialnik, 2000).

Most stars are formed in starburst regions within galaxies. If a group of stars is born during the same starburst episode they will have the same metallicity, and their mass distributions can be described by an universal initial mass function (IMF). Therefore, one can use their metallicity and IMF to compute the collective emission profile of a stellar population. By superpositioning individual starburst SEDs, a galaxy's spectrum can be modelled. We can evaluate the contribution of stellar emissions to the EBL by integrating over all the galaxies spectra in a comoving volume. However, there is one main factor that needs to be considered, i.e., the absorption and re-emission of the starlight inside galaxies by the gas and dust in the IGM.

Hydrogen is the most efficient absorber in the Universe. The ionization energy of Hydrogen is 13.6 eV (Lyman limit), therefore a photon with energy above 13.6 eV will be absorbed by the Hydrogen cloud in the ISM. Moreover, photons with energy less than 13.6 eV also get absorbed by exciting Hydrogen. On the other hand, the reverse process also happens when a free electron recombines with a Hydrogen ion and emits photons in the UV, optical and IR due to de-excitation. In addition, when a free electron passes close to a proton, a free-free scatter (bremsstrahlung emission, see Section 2.2.1.1) occurs resulting in an emission of continuum spectrum. This emission is usually present in HII regions surrounding hot massive stars (e.g. Spitzer, 1978; Kennicutt & Chu, 1988).

2.1.1.2 Dust emission

Dust is one of the fundamental components of a galaxy, and plays an important role in the galaxy's evolution. The presence of dust in the Universe can manifest itself in many ways, for instance, dust extinction (the absorption and scattering of starlight), polarization of the starlight arising from aligned dust grains, the presence of the IR emission, and interstellar gas depletion. The most widely accepted model of the dust in the interstellar environment suggests that there are different dust populations: ranging from silicate and graphite with sizes between 0.5 μm and a few angstroms to macromolecules granularly known as polycyclic aromatic hydrocarbons (PAHs). The spatial distribution of the dust is also important to model the dust, and can be categorized in four environments according to the distance from the radiating sources. These are: i) the circumstellar environment; ii) interstellar dust; iii) dusty torii around AGN; and iv) intergalactic dust. A population of dust grains is stochastically heated by the surrounding diffused radiation field and is re-emitted in the mid-IR. This can be observed in the Milky Way and other external galaxies spectra. Studies suggest that dust is responsible for absorbing at least 30% of the energy emitted as starlight in the Universe and re-radiating it in the infrared (Bernstein et al., 2002c).

2.1.1.3 Additional sources

AGN

AGNs have a broadband spectrum emissions from radio to γ-ray, thus they contribute to the EBL. However, their contribution to the EBL spectrum is usually ignored in the EBL models, since it is believed to be a minor contribution (Madau & Pozzetti, 2000). A significant part of radiation from AGNs is produced during the accretion of matter by the massive central black hole. For example, for a black hole with average mass density $\rho \simeq 3 \pm 2 \times 10^6$ h $M_{\odot}\mathrm{Mpc}^{-3}$ (Madau & Pozzetti, 2000). Therefore, at a mean redshift distribution ($\langle z \rangle \sim 2$), only 10 to 20% of the total EBL can be expected from AGNs contribution, which is relatively small (Hauser & Dwek, 2001).

Brown dwarfs & primordial particles

Brown dwarfs are objects that are not massive enough ($< 0.08\,M_{\odot}$) for Hydrogen to start burning to form stars. The expected contribution to the EBL, if we hypothetically assume that all the dark matter that is required for a closed universe is in the form of brown dwarfs, would be at most $3\,\mathrm{nWm^{-2}sr^{-1}}$ in the range between 10-100 μm (Burrows & Liebert, 1993). This is a small contribution compared to $\sim 40\,\mathrm{nWm^{-2}sr^{-1}}$ from a normal galaxy.

There are a lot of speculative theories about the existence of primordial particles. However, the suggested radiative output from their decay depends on the particle mass, their number density and distribution at specific redshift. Various intensity ranges can be obtained from these hypothetical particles (Bond et al., 1986; McDonald et al., 2001), but, no physical motivation can be used to distinguish between them. Therefore, the contribution from hypothetical primordial particles has been neglected.

2.1.2 Measurements of the EBL

Although it is very difficult to measure the EBL due to its weakness (diffuse nature) and the foreground emissions, efforts have been made to measure the the intensity directly and indirectly. In this section we will discuss the techniques that are used in measuring the EBL. For a detailed review see Hauser & Dwek (2001); Dwek & Krennrich (2013), and references therein.

2.1.2.1 Direct measurements

Measuring the EBL is very challenging because of the contamination due to the foreground emissions from the Milky Way and zodiacal light (light that is reflected from the Sun), which are brighter than the EBL in most of the UV and optical regimes (Hauser & Dwek, 2001). In the IR, a major contamination is caused by the interplanetary dust which contributes to most of the wavelengths. While a significant contamination in the near IR and optical comes from the starlight in our galaxy. As a result, a reliable measurement of the EBL requires a careful modelling of all the foreground components and removing them from the measurement. Moreover, technical (instrumental) difficulties in maintaining the calibration of the zero-point of detectors add more challenges.

Sky brightness

The common approach to measure the EBL has been to observe the total brightness of the sky (at a certain wavelength), and subtract the foreground contamination from the known sources, what is left would be the EBL. Fig. 2.3 shows the steps of extracting the EBL using this technique. Deep field observations of the Hubble Space Telescope (HST) simultaneously with ground-based observations by Bernstein et al. (2002a,b) provided measurements of the EBL with $1 - 2\sigma$ detection limit. Table 2.1 shows some of the measurements using this techniques (the data was adopted from Hauser & Dwek (2001)).

In the IR regime, there were many attempts to measure the background emission using rockets (Matsumoto et al., 1988; Kawada et al., 1994). However,

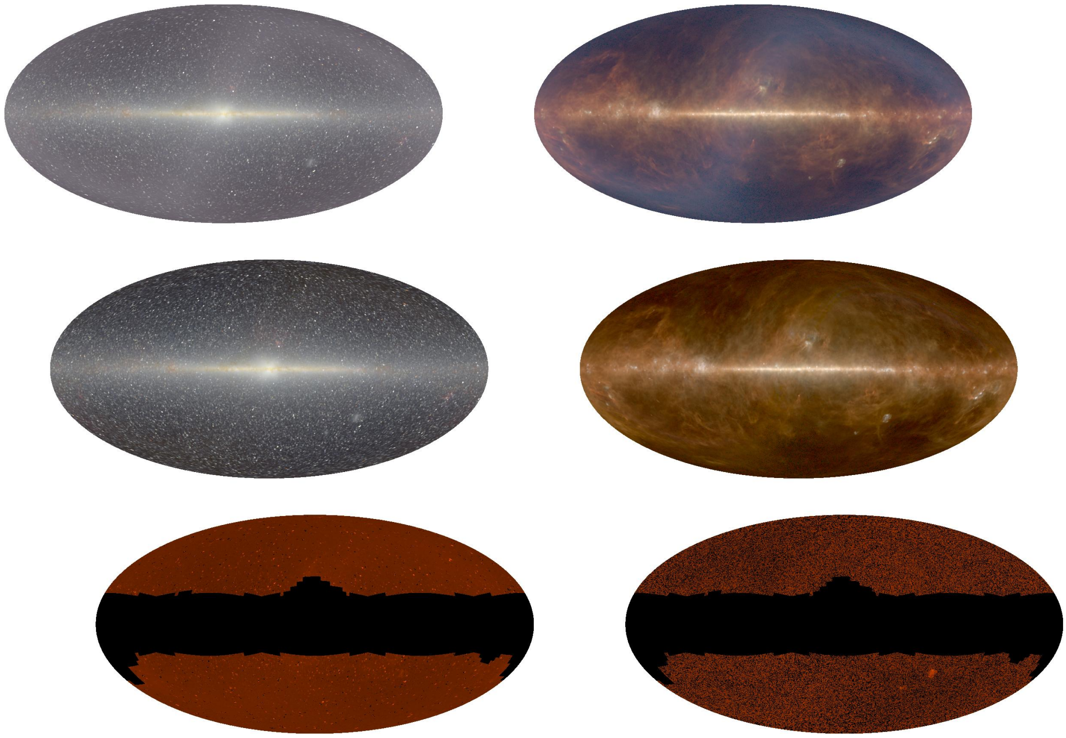

(a) (b)

Figure 2.3: (a) The top map shows a 3 colour image of the full sky CIB map (blue = 1.25 μm, green = 2.2 μm and blue = 3.5 μm). The middle map shows the same image after subtracting the zodiacal light. The bottom map shows what is left after subtracting the galactic foreground using the technique discussed in Dwek & Arendt (1998). However, this subtraction technique is unreliable near the Galactic plane, so this area has been masked out. The lowest levels for the upper and middle images are 3.95, 6.67, and 7.08 kJy/sr at 3.5, 2.2, and 1.25 μm respectively, but 0.395 kJy/sr for the lower image.
(b) The same maps as in (a), but different wavelengths (blue = 60 μm, green = 100 μm and red = 240 μm) and different technique to subtract the galactic foreground (see, Arendt et al., 1998). The lowest level for the upper and middle images are 223.2, 555.3, and 508.2 at 240, 100, and 60 μm respectively, but 30.7 kJy/sr for the lower image. The image has been adopted form: `http://www.astro.ucla.edu/~wright/CIBR/images.html`

Table 2.1: The upper limits of the EBL derived using sky brightness measurements technique. The data is adopted from Hauser & Dwek (2001).

λ (μ m)	νL_ν (nWm^{-2}sr^{-1})	References
0.10	< 11	Edelstein et al. (2000); Murthy et al. (1999)
0.1595	$14(10 \pm 2)$	Brown et al. (2000)
0.165	$7.0(5.6 \pm 0.7)$	Martin et al. (1991)
0.3	$22.2 - 27.3$	Mattila (2003)
0.4	$< 46(26 \pm 10)$	Mattila (1990)
0.44	$< 60(10 \pm 25)$	Toller (1983); Leinert et al. (1998)
0.5115	$< 48(30 \pm 9)$	Dube et al. (1979); Leinert et al. (1998)
0.550	$84.7 - 113.9$	Mattila (2003)
0.814	$84.8 - 114.2$	Mattila (2003)

these measurements suffered from systematic errors such as thermal emission from the rockets that contaminates the measurements in addition to the limitation in the observation time. In the year 1983 the Infrared Astronomy Satellite (IRAS) was launched to conduct a full sky survey in five wavelengths from mid- to far-IR. However, due to the uncertainties in the flux measurements (zero-point calibration) IRAS was not able to claim detection of the EBL (Rowan-Robinson et al., 1990).

Subsequent measurements by the Diffuse Infrared Background Experiment (DIRBE) and the Far-Infrared Absolute Spectrophotometer (FIRAS) on-board the Cosmic Background Explorer (COBE) satellite were able to provide robust measurements of the EBL in the IR. DIRBE was designed to measure the diffuse IR background in 10 different wavelengths distributed between 1.25 and 240 μm, where the contamination from the zodiacal light is minimum (Hauser & Dwek, 2001). Although, these experiments suffer from the sky subtraction uncertainties, they provided an important upper limit on the EBL.

Source count

Integrating the light from all galaxies within a given magnitude per unit sky area can be used to set a lower EBL limit. In order for this technique to provide meaningful results, it is necessary that the integrated flux converges. From a technical point of view, the convergence is achieved when the slope of the logarithmic differential galaxy count at that specific magnitude ($d \log N/dm$) is less than 0.4 at the faintest possible magnitude (Hauser & Dwek, 2001).

The major restriction for this method is due to detection limits and resolution of the instrument used, and there is also a possibility of significant

Table 2.2: The lower limits of the EBL derived from source count measurements. The data is adopted from Hauser & Dwek (2001).

λ (μ m)	νL_ν (nWm^{-2}sr^{-1})	References
0.01595	$> 2.9^{+0.6}_{-0.4}$	Gardner et al. (2000)
0.2365	$3.6^{+0.7}_{-0.5}$	Gardner et al. (2000)
0.36	$2.9^{+0.6}_{-0.4}$	Madau & Pozzetti (2000)
0.45	$4.6^{+0.7}_{-0.5}$	Madau & Pozzetti (2000)
0.67	$6.7^{+1.3}_{-0.9}$	Madau & Pozzetti (2000)
0.81	$8.0^{+1.6}_{-0.9}$	Madau & Pozzetti (2000)
1.1	$9.7^{+3.0}_{-1.9}$	Madau & Pozzetti (2000)
1.6	$9.0^{+2.6}_{-1.7}$	Madau & Pozzetti (2000)
2.2	$7.9^{+2.0}_{-1.2}$	Madau & Pozzetti (2000)

contribution coming from unresolved galaxies or low surface brightness galaxies that are below the detection limit. Moreover, the possibility of a truly diffused mechanism that contributes to the total EBL density cannot be accounted for with this method. In fact, Bernstein (2007) showed that it is possible to miss 50% or even more with a simple aperture photometry from the light that comes from extended sources, because of the difficulty to resolve faint galaxies from the background.

While Hubble Deep Field (HDF) set a lower EBL limit at $0.4 - 1\,\mu$m range (Madau & Pozzetti, 2000), the Two-micron All Sky Survey (2MASS) extended the range up to $3\,\mu$m. The derived lower limit from their observations is much lower than that given in Bernstein (2007), which could be due either to an underestimation of integrating the light from faint sources by HST or unresolvable diffuse sources. Continuous efforts by the Space Telescope Imaging Spectrograph (STIS) on board HST have extended the measurements to the shorter UV wavelengths. Table 2.2 shows the measurements of Madau & Pozzetti (2000) & Gardner et al. (2000).

Fluctuation analysis

Studying the EBL fluctuations does not provide absolute measurements of the background radiation, however, it can be used to constrain the EBL intensity. Combining the fluctuations measurements with other methods such as source count can provide a constrain on the light from unresolved sources. Using this method an upper limit on the EBL was derived by Kashlinsky et al. (1996b) from DIRBE analysis in the near-IR band. Additional studies have expanded the work including all DIRBE bands upto mid-IR, where it is very difficult

Table 2.3: The measurements of the EBL in IR derived using fluctuations analysis technique, $\delta\nu L_\nu$ is the variance. The data is adopted from Hauser & Dwek (2001); Kashlinsky (2005).

λ (μ m)	$\delta\nu L_\nu$ (nWm^{-2}sr^{-1})	νI_ν
1.25	$> 15.5^{+3.7}_{-7.0}$	< 200
2.2	$5.9^{+1.6}_{-3.7}$	78
3.5	$2.4^{+0.5}_{-0.9}$	< 26
1.9	$2.0^{+0.25}_{-0.5}$	< 13
12	$\lesssim 1$	< 15
25	$\lesssim 0.5$	< 8
60	$\lesssim 0.7$	< 12
100	$\lesssim 1$	< 17

to directly use photometry due to the zodiacal light (Kashlinsky et al., 1996c; Kashlinsky & Odenwald, 2000).

Furthermore, the EBL fluctuations at 170 μm measured by Infrared Space Observatory (ISO) were investigated by Matsuhara et al. (2000) including flux from sources under the detection threshold of the instrument, and provided a lower limit lower than that of Kashlinsky et al. (1996c) and Kashlinsky & Odenwald (2000). Table 2.3 shows the EBL measurements with uncertainties using this method, the data is adopted from (Hauser & Dwek, 2001; Kashlinsky, 2005).

2.1.2.2 Indirect observation

As mentioned above direct measurements of the EBL are very difficult because of the bright foreground. However, the VHE γ rays emitted at cosmological distances can penetrate most of the obstacles (dust in the Milky Way and the solar system) along their path. As these γ rays pass through the radiation field of the EBL they interact with the EBL via pair-production (see Section 2.2.2.2) thereby attenuating the γ-ray spectrum. The attenuation depends on both distance and energy of the source. Because of this, the EBL leaves its imprint in the observed spectrum of the VHE γ-ray. Therefore, in principle if we know the intrinsic γ-ray (emitted) spectrum, we can determine the intervening EBL intensity by comparing the intrinsic spectrum with the observed spectrum. Several studies have used this method to determine an upper limit on the EBL density (e.g., Stanev & Franceschini, 1998; Aharonian et al., 2006; Guy et al., 2000; Schroedter, 2005; Mazin & Raue, 2007; Orr et al., 2011). Although, this method is very useful to constrain the EBL, the true EBL spectrum cannot

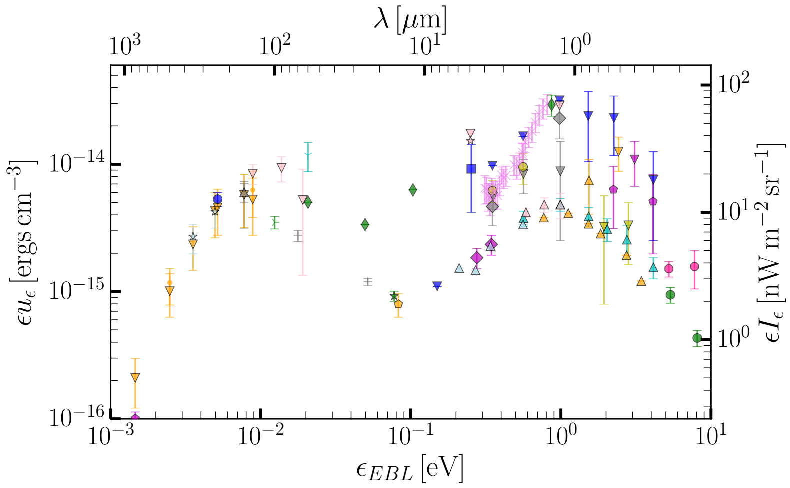

Figure 2.4: EBL measurements from various studies are represented as follows: green circle (Xu et al., 2005); red octagon (Gardner et al., 2000); blue triangle down (Bernstein, 2007); cyan triangle up (Totani et al., 2001); magenta triangle down (Mattila, 1990); yellow triangle down (Matsuoka et al., 2011); orange triangle down (Dube et al., 1979); grey triangle down (Levenson et al., 2007); pink triangle up (Keenan et al., 2010); magenta diamond (Ashby et al., 2013); blue square (Arendt & Dwek, 2003); orange pentagon (Hopwood et al., 2010); green star (Teplitz et al., 2011); grey plus (Béthermin et al., 2010); cyan triangle down (Finkbeiner et al., 2000); pink triangle down (Matsuura et al., 2011); green triangle up (Berta et al., 2011); orange triangle down (Fixsen et al., 1998); grey triangle down (Pénin et al., 2012); red star (Béthermin et al., 2012); orange dot (Odegard et al., 2007); blue circle (Zemcov et al., 2010); the yellow x (Matsumoto et al., 2005); green diamonds (Kashlinsky & Odenwald, 2000).

be assured due the uncertainties in the intrinsic γ-ray spectrum. With the advent of the current γ-ray telescopes the sample of the VHE sources has now increased, providing better constraints on the VHE spectrum.

To summarize, despite the impediments to accurately measure the EBL intensity, detections and limits on the EBL have been acquired via direct and indirect methods using ground- and space-based instruments. These observations are able to resolve the foreground contamination emission from Galactic sources. However, further observations are needed to constrain the zodiacal light, or even preform observation outside our solar system, which will eliminate any Fraunhofer lines, to obtain the absolute measurement of the EBL. Figure 2.4 shows a summary of the EBL observations using all the techniques discussed above.

2.1.3 Modelling the EBL

Due to the uncertainties involved in direct measurements of the EBL intensity, several methods have been developed to model the EBL. These models are based on our understanding of galaxy properties and star formation rates while incorporating observational constraints.

A good understanding of these models are also very important since they provide knowledge on many issues related to the evolution of EBL. The integrated intensity of the modelled EBL will provide limits on the evolution of the energy released throughout the cosmic history of the Universe. The spectral intensity I_ν offers more detail about the different contributors to the EBL such as; stars, dust, AGNs etc., and their relative contribution and evolution. The observed spectral intensity at a frequency ν_0 can be given as the integration over the expected sources luminosities (Peebles, 1993):

$$I_\nu = \frac{c}{4\pi} \int_0^\infty \mathcal{L}_\nu(\nu', z) \left| \frac{dt}{dz} \right| dz, \tag{2.1}$$

where $\mathcal{L}_\nu(\nu, z)$ is the spectral luminosity density, and $\nu' = \nu(1+z)$. The luminosity density $\mathcal{L}$ can be written as a convolution between the star formation rate (ρ) and the bolometric luminosity per unit mass $L_b(t)$ (Hauser & Dwek, 2001),

$$\mathcal{L} = \int_0^t \rho(\tau) L_b(t-\tau) d\tau, \tag{2.2}$$

In the following sections we will discuss four different approaches to model the EBL as categorized by Dwek & Krennrich (2013): backward evolution (BE), forward evolution (FE), semi-analytic evolution (SA) and cosmic chemical evolution (CCE) models. Most of the information in this section is obtained from Hauser & Dwek (2001); Dwek & Krennrich (2013); and Dwek (2001).

2.1.3.1 Backward evolution models

Generally backward evolution (BE) models use the observed spectral properties of galaxies in the local Universe and extrapolate it to higher redshifts. They also use the evolutions of parameters observed in the local Universe as constraints. The simplest BE models ignore the evolution in the galaxies comoving number density and in the SED of galaxies, in other words, they are independent of redshift (Lagache et al., 2005; Rodighiero et al., 2010). In order to compute the EBL one needs to integrate the local luminosity density over redshift up to where the first galaxies started to form, z_{max}. The difference between various BE models arise in determining the $\mathcal{L}(\nu)$ at different bands, for e.g, from UV-optical-near-infrared and mid-to far-infrared. More sophisticated BE models consider evolution in the LF estimation (e.g. Chary & Elbaz (2001); Rowan-Robinson (2001); Domínguez (2011)). Fig. 2.5 shows the resulting spectra of different BE models with respect to the observed data.

BE models are the simplest models and they can easily be compared with observations. However, they are not fully constrained by physical processes, e.g. radiative processes or star formation.

2.1.3.2 Forward evolution models

Forward evolution (FE) models go one step further to overcome some of the simplifications of the BE models by involving more physical processes in the prediction of the EBL density. FE models take the evolution of the stellar population into account using programs and libraries that track spectral evolution. They also calculate metallicity, stellar and gas content of galaxies, and their impact on the resulting SED. The general formula for the photon density ϵ at epoch t_z since the stars turned on at t_*, or redshift z, can be written as Dwek & et al. (1998):

$$\epsilon(t_z) = \int_{t_*}^{t_z} \psi(t)dt \int_{M_{\text{low}}}^{M_{t'}} L(m, t')\phi(m)dm, \tag{2.3}$$

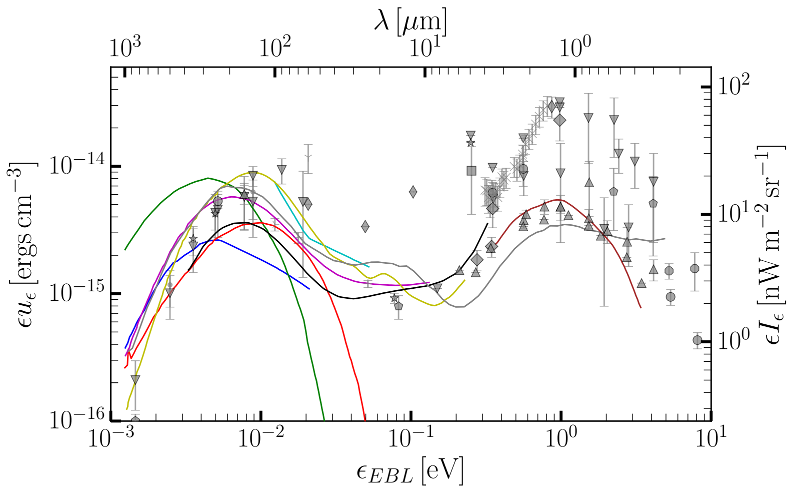

Figure 2.5: The EBL as predicted by different BE models. The solid blue line represents the model by Beichman & Helou (1991); solid cyan line is the model by Hacking & Soifer (1991); the black line is the model by Malkan & Stecker (1998); the green and red lines are the models by Blain & Longair (1993); the solid yellow line is the model by Xu (2000); magenta line is model by Tan et al. (1999); blue and green lines is the (RR) model by Rowan-Robinson (2001) and the brown solid line is the model by Yoshii & Takahara (1988). The models in this figure were adapted from Hauser & Dwek (2001).

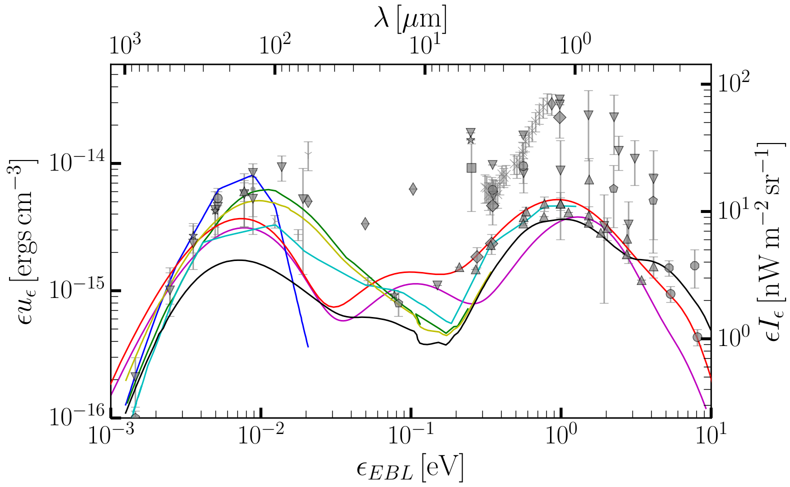

Figure 2.6: The EBL as predicted by different FE models. Where the cyan solid line represents the model by Franceschini et al. (1994); solid blue line by Calzetti & Heckman (1999); green, yellow, black solid lines are models by Dwek (1998); red solid lines by Finke et al. (2010), magenta solid line by Kudoda & Faltenbacher (2017). The models in this figure are adapted from Hauser & Dwek (2001) with the exception of Kudoda & Faltenbacher (2017).

where $\psi(t)$ and $L(m, t')$ are the global star formation rate and luminosity of a star with mass m at time $t' = t_z - t$, respectively, and $\phi(m)$ is the stellar IMF normalized to unity in the $(M_{\rm low}, M_{t'})$, and $M_{t'}$ is the initial main-sequence mass of a star with a lifetime t'. The intensity of the EBL can then be described as:

$$I = \left(\frac{c}{4\pi}\right) \int_0^z \epsilon(z) \left|\frac{dt}{dz}\right| \frac{dz}{1+z}. \tag{2.4}$$

The difference between various FE models lies in the complexity of modelling the stellar and dust components in the EBL. Some FEs use radiative transfer models (e.g. Silva et al., 1998; Gordon et al., 2001) to determine the SED of the galaxy, while others use analytic and observationally motivated recipes (see Dwek & Krennrich, 2013, and references therein). Fig. 2.6 shows different spectra of FE models with respect to observations.

Even though FE models have solved some of the simplifications of BE models and managed to predict the observed EBL using some free parameters, they have their own shortcomings. For example, their inability to track galaxy interactions, morphological evolution of galaxies and starburst phases.

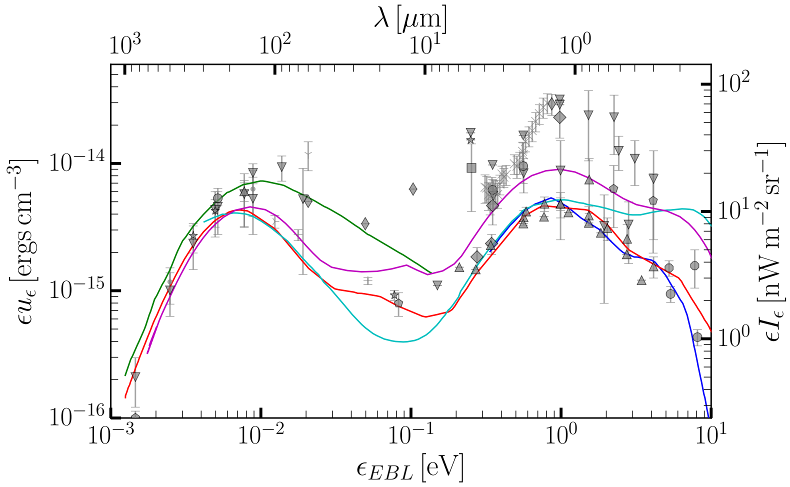

Figure 2.7: The EBL as predicted by different SAMs. The magenta line represents the model by Primack et al. (1999); the red line represents the model by Devriendt & Guiderdoni (2000); and the blue line represents the model by Blain et al. (1999). The models in this figure have been adapted from Hauser & Dwek (2001)

2.1.3.3 Semi-analytic evolution models

Semi-analytic evolution models (SAMs) begin with simulating the structure formation using the cold dark matter cosmological framework and apply numerical recipes to populate the gravitationally formed structures with galaxies. They are developed to overcome some of the shortcomings of the FE models. SAMs follow the merger-trees of the dark matter halos and apply physically motivated recipes to describe heating and cooling processes, feedback and chemical enrichment of the ISM and IGM.

The outcomes of SAMs are by construction in agreement with various observed properties of galaxy populations such as morphology mix, SEDs, star formation histories, luminosity functions in different wavebands and for various redshifts (Fontanot et al., 2009; Fontanot & Somerville, 2011; Somerville et al., 2012; Younger & Hopkins, 2011). Despite the involvement of a large number of parameters, simplified algorithms, and high level of complexity, SAMs are the most physically motivated of the models discussed in this section (Dwek & Krennrich, 2013). Fig. 2.7 shows some of SAMs models and compares it with observed EBL data.

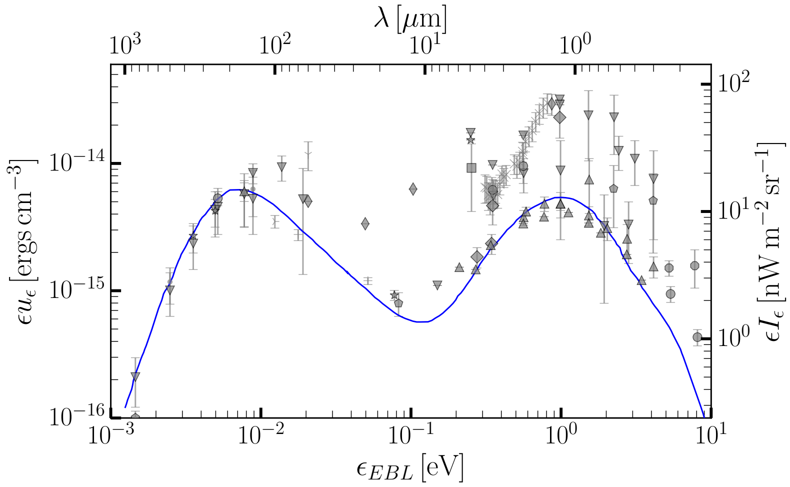

Figure 2.8: The EBL as predicted by a CCE model (blue line) by Pei et al. (1999). The model in this figure is adapted from Hauser & Dwek (2001).

2.1.3.4 Cosmic chemical evolution models

Cosmic Chemical evolution (CCE) models treat the whole universe as one closed system and represent all galaxies in large comoving volumes by their basic elements: gas, stars, radiation, and metallicity. Chemical evolution equations are applied to track the chemical evolution of galaxies within the comoving volume element. These models particularly focus on the average properties over the global galaxy population. The first CCE model was developed by Pei & Fall (1995). Their model use the rest-frame UV emissivity as a function of redshift and the properties of the ISM as inputs. Using these inputs they obtain a solution for the evolution of the cosmic star formation rate. Similar to the FE models, stellar emissivity is calculated using population synthesis models. These models apply an extinction law to determine the amount of starlight absorbed by the dust, and redistribute the dust according to its temperature (Dwek & Krennrich, 2013). Fig. 2.8 shows the resulting EBL spectrum of Pei et al. (1999) compared to observations.

2.1.4 EBL as cosmological probe

The discussion above already made clear that the EBL comprises a wealth of cosmological and astrophysical information. In this section we will cover some of these aspects.

2.1.4.1 EBL total energy density

The total energy density of the EBL is directly related to all physical processes involved in its emission and can be used to constrain these processes. Hauser & Dwek (2001) calculated the total EBL energy density relative to the critical energy density by using the dimensionless representation of the EBL energy density $\Omega_{\rm EBL}$:

$$\Omega_{\rm EBL} = \frac{4\pi}{c}\frac{I_{\rm EBL}}{\rho_c c^2} \sim 10^{-6} - 10^{-5}, \qquad (2.5)$$

which is small relative to the CMB ($\Omega_{\rm EBL}/\Omega_{\rm CMB} \sim 0.1$)

2.1.4.2 Element production

As mentioned before, stars are not only the main contributor to the EBL energy density, but also convert Hydrogen to heavier elements to generate energy. This reaction liberates 0.7% of the rest mass of the converted Hydrogen into energy. Therefore, we can directly link the observed EBL energy density to the amount of Hydrogen that is converted to other heavier elements Hauser & Dwek (2001):

$$\Delta X \simeq 2 \times 10^{-4} \times I_{\rm EBL} \;\; [\rm nWm^{-2}sr^{-1}], \qquad (2.6)$$

where $\Delta X = \rho_{\Delta X}/\rho_b = \Omega_{\Delta X}/\Omega_b$ is the fraction of Hydrogen that is converted to heavier elements, ρ_b is the baryonic density matter and Ω_b is the fraction of the baryonic to critical density ($= 1.92 \pm 0.18 \times 10^{-2} h^{-2}$, Olive et al., 2000). Considering the EBL intensity in the range $43 - 175\,\rm nWm^{-2}sr^{-1}$ implies that roughly $2\% - 6\%$ of the total Hydrogen in the Universe is consumed in powering stars throughout cosmic history (e.g. Hauser & Dwek, 2001).

2.1.4.3 Star formation rate

Understanding the star formation history is essential in constraining the structure formation models in the Universe. From spectroscopic studies and galaxy surveys, a uniform picture of the star formation rate (SFR) can be derived (Hopkins et al., 2001; Kennicutt, 1998; Madau et al., 1996). The observed comoving space density $\dot{\rho}_*$ of the SFR in galaxies rises by one order of magnitude from $z = 0$ to $z = 1$ and it stays almost constant between $1 < z < 2$, with a peak around $z \sim 1.5$. However, at higher redshifts the behaviour of the SRF

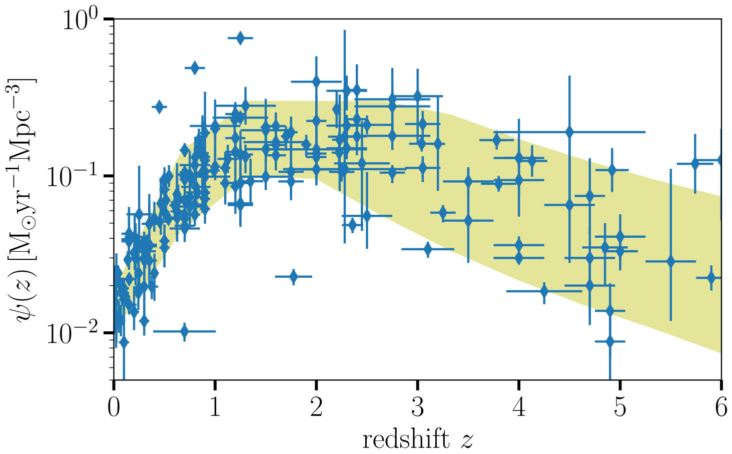

Figure 2.9: The cosmic star formation rate derived from H_α, Ly_α, radio sub-millimetre, MIR, and UV observations. The shaded area represents an analytic approximation for the upper and lower limits. The figure is reproduced from Dwek & Krennrich (2013).

is still not clear, i.e., whether it remains constant or decreases at much higher redshifts (see Fig. 2.9).

As discussed in Section 2.1.1.1 starlight dominates the EBL comoving luminosity density $\mathcal{L}$. Therefore, it is self-evident to assume a strong relation between the SFR and EBL, as shown in eq. 2.1 and eq. 2.2.

2.1.4.4 The radio-IR background relation

The emission from H II regions around massive hot stars in star forming galaxies in radio and IR through free-free mechanism (bremsstrahlung) can be used to establish a connection between the IR and radio emissions (Hauser & Dwek, 2001). This correlation has been confirmed through observations (Helou, 1991). However, in AGNs the radio emission is attributed to different processes, and therefore, such correlation is neither observed nor expected.

The correlation in star-forming galaxies is used to derive 50% of the CRB at 170 cm, while 50% of the CRB at 75 cm can be attributed to AGN-like radio sources. Both contributors are consistent with models for the origin of the CRB (Haarsma & Partridge, 1998).

2.2 HIGH ENERGY γ-RAY ASTROPHYSICS

Since the focus of this thesis is to model the γ-ray path over cosmological distances, we will provide a brief introduction on the origin of γ-ray emission, production mechanisms, the possible interactions along their path to the observer, and observation techniques.

2.2.1 Production mechanisms

The different mechanisms that can produce photons in general can be categorized in two main branches: thermal and non-thermal emissions. For γ rays we can rule out thermal emission mechanisms because in order for a black-body spectrum to peak at γ-ray energies, the associated temperature must be roughly 10^{10} K (six orders of magnitude higher than our Sun). Such high temperatures are not found in the observable Universe. Therefore, in what follows we only discuss main emission mechanisms relevant to VHE: bremsstrahlung, synchrotron, inverse Compton scattering, pion decay, and annihilation.

2.2.1.1 Bremsstrahlung radiation

Bremsstrahlung or braking radiation occurs when a charged particle is accelerated or decelerated due to an external electric field. For instance, when an electron traversing through matter passes very close to the nucleus of an atom, a deflection in the electron's original trajectory happens due to the nuclear electric field (see Fig. 2.10a). As a result, the electron loses energy in a form of photon with energy $E_\gamma \simeq E_e/2$. The differential cross-section of bremsstrahlung scattering can be written as:

$$d\sigma_{bra} = 4Z^2\alpha r_0^2 \frac{dk}{k} E_i^{-2} \left[(E_i^2 + E_f^2) - \frac{2}{3}E_i E_f\right] \left[\ln\left(\frac{2E_i E_f}{k}\right) - \frac{1}{2}\right], \qquad (2.7)$$

where r_0, α are the classical electron radius and fine structure constant, respectively. k is the momentum of the photon and is the difference between the electron's initial E_i and final E_f energies. The number of photon N_γ emitted within the momentum dk at time dt when an electron passing close to atoms or ions with corresponding number densities n_s can be written as (Blumenthal & Gould, 1970):

$$\frac{dN_\gamma}{dtdk} = c\sum_s n_s \frac{d\sigma_{bra}}{dk}. \qquad (2.8)$$

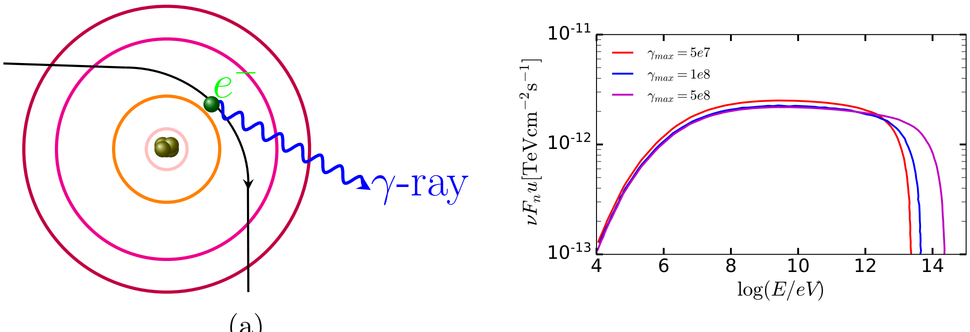

Figure 2.10: The left panel provides a schematic of the bremsstrahlung process. As the electrons e^- passes close to a nucleus it gets deflected and loses some of its energy in the form of γ-ray. The right panel provides the spectrum emitted by bremsstrahlung assuming a power-law energy distribution of three different populations of electrons with different maximum energy. The figure is reproduced from (Saha, 2014).

The total spectrum of bremsstrahlung as result of energetic electrons with distribution (dN_e/dE) is given by:

$$\left(\frac{dN_\gamma}{dtdk}\right)_{total} = \int dE \frac{dN_e}{dE}\frac{dN_\gamma}{dtdk}. \tag{2.9}$$

This process is very important in many aspects of astrophysics. Fig. 2.10b shows the emitted spectrum for three different populations of electrons that has energy distribution follow a power-law $dN_e/dE \propto \gamma^{-2.1}$ with different maximum energies. In the case of relativistic electrons (with energy E) interacting with molecules or atoms, photons with maximum frequency are emitted. The average energy of the emitted photons is around a third of the electron energy. In general, a power-law photon energy spectrum emitted by this interaction will have the same power-law of the interacted electrons, and it is very important in understanding the low energy γ-ray emitted in the ISM (Strong et al., 2000).

2.2.1.2 Synchrotron radiation

Synchrotron emission occurs when a charged particle (with a mass m) changes its direction due to an external magnetic field B. Synchrotron radiation is emitted in the tangential direction to the trajectory of the charged particle in a narrow cone shape. The spectrum of the synchrotron emission can be written as (Blumenthal & Gould, 1970):

$$\frac{d\mathcal{E}}{d\nu dt}_{sy} = \frac{\sqrt{3}e^3 B \sin\theta}{m_e c^2} \frac{\nu}{\nu_c} \int_{\nu/\nu_c}^{\infty} K_{5/3}(x)dx, \tag{2.10}$$

where

$$\nu_c = \begin{cases} \frac{3e\gamma^2}{4\pi m_e c} B \sin\theta & \text{for electrons,} \\ \frac{3e\gamma^2}{4\pi m_p c} B \sin\theta & \text{for protons,} \end{cases} \tag{2.11}$$

is the characteristic frequency of the radiated emission, e is the charge of the electron, $K_{5/3}$ is the modified Bessel function of the order 5/3, and θ is the pitch angle between the direction of the magnetic field and the trajectory of the particle. The characteristic frequency of the photons emitted by electrons is $(m_p/m_e) \backsimeq 6 \times 10^9$ times higher than the characteristic frequency emitted by protons, which makes the electron synchrotron emission more relevant in high energy astrophysics.

Averaging over the pitch angle ($< \sin\theta >= \sqrt{2/3}$), the total energy emitted through synchrotron emission from an electrons will be:

$$\mathcal{L}^{tot} = \int_1^{\infty} d\gamma \frac{dN_e}{d\gamma_e} \frac{d\mathcal{E}}{d\nu dt}_{sy}, \tag{2.12}$$

where $\mathcal{L}^{tot}$ and $\frac{dN_e}{d\gamma_e}$ are the total spectral energy and the energy spectrum of the electrons, respectively. Figures 2.11a and 2.11b show a schematic of synchrotron process and the characteristic synchrotron spectrum of electrons with an energy distribution following a power-law ($dN_e/d\gamma \propto \gamma^{-2.1}$) for three values of magnetic field (dashed lines) and the same magnetic field with different maximum energy for the electrons (solid lines). Synchrotron radiation is common in astrophysics. We can observe synchrotron radiation as radio emission from supernova remnants, within the intrastellar medium of our Galaxy and from extragalactic radio sources as a result of relativistic electrons interacting with magnetic fields. In some cases of VHE sources, such as blazars, synchrotron emission produced by relativistic protons may be responsible for the TeV emission (Aharonian, 2000).

2.2.1.3 Inverse Compton scattering

Inverse Compton (IC) scattering occurs when a relativistic charged particle transfers some of its energy to a low energy photon (E_{ph}) through collision. As a result of this interaction the scattered photon could gain a significant

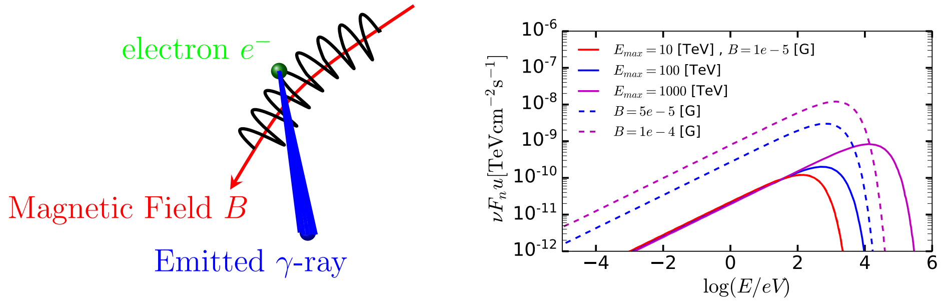

(a) (b)

Figure 2.11: The left panel shows a schematic diagram of the synchrotron emission mechanism. The right panel shows the resulting synchrotron spectrum of three different populations of electrons with the same magnetic field but different maximum energies in solid lines. The dashed lines represent emission when using the same energy distribution with a different magnetic field. The figure is replotted from Saha (2014)

amount of energy. Fig. 2.12a shows a schematic of the interaction. The energy E_γ of the γ-ray can be approximated as (e.g. Longair, 2011):

$$E_\gamma \simeq \frac{4}{3}\gamma^2 E_{ph}. \tag{2.13}$$

The expected energy spectrum of the γ-ray from this interaction is shown in Fig. 2.12b. This interaction occurs in places where there is a high number density of low energy photons and high energy (relativistic) charged particles. The spectrum of the photons emitted by IC can be written as (Blumenthal & Gould, 1970):

$$\frac{d\mathcal{E}}{d\nu dt}_{IC} = \frac{3\sigma_T c}{4\gamma^2} h^2 \nu \int_{h\nu/4\gamma^2}^{h\nu} d\epsilon \frac{n_b(\epsilon)}{\epsilon} f_{IC}(\epsilon, \nu, \gamma), \tag{2.14}$$

where $f_{IC}(\epsilon,\nu,\gamma) = 2q\ln q + (1+2q)(1-q) + \frac{1}{2}\frac{[4\epsilon\gamma q/(m_e c^2)]^2}{1+4\epsilon\gamma q/(m_e c^2)}(1-q)$, σ_T is the Thomson cross-section, $d\epsilon n_b(\epsilon)$ is the number density of the soft photons with energy between ϵ - $\epsilon + d\epsilon$, and $q = \frac{h\nu}{4\epsilon\gamma^2[1-h\nu/(\gamma m_e c^2)]}$. The total energy emitted by electrons with energy distributed $(dN_e/d\gamma)$ through IC process can be written as:

$$\mathcal{L}^{tot} = \int_1^\infty d\gamma \frac{dN_e}{d\gamma_e}\frac{d\mathcal{E}}{d\nu dt}_{IC}. \tag{2.15}$$

The low energy photons can be produced by several mechanisms such as

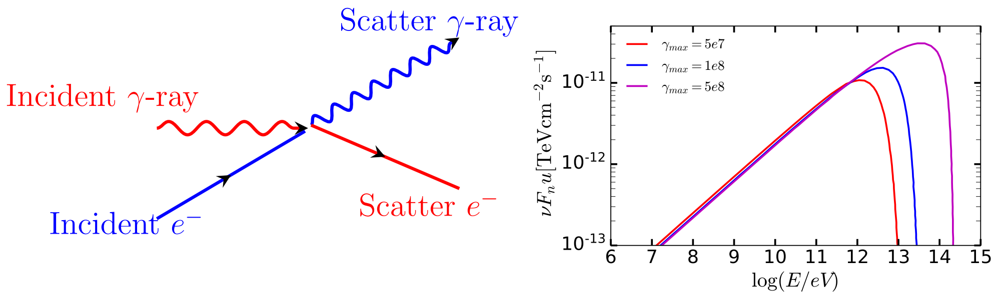

(a) (b)

Figure 2.12: The left panel shows a schematic diagram of inverse Compton interaction. The right panel shows the IC spectrum for different populations of electrons with different maximum energies. The figure is replotted from Saha (2014).

CMB photons, thermal emission from dust and synchrotron radiation by the same electron involved in the IC. If the high energy electrons interact with photon emitted by synchrotron radiation by the same electrons, it is known as synchrotron self Compton (SSC; see Section 2.2.5.1). Fig. 2.12b shows the IC spectrum produced by electrons with a spectrum ($dN_e/d\gamma \propto \gamma^{-2.1}$) with different maximum energies.

2.2.1.4 Pion decay

When a proton with high energy collides with the nuclei of atoms in the interstellar gas, different types of pions (π^+, π^0 and π^-) are produced. However, the neutral pions are not stable having a lifetime 8×10^{-17} s, and decay into two γ rays, each with half of the pion rest mass ~ 70 MeV. The other charged pions (π^+ and π^-) decay into positive and negative muons, while the latter decays into relativistic electron positron pair. The γ-ray spectrum as result of the pion decay can be written as (Kelner et al., 2006):

$$\frac{dN_\gamma}{dE_\gamma dt} = cn_H \int_{E_\gamma}^{\infty} \sigma_{inel}(E_p) \frac{dN_p}{dE_p} F_\gamma \left(\frac{E_\gamma}{dE_p}, E_p \right) \frac{dE_p}{E_p}, \tag{2.16}$$

where $F_\gamma(\frac{E_\gamma}{dE_p}, E_p)$ is the number of photons emitted per unit interval of $\frac{E_\gamma}{dE_p}$ per interaction between ambient protons and protons with energy E_p. $\sigma_{inel}(E_p) = 34.3 + 1.88L + 0.25L^2$[mb] is the inelastic cross-section of the p-p interaction with $L = \ln(E_p/1\text{TeV})$, and N_p is the number of the protons. The details of the spectrum model can be found in Kelner et al. (2006).

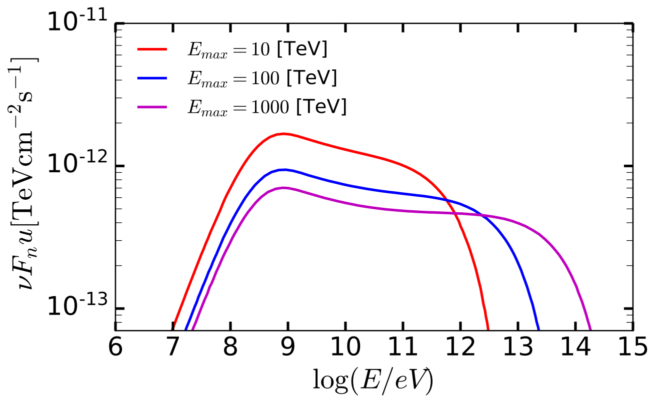

Figure 2.13: The spectrum emitted from pion decay as a result of the interaction between high energy protons (with power-law distribution but different maximum energies) and the ambient matter. The figure is replotted from Saha (2014).

Fig. 2.13 shows the spectrum of the γ-ray emitted by π^0 decay, which is computed using power-law for the energy distribution of protons ($\frac{dN_p}{dE_p} \propto E_p^{-2.1}$ where $E_p \leq E_{max}$) for different $E_{max} = 10, 100, 1000\,\mathrm{TeV}$.

2.2.1.5 Annihilation

Annihilation occurs when a particle and an antiparticle encounter each other and convert their masses into energy. The outcome of this interaction is usually a pair of photons, in some cases more pairs, depending on the particle-antiparticle angular momentum. The lightest particle-antiparticle pair that can be generated is an electron-positron pair, each with 511 keV rest mass. Detecting these photons is very important in high energy astrophysics because of the possibility of finding a signature of hypothetical massive particle annihilation which could be a candidate for dark matter.

2.2.2 γ-ray interaction with matter

The interaction of γ-ray with matter depends on the probability of the γ-ray encountering an electron or nucleus. While the probability of the interaction is determined by the density and atomic number of the material, the energy of the photon and the interaction cross-section, the energy of the γ-ray photons determines the type of interaction. The interaction of γ-ray with matter is important to study different kinds of astrophysical phenomena, as well as for γ-ray detection. In this section we will discuss the main modes of γ-ray

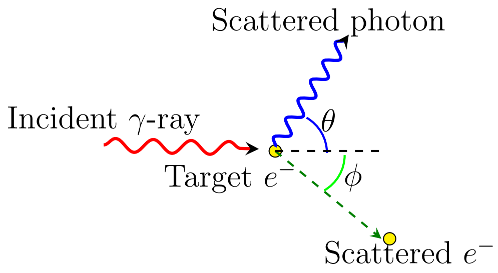

Figure 2.14: A schematic diagram of Compton scattering. θ and ϕ are the scattered angles of the photon and electron (e), respectively.

interactions with matter that are relevant to this thesis: Compton scattering and pair production.

2.2.2.1 Compton scattering

Compton scattering takes place when a γ-ray photon collide with a weakly bound electron or a free electron, and lose some of its energy to the electron. The cross-section of Compton scattering σ_C is given by the Klein-Nishina formula:

$$\sigma_{KN} = \pi r_0^2 \frac{1}{x}\left(\left[1 - \frac{2(x+1)}{x^2}\right]\ln(2x+1) + \frac{1}{2} + \frac{4}{x} - \frac{1}{2(2x+1)^2}\right), \qquad (2.17)$$

where $x = \hbar\omega/m_e c^2$. This interaction usually occurs in the range of 100 keV up to a few MeV. Fig. 2.14 shows a schematic of the Compton scattering (Note that the particle in this case is relativistic). In Compton scattering, the γ-ray photons require multiple interactions to lose all of their energy. If the photon energy at the electron rest frame is $\ll m_e c^2$, the interaction is called Thompson scattering. The cross-section σ_T is:

$$\sigma_T = \frac{8\pi}{3}\left(\frac{q^2}{4\pi\epsilon_0 m_e c^2}\right)^2 = \frac{8\pi}{3} r_0^2, \qquad (2.18)$$

where q is particle charge with a mass m, and r_0 is known as the classical radius of an electron. If the particle is an electron, the cross-section equals $6.6524 \times 10^{-25}\,\text{cm}^2$.

2.2.2.2 Pair production

When a γ-ray photon with energy more than double the rest mass of an electron (511 keV) passes through a strong electric field an electron-positron pair

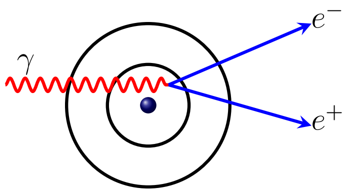

Figure 2.15: A schematic diagram of pair production. γ represents a photon with energy above 1.02 MeV interacting with nucleus field, and e^- and e^+ represent produced electron-positron pair.

can be created. The role of the field is to keep the energy and momentum simultaneously conserved. The field of a nucleus with high atomic number Z can be sufficient to provide the right environment. The probability of this interaction is proportional to the Z and the energy of the γ-ray photons. The cross-section of the this interaction σ_{pair} can be defined as (Longair, 2011):

$$\sigma_{pair} = \begin{cases} \alpha r_e^2 Z^2 \left[\frac{28}{9} \ln\left(\frac{2\hbar\omega}{m_e c^2}\right) - \frac{218}{27}\right] & \text{For } 1 \ll \hbar\omega/m_2c^2 \ll 1/\alpha Z^{1/3}, \\ \alpha r_e^2 Z^2 \left[\frac{28}{9} \ln\left(\frac{183}{Z^{1/3}}\right) - \frac{2}{27}\right] & \text{For } \hbar\omega/m_e c^2 \gg 1/\alpha Z^{1/3}, \end{cases} \tag{2.19}$$

For this interaction to occur the γ-ray photon and nucleus system must have more energy in the centre-of-momentum frame than the rest mass of produced pair ($\sim 1\,\text{MeV}$). The cross-section of this interaction is $\sim \alpha\sigma_T Z^2$, where α is fine structure constant. Fig. 2.15 shows a schematic diagram of the pair production mechanism. Pair production takes place at energies higher than the Compton interaction, where the γ-ray photon can lose all of its energy in a single interaction.

2.2.2.3 Electromagnetic cascades

Electromagnetic cascading (or showering) is not a type of interaction. Rather, it is a combination of different interactions. If a VHE γ-ray enters the Earth's atmosphere, it initiates a series of interactions and generates electron-positron pairs with high kinetic energy, which will emit high energy photons. The high energy photons in turn produce electron-positron pairs, and so on. Fig. 2.16 shows a diagram of the γ-ray cascading scenario. This phenomena is very important in γ-ray observations (we will see this in the following sections).

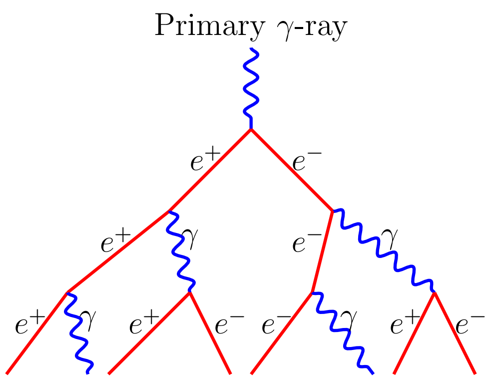

Figure 2.16: A schematic representation of electromagnetic cascades.

2.2.3 Observation of γ-rays

Astronomical observations depend on many factors such as the luminosity of the source (number of photons emitted) and the number of photons that can be collected. The latter depends on how far away the source is, what happens along the photons path to the observer, and the collecting area of the detector. In the case of γ-ray observations, the γ rays carry the highest energy in the electromagnetic spectrum; the energy in one γ-ray photon is equivalent to 10^6 up to 10^{14} times the energy of optical photons. This implies that even the most energetic processes in the universe can only produce relatively small amounts of γ rays, which limits the number of emitted photons. Moreover, the Earth's atmosphere is totally opaque to photons with a wavelength below 300 nm, making direct ground observation impossible.

One method to observe γ rays is from above the atmosphere level. Since the number of high energy γ rays decreases with an increase of their energy, a large collection area is needed. The current advancement in the development of instruments (satellites) with large collecting areas which are sensitive to higher energy photons allow us to observe γ-ray photons with energies less than ~ 100 GeV.

The first mission sent by NASA that carried a γ-ray detector was SAS-2 in 1972 (Derdeyn et al., 1972), it mapped the galactic plane and detected an isotropic γ-ray radiation in addition to discrete γ-ray sources. The COS-B satellite in 1975 launched by ESA (Bignami et al., 1975) confirmed the SAS-2 findings and expanded the discrete γ-ray sources catalogue. Later, Compton Gamma Ray Observatory (CGRO) was launched in 1991 with four detectors on board (EGRET, COMPTEL, OSSE and BATSE), each one designed to observe in specific energy regime (Gehrels et al., 1993). The latest γ-ray satellite, Fermi Large Area Telescope (Fermi LAT Atwood et al., 2009), has been surveying the high energy sky since 2008, increasing the γ-ray catalogue by more than a thousand new sources.

The second method is indirect observation from the ground. This is achieved by observing the interaction of the VHE γ-ray with our atmosphere. A primary particle with energy greater than a few GeV interacts with the atmosphere creating secondary particles (electron-positron pairs) which in turn interacts with the atmosphere, resulting in a cascade of particles and lower energy photons (as discussed in section 2.2.2.3). Gamma-ray telescopes detect these showers through the Cherenkov radiation as they propagate through the atmosphere with a speed higher than the speed of light in the medium. The amount of the Cherenkov shower produced is proportion to the primary particle energy. Generally, telescopes that use this technique are called Atmospheric Cherenkov Telescopes (ACT). Example of ACT include: Whipple Telescope (Weekes et al., 1989), High-Energy-Gamma-Ray Astronomy (HEGRA) (Mirzoyan et al., 1994), High Energy Stereoscopic System (HESS) (Hermann, 1997), Solar Tower Atmospheric Cherenkov Effect Experiment (STACEE) (Bhattacharya et al., 1997), Themistocle and CELESTE and Pachmarhi Array of Cherenkov Telescopes (PACT) (Bhat, 1999), Very Energetic Radiation Imaging Telescope Array System (VERITAS) (Krennrich et al., 2004), and Major Atmospheric Gamma-ray Imaging Cherenkov Telescope (MAGIC) (Cortina et al., 2009).

2.2.4 Astrophysical γ-ray sources

γ rays are expected to be emitted from the sources that are associated with energetic activities where particles are accelerated to high energies. In this section we will discuss γ rays from active galaxies since the emission from these sources is the focus of this thesis.

2.2.4.1 Active galactic nuclei

Active galactic nuclei (AGNs) refer to the central region of galaxies that harbour energetic phenomena and produce enormous amounts of radiation. The powerful radiation from AGNs is believed to be due to accretion of matter into a super massive black hole ($10^6 - 10^8\,M_\odot$ Longair (2011)) at the centre of the galaxy. As the black hole accretes matter from its surrounding, the in-falling material is highly accelerated. Conservation of the angular momentum forces, however, the in-falling matter to form an accretion disk rather than fall directly into the black hole. Matter is heated to high temperatures by dissipation in the accretion disk and radiated away. The emission from AGNs covers a wide range of energies from radio to γ-ray, and it is characteristically non-thermal.

Historically there are many AGN classifications based on their observational characteristics in different wavebands. One of the main recognized classifications is according to the strength of their radio emission: radio-loud and radio-quiet AGNs. There are subclasses in each type. Radio-quiet AGNs are classified into: radio quiet quasars, Seyfert type I and Seyfert type II. While radio-loud AGNs are classified into: radio loud quasars; FR I and FR II, low ionization narrow emission-line (LINERs) and Blazars. However, despite these classifications it is believed that the central region of AGNs are similar, and the historical distinction does not reflect their underlying physical properties. In the current AGN paradigm, different subclasses of AGNs are linked by the Unified model of AGNs (Urry & Padovani, 1995). According to this model AGNs can be classified into type 0, 1, and 2 AGNs. This classification is based on the orientation of the accretion disk and the obscuring dusty molecular torus around the AGN with respect to the line of sight of the observer.

In type 1 the axis of the torus is close to the line of sight, and the observer can see both broad-line (emitted from the high-velocity gas clouds orbiting close to the centre) and narrow-line (emitted from the low-velocity gas clouds relatively far form the centre). Whereas the orientation of the dust torus in type 2 blocks the nucleus from the view and we can only see the narrow-line. In the rare cases where the jet is pointing towards the observer, they are referred to as type 0 (Urry & Padovani, 1995). Fig. 2.17 shows a schematic of an AGN and the different classes, according to the Unified model. In the following sections we will concentrate on blazars and their interaction with the EBL.

2.2.4.2 Blazars

Blazars are a particularly interesting class of AGNs with their jet pointing towards the observer. This makes them appear extremely bright due to relativistic beaming. Blazars are characterized by a compact radio core, flat radio spectrum, high polarization, apparent superluminal motion, high energy emission, and rapid variability (Longair, 2011). Although Blazars constitute a small fraction of the total number of AGNs, they are major contributors of the extragalactic VHE emission. The spectral energy distribution of blazars contain two distinct humps, peaking in the IR- X-ray regime and in the MeV-TeV regime. The peaks are believed to be produced by synchrotron emission at low

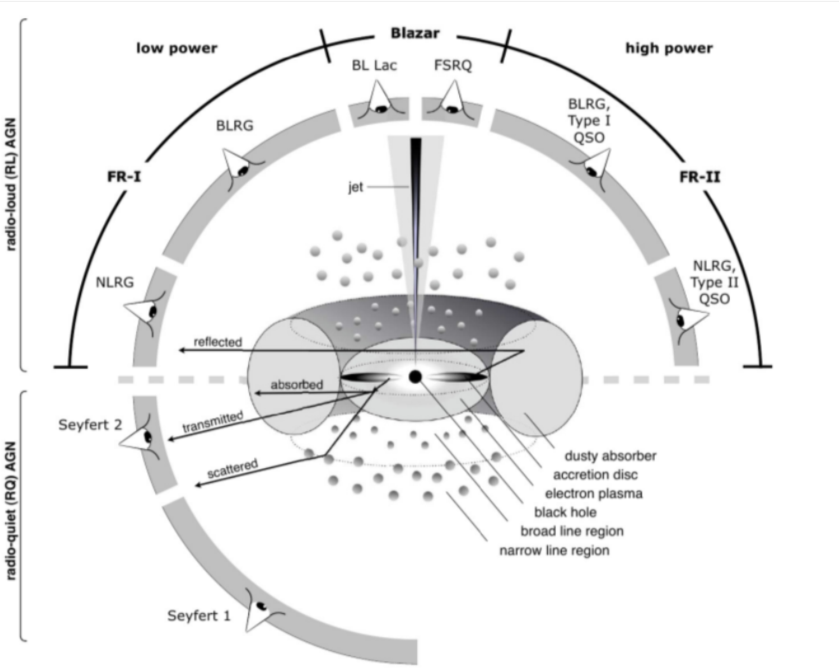

Figure 2.17: A schematic diagram of AGN from the Unified model point of view (Beckmann & Shrader, 2012). In Blazars the angle between the AGN's jet and line-of-sight is very small. In Seyfert I the angle is about 30° and the narrow-line and broad-line regions are observable; at larger angles these regions will be blocked by the torus with the corresponding class being Seyfert II. In the case of radio galaxies, the line-of-sight is perpendicular to the jet (which might be seen at low frequencies).

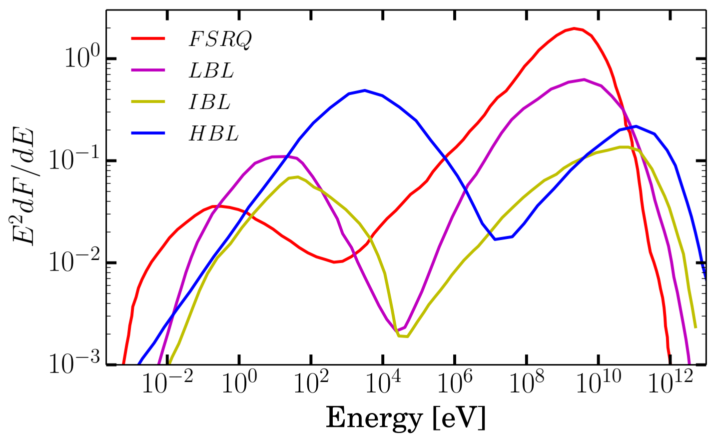

Figure 2.18: The normalize SED of the different types of blazars. The figure is replotted form Díaz (2011).

frequencies and inverse Compton at high energies (see e.g., Sikora et al., 1994). There are two general types of blazars: Flat-Spectrum Radio Quasars (FSRQ) and BL Lacertae (BL Lac). BL Lacs are further classified into high, intermediate, and low-frequency- peaked (HBL, IBL, and LBL) classes, respectively, depending on the location of the first peak (e.g. Padovani & Giommi, 1995). Fig. 2.18 shows a schematic of the different types of blazar spectra.

Since Blazars are strong VHE γ-ray emitters, it makes them ideal tools for indirect measurement of the EBL spectrum through their interaction with the EBL. VHE γ rays emitted from blazars collide with EBL photons and produce electron-positron pairs. This interaction causes absorption in the high energy tail of the blazar spectrum, changing the slope or the spectral index (Γ) of the VHE γ-ray part of the blazar spectrum.

Different models have been proposed to construct the spectrum of blazars from different emission mechanisms. In the next section we will give a brief description of these models and emission mechanisms.

2.2.5 Models of γ-ray emission from Blazars

There are different approaches to model the SED of blazars based on leptonic and hadronic origins. Leptonic models assume that electrons and positrons that are accelerated in the jet of the blazar boost low energy photons to high energies via IC scattering. While, in hadronic models, γ rays are the result of reactions initiated by protons that are accelerated to very high energies producing secondary particles through pions production. The resulting secondaries, such as electron-positron pairs lead to γ rays via inverse Compton or synchrotron radiation.

2.2.5.1 Leptonic model

Generally all leptonic models for blazars agree that the source of the VHE γ rays is produced by IC scattering of low energy photons by relativistic electrons found in the jet. The main difference between the various leptonic models is the source of the low energy photons. Some assume that it is from the scattering of synchrotron photons by the same electrons responsible for creating them; this is often called Synchrotron Self-Compton (SSC) (e.g. Marscher & Gear, 1985; Maraschi et al., 1992; Böttcher et al., 2009). Others suggest that the source is external to the jet and often called Synchrotron External Compton (SEC). These include photons from the accretion disk, the broad line regions, or the dusty torus (Dermer et al., 1992; Dermer & Schlickeiser, 1993; Sikora et al., 1994; Blandford & Levinson, 1995; Ghisellini & Madau, 1996; Dermer et al., 1997).

2.2.5.2 Hadronic model

Hadronic models are alternative to the leptonic ones where protons are accelerated to ultra-relativistic energies. Protons are $\sim$ 1000 times heavier than electrons, in order to accelerate the protons to ultra-relativistic energies a very strong magnetic field (tens of Gauss) must be present. Two scenarios are proposed for the VHE γ-ray production: i) shock acceleration of protons to a very high energy $\sim 10^{19}$ eV producing γ-ray via synchrotron mechanism; ii) accelerated protons interact through $p-\gamma$ or $p-p$ interactions producing pions π^0 with a lifetime $\tau = (8.4 \pm 0.5) \times 10^{-17}$s, and subsequently decay into VHE γ rays (Rachen & Mészáros, 1998; Mücke et al., 2000; Mücke & Protheroe, 2001).

2.3 INTERACTION BETWEEN γ-RAY AND EBL

2.3.1 γ-ray opacity

At the energies of the γ-ray $> 10\,$GeV, the interaction of the EBL photons with a VHE γ-ray producing electron-positron pair is the main absorption mechanism of the latter. This process is kinematically possible when:

$$\epsilon > \epsilon_{thr}(E_\gamma, \theta) \equiv \frac{2m_e^2c^4}{E(1-\cos\theta)}, \tag{2.20}$$

where ϵ and E_γ are the energies of the EBL and γ-ray, respectively, θ is the angle between the two photons. Due to the cosmic expansion, the energies of these photons are proportional to $(1+z)$ as they propagate along the line of sight. The interaction cross-section $\sigma_{\gamma\gamma}$ can be written as Breit & Wheeler (1934):

$$\sigma_{\gamma\gamma} = \frac{2\pi\alpha^2}{3m_e^2}W(\beta) \simeq 1.25\times10^{-25}W(\beta)\mathrm{cm}^2, \tag{2.21}$$

where

$$W(\beta) = (1-\beta^2)\left[2\beta(\beta^2-2)+(3-\beta^4)\ln\left(\frac{1+\beta}{1-\beta}\right)\right], \tag{2.22}$$

and

$$\beta(E_\gamma, \epsilon, \theta) \equiv \left[1-\frac{2m_e^2c^4}{E\epsilon(1-\cos\theta)}\right]^{\frac{1}{2}}. \tag{2.23}$$

This cross-section reaches its maximum ($\sigma_{\gamma\gamma}^{\max} \simeq 1.7\times10^{-25}\mathrm{cm}^2$) in a head-on collision at $\theta=\pi$ with $\beta \simeq 0.7$.

In the case of a high energy photon being absorbed in an isotropic background photon, the most effective attenuation of γ-ray photon of energy $E \sim 1\,\mathrm{TeV}$ by a soft photon is equal to a wavelength (Vassiliev, 2000),

$$\lambda_{\mathrm{IR}} = 1.33\,\mu\mathrm{m}\frac{E}{1\mathrm{TeV}}. \tag{2.24}$$

Thus, γ rays in the energy range of 100 GeV$-$10 TeV experience attenuation by low energy photons with energies from 10 eV to 0.1 eV.

By convolving the EBL photon number density (n_ϵ) with the cross-section between the EBL and γ-ray, and integrating over distance, energies of the EBL and the scattering angle, we can get the optical depth for γ rays (e.g. Dwek &

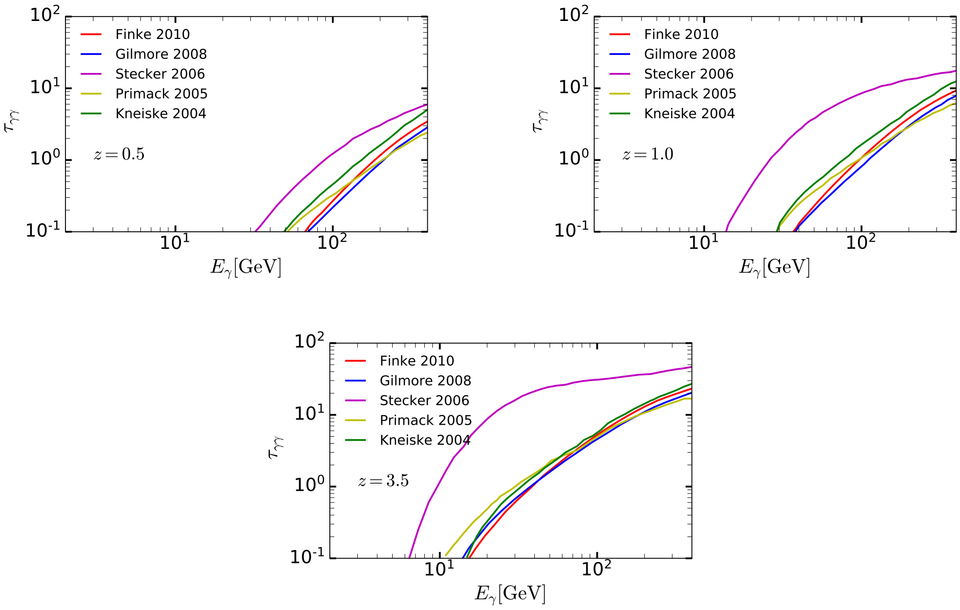

Figure 2.19: The opacity computed using different EBL models at different redshifts. The blue, red, magenta, yellow, and green lines represents the opacities using Gilmore et al. (2008); Finke et al. (2010); Stecker et al. (2006); Primack et al. (2005) and Kneiske et al. (2004) EBL models, respectively.

Krennrich, 2013):

$$\tau(E,z) = \int_0^z dz' \frac{dl}{dz'} \int_1^{-1} d\cos\theta \frac{1-\cos\theta}{2} \int_{\frac{2m_e^2c^4}{E(1-\cos\theta)}} d\epsilon(z') n_\epsilon(\epsilon(z'), z') \sigma(E(z'), \epsilon(z'), \theta), \quad (2.25)$$

where

$$\frac{dl}{dz} = \frac{c}{H_0} \frac{1}{(z+1)[(z+1)^2(\Omega_M z+1) - \Omega_\Lambda z(z+2)]^{\frac{1}{2}}}. \quad (2.26)$$

Fig. 2.19 shows the calculated opacity using different EBL models at different redshift ($z = 0.5, 1.0, 3.0$).

The intrinsic flux of the γ-ray emitted from a blazar can be related to the observed flux by (Rybicki & Lightman, 1985):

$$F_{\text{Intrinsic}} = F_{\text{Observed}} \exp[\tau(z)]. \quad (2.27)$$

The attenuation of the intrinsic γ-ray spectrum caused by the EBL taking its redshift dependency into account can be used in three ways. Knowledge of any two of the three (intrinsic γ-ray spectrum, EBL density, or redshift) can be used to determine the third or at least put a constrain on the third (see e.g., Dwek & Slavin, 1994; Biller et al., 1998; Funk et al., 1998).

2.3.2 γ-ray horizon

The probability of a VHE γ-ray encountering an EBL photon and producing an electron-positron pair depends on the energy of the VHE photon, redshift of the source and density of the EBL along the path. The γ-ray horizon is the redshift at which the optical depth becomes one ($\tau(E_\gamma, z) = 1$). In other words, it is the distance of the source at which the intrinsic γ-ray flux experience an e-fold attenuation, where the VHE photons with higher energies experience more severe attenuation. The relation between the E_γ and redshift of the horizon is called the Fazio-Stecker relationship (Fazio & Stecker, 1970). Fig. 2.20 shows the Fazio-Stecker relation for different EBL models. All models have almost the same pattern, however, the model by Stecker et al. (2006) is most opaque. While models by Kneiske et al. (2004); Gilmore et al. (2008) and Finke et al. (2010) follow a similar pattern at all redshifts, the model by Primack et al. (2005) experience more attenuation at higher redshifts. In general, the Fazio-Stecker relation is a useful tool to visualize the attenuation of the γ-rays at different redshift.

2.3.3 GeV/TeV break

The VHE blazar spectrum is a small part of the spectrum at the highest energies. The VHE spectrum can be fitted with two spectral indices for GeV (Γ_{GeV}) and TeV (Γ_{TeV}) ranges. An important feature in this spectrum is the break in the spectral index ($\Delta\Gamma_{GeV} \equiv \Gamma_{TeV} - \Gamma_{GeV}$). The Γ_{GeV} is determined by fitting the energy between $\sim 1 - 10\,\mathrm{GeV}$, which is neutral to the EBL. Under the assumption that the intrinsic spectrum of the blazar has only one spectral index ($\Delta\Gamma_{GeV} = \Gamma_{TeV} - \Gamma_{GeV} = 0 \Rightarrow \Gamma_{TeV} = \Gamma_{GeV}$), any change in the Γ_{TeV} can be directly attributed to the effect of the EBL. The position of the GeV/TeV break is expected to change with redshift. Studying the $\Delta\Gamma_{GeV}$ offers an important tool to understand the EBL and its effect on the VHE γ-ray photons, assuming that the intrinsic spectrum dose not turn up between HE and VHE regimes (see Dwek & Krennrich, 2013, for more detail).

Fig. 2.21 shows the $\Delta\Gamma_{GeV}$ as a function of redshift for different γ-ray sources. The figure shows a clear trend of increasing $|\Delta\Gamma_{GeV}|$ with redshift.

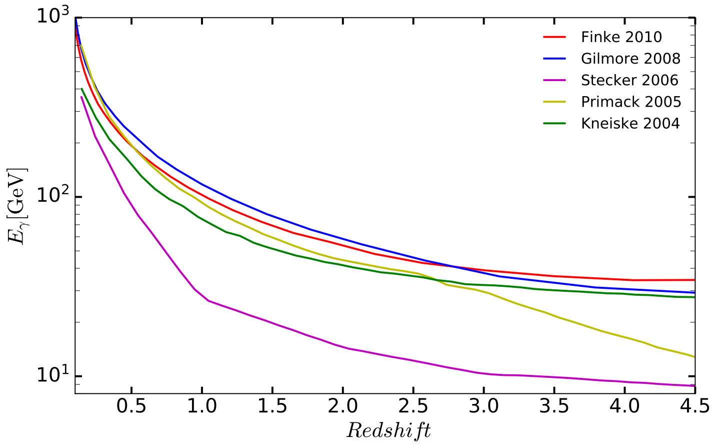

Figure 2.20: The Fazio-Stecker relationship $\tau = 1$ calculated for different EBL models. The blue, red, magenta, yellow, and green lines show the Fazio-Stecker relationship obtained using Gilmore et al. (2008); Finke et al. (2010); Stecker et al. (2006); Primack et al. (2005) and Kneiske et al. (2004) EBL models, respectively.

Almost all the sources have $\Delta\Gamma_{GeV} < 0$, which strongly implies that the break in the GeV/TeV spectrum is due to the attenuation by the EBL. In addition to the trend in the figure, there is a scatter at any redshift. The scatter could indicate intrinsic softening/hardening of the sources. An upper limit in the scatter implies that the break is only caused by the EBL (e.g., spectral hardening in 1ES 0502+675; Abdo et al., 2011a), a lower limit suggests a combination between the EBL absorption plus an intrinsic softening in the source (e.g., spectral softening in PKS 1510-089 and 3C 279). In some cases there are no spectral cut-offs up to 300 GeV (Mrk 501 Abdo et al., 2011b) and (Mrk 421 Abdo et al., 2011c) or even up to TeV ranges (Krennrich et al., 2002). Disentangling the effects EBL and the intrinsic inherited features of the source (softening/hardening of the spectra) is very challenging, therefore, multiwavelength observations are crucial to fully understand the TeV spectrum.

2.3.4 'EBL-crisis'

As mentioned earlier the EBL absorbs VHE γ rays from distant sources, the higher the distance the higher the absorption. Therefore, the spectral index at this range must steepen with distance. According to most EBL models, the VHE spectra at energies below 1 TeV and above 10 TeV are expected to be

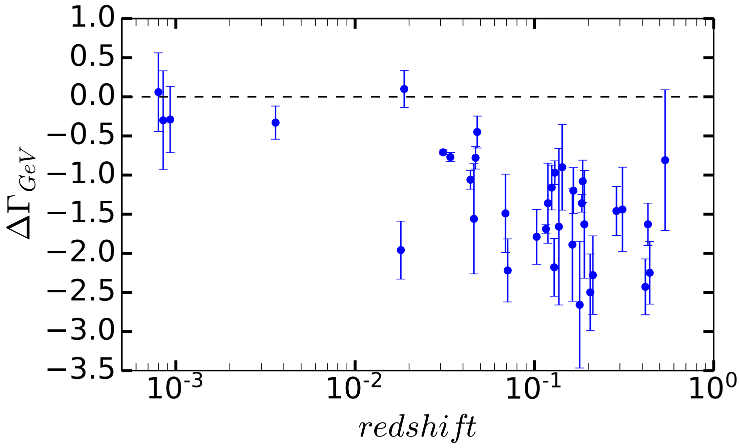

Figure 2.21: The difference between the spectral indices at TeV (Γ_{TeV}, at H.E.S.S, VERITAS and MAGIC energy range) and GeV (Γ_{GeV}, at Fermi energy range) as function of redshift for different extragalactic γ-ray sources (radio galaxies, HBLs, IBLs, LBLS, and FSRQs). The data is taken from Dwek & Krennrich (2013).

steeper relative to the energies between 1 TeV and 10 TeV given that $\tau > 1$ at the corresponding energies (Aharonian et al., 2008; Furniss et al., 2013). However, recent studies of distant TeV sources show that the γ-ray spectra corrected for EBL absorption appear unusually hard, or up-turns in some cases, at the highest energies. The VHE γ rays show that the Γ does not follow the expected pattern considering the estimated EBL density on these γ-ray paths. Fig. 2.22 shows the observed Γ with respect to redshifts together with the expected Γ only considering the EBL effect. We can clearly see the deviation between the two, creating the so-called 'EBL-crisis'. In other words, it suggests that the Universe is more transparent than it should be.

Various solutions have been suggested to solve this discrepancy. These include lower EBL density than predicted by models (see Furniss et al., 2013, and references therein), the production of secondary VHE photons due to the interaction with extragalactic ultrahigh-energy cosmic rays (UHECR) along the line of sight (see e.g., Essey & Kusenko, 2010). Some also suggested γ-ray coupling with axion-like particles (ALP), predicted by several beyond standard models of particle physics (e.g., Domínguez et al., 2011; Horns & Meyer, 2012; Harris & Chadwick, 2014; Tavecchio et al., 2015). The idea of the γ-ray mixing with ALP is that the γ-ray can potentially convert to ALP in magnetic field. The magnetic field can be close to the source or in the intergalactic

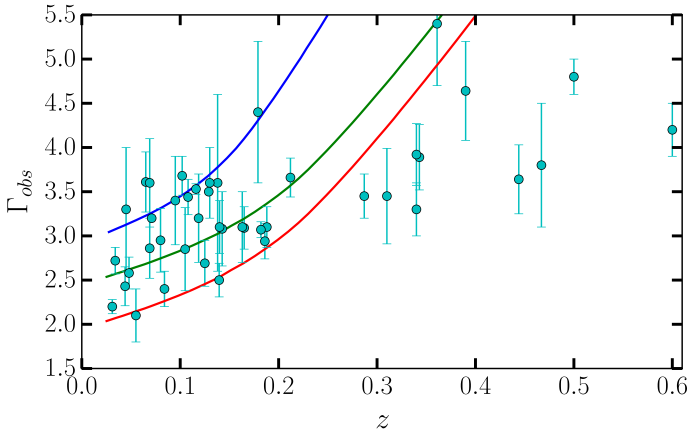

Figure 2.22: The observed spectral index Γ_{obs} at VHE γ-ray from blazars as a function of redshift (green dots) with theoretical values of Γ considering the EBL attenuation (lines). We consider three different intrinsic spectral indices ($\Gamma = 2, 2.5$, and 3 in red, green , and blue lines, respectively). There is a clear deviation between the observed and the expected values, specially at higher redshifts. Data taken from table 1 in Sinha et al. (2014).

medium. The ALP does not interact with EBL therefore helps γ-ray avoid the EBL absorption till it enters our Galaxy which the magnetic field will convert them back to γ-ray. Another proposal to fix the Universe transparency problem requires a violation of the Lorentz invariance. The possibility of Lorentz invariance violation altering the threshold of the interaction of the EBL with the VHE photons ($> 10\,\mathrm{TeV}$) and reducing the EBL opacity to the γ-ray (Tavecchio & Bonnoli, 2016).

In this thesis we will tackle the problem by studying the presence of the EBL fluctuations (Furniss et al., 2015; Kudoda & Faltenbacher, 2016; Abdalla & Böttcher, 2017) and its possible impact on the VHE γ-ray spectrum from distance sources such as blazars.

Chapter 3

EFFECTS OF SPATIAL FLUCTUATIONS IN THE EXTRAGALACTIC BACKGROUND LIGHT ON HARD GAMMA RAY SPECTRA

This work is based on the EBL model developed during my master titled *'Modelling the Inhomogeneities of the Extragalactic Background Light'* on August 2015. After fixing some bugs in the code, we reconfirm the results published in the Masters thesis. For the following publication in MNRAS we extended the work by: 1) including a comprehensive comparison with existing models, 2) calculation of the γ-ray horizon, 3) calculation of γ-ray transmissivity, 4) determination of the de-absorbed γ-ray spectra of four observed blazars, and 5) the derivation of predictions and constraints for future VHE γ-ray observations with the Cherenkov Telescope Array.

This work has been published in Monthly Notices of the Royal Astronomical Society, Kudoda & Faltenbacher Volume 467, Issue 3, 1 June 2017, Pages 2896-2902. The corresponding author of the work is Ayman Kudoda, No content was modified aside from necessary formatting.

Abstract

This study investigates the impact of the fluctuations in the extragalactic background light (EBL) on the attenuation of the hard γ-ray spectra of distant blazars. EBL fluctuations occur on the scales up to 100 Mpc and are caused by the clustering of galaxies. The EBL photons interact with high-energy γ-rays via the electron-positron pair production mechanism: $\gamma + \gamma' \rightarrow e^+ + e^-$. The attenuation of γ-rays depends on their energy and the density of the intervening EBL photon field. Using a simple model for the evolution of the mean EBL photon density, we implement an analytical description of the EBL fluctuations. We find that the amplitudes of the EBL energy density can vary by ± 1 per cent as a function of environment. The EBL fluctuations lead to mild alterations of the optical depth or equivalently the transmissivity for γ-rays from distant blazars. Our model predicts maximum changes of ± 10 per cent in the γ-ray transmissivity. However, this translates into marginal differences in the power-law slopes of currently observed γ-ray spectra. The slopes of deabsorbed γ-ray spectra differ by not more than ± 1 per cent if EBL fluctuations are included.

3.1 INTRODUCTION

The extragalactic background light (EBL) is the light between 0.1 and 1000 μm accumulated by the global stellar population throughout cosmic time. It contributes about 1 per cent to the sky brightness from the ultraviolet (UV) to infrared (IR) wavelength range (Bernstein, 2000) with two peaks dominating the spectrum: a first peak between 0.1 and 10 μm, which is due to direct stellar emission; and a second peak between 10 and 1000 μm caused by the dust contribution (Hauser & Dwek, 2001; Dwek & Krennrich, 2013).

The EBL contains a wealth of information related to the evolution and the structure of the Universe and its astrophysical components. Measuring the EBL directly, however, is difficult for various reasons. For example, it is challenging to separate the EBL from the zodiacal light of our Solar system and from the foreground light of our Galaxy (Costamante, 2013). For direct source counts, the foreground light causes a systematic bias against the detection of individual faint or low surface brightness galaxies and intergalactic stars. Despite all difficulties, the measurement of the EBL can provide useful integral constraints on star formation models and the baryonic matter content of the Universe (Bernstein, 2000).

Several observational studies have been carried out to investigate fluctuations in the EBL. Fluctuations in the EBL are expected due to the density fluctuations of the underlying galaxy population. For instance, Shectman (1973) and Shectman (1974) study the anisotropy in the optical regime, and Kashlinsky et al. (1996b) investigate the clustering in the near-IR region using Cosmic Background Explorer (COBE) and Diffuse Infrared Background Experiment (DIRBE) maps. Although one cannot determine the EBL density by knowing only the fluctuations in the EBL, the fluctuation measurements can be used to derive limits on the EBL density at certain regions of the spectrum (Pénin et al., 2012; Dwek & Krennrich, 2013).

Indirect measurements of the EBL can be obtained from observations of the attenuation of γ-ray spectra of distant very high energy (VHE) sources such as quasars. As γ-rays travel through the Universe, they interact with EBL photons producing electron-positron pairs ($\gamma + \gamma' \rightarrow e^- + e^+$). This process leaves a finger print on the spectral index of the quasars in the VHE regime (Stecker et al., 1992; Yuan et al., 2012; Stecker et al., 2016). Electron-positron pair production is the main channel for γ-ray absorption at VHE, and the only absorption process we consider here for γ-ray photons travelling cosmic distances. It can take place only if the total energy of the two interacting photons is higher than the rest mass of the electron-positron pair. Based on the cross-section of the photon-photon interaction and a model of the EBL density, the optical depth (τ) can be computed for VHE γ-ray sources at redshift z.

It is well known that galaxies, the sources of the EBL, are clustered. Thus, the EBL density is expected to be subject to fluctuations too. However, since the EBL is accumulated throughout the history of the Universe, the fluctuations may be small as they are largely overpowered by the homogeneous contribution of EBL sources at larger distances. To what extent these small fluctuations can impact the attenuation of VHE quasar spectra is currently still under debate. Recently, Furniss et al. (2015) found a correlation between VHE-emitting sources and cosmic voids along the line of sight. However, they estimate that the attenuation decreases less than 10 per cent for a γ-ray source with opacity $\tau \sim 5$ if the line of sight goes entirely through underdense regions. The model presented here provides a quantitative analysis of EBL fluctuations, which allows us to predict the alteration of the attenuation of VHE γ-rays from distant quasars.

The structure of this paper is set as follows. In Section 3.2, we introduce the analytical EBL model, which is based on the work of Razzaque et al. (2009) and Finke et al. (2010) with an extension allowing for the implementation of EBL fluctuations. The calculations for the absorption of γ-rays due to the interaction with EBL photons are reviewed in Section 3.3. Based on deabsorbed quasar spectra, the impact of the EBL fluctuations is discussed in Section 3.4. Finally, a brief conclusion is given in Section 3.5.

3.2 MODELLING THE EBL

The EBL model employed here is similar to the approach presented in Razzaque et al. (2009), hereafter referred to as RDF09, which is a forward evolution model. RDF09 take into account only the contribution of the stellar component, which is inferred from the stellar thermal surface emission of main-sequence stars modelled as blackbody radiation. Contributions from off-main-sequence stars are ignored. Since the total contribution of quasars and active galactic nuclei (AGNs) to the optical and the IR regime of the EBL spectrum is $10 - 20$ per cent at maximum (Hauser & Dwek, 2001), the contributions of AGNs are ignored by RDF09 and in our model as well.

The IR re-emission of stellar light absorbed by dust is modelled following Finke et al. (2010), hereafter referred to as FRD10. As an extension, we

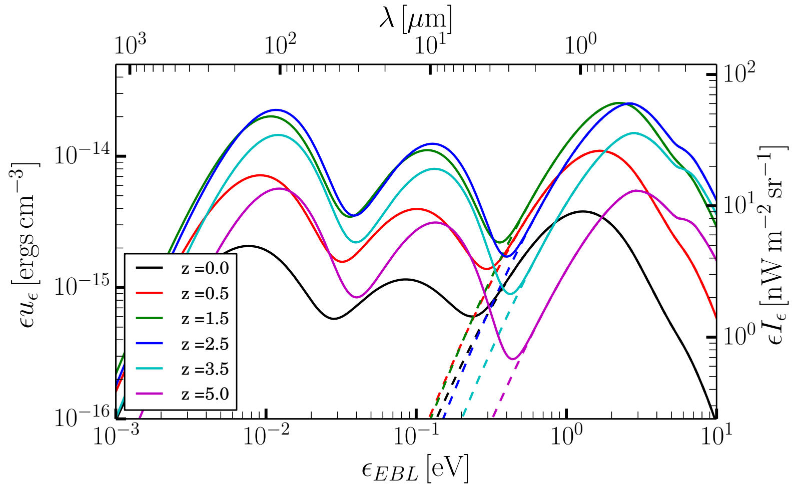

Figure 3.1: Model of the EBL energy density including stellar and dust components at different redshifts (solid lines). The model of the stellar component (dashed lines) is a reproduction of model B in Razzaque et al. (2009). The emission of the dust component, responsible for the two peaks at $\lambda \gtrsim 8\mu$m, is computed following Finke et al. (2010).

implement a statistical description of fluctuations of the EBL photon densities due to the clustering of galaxies. For that purpose, we utilize the small-scale (< 100 Mpc) variance of the cosmic star formation rate.

3.2.1 Stellar component

This section gives a brief review of the RDF09 model; for more details, we refer the interested reader to the original article by RDF09. The RDF09 model estimates the EBL at $z = 0$ by integrating the contributions from stars of all masses formed throughout the history of the Universe. The emission of stars is modelled as blackbody radiation at a given temperature emitted from the spherical surface of the star. Temperature and radius are expressed as fitting functions with the stellar mass as free variable. The mass distribution is modelled by a given initial mass function (IMF) plus a stellar lifetime criterion, which eliminates the contribution of stars that have left the main sequence. A further element for the integration of the EBL is the global star formation rate (SFR).

With these ingredients, the spectral energy distribution (SED) of the stellar component of the EBL measured at present ($z = 0$) can be expressed by

$$\begin{aligned} \frac{dN(\epsilon, z=0)}{d\epsilon dV} =& \mathcal{N} \int_{z=0}^{\infty} dz'' \left| \frac{dt}{dz''} \right| \psi(z'') \int_{M_{\min}}^{M_{\max}} dM \xi(M) \\ & \times \int_{\max\{z=0, z_d(M,z')\}}^{z''} dz' \left| \frac{dt}{dz'} \right| \\ & f_{\rm esc}(\epsilon') \frac{dN(\epsilon', M)}{d\epsilon' dt} (1+z'), \end{aligned} \qquad (3.1)$$

where $\mathcal{N}$ is the normalization factor for the IMF $\xi(M)$, M_{min} and M_{max} are 0.1 $M_\odot$ and 120 $M_\odot$, respectively, $\psi(z)$ is the SFR at redshift z, $\epsilon' = \epsilon(1+z')$ is the redshifted energy of the EBL photons, z_d is the redshift when the star evolves away from the main sequence and $\frac{dN(\epsilon',M)}{d\epsilon' dt}$ is the total number of emitted photons per unit time per energy interval from a star with mass M that uniquely determines the radius R and temperature T. The averaged photon escape fraction from a galaxy, $f_{\rm esc}(\epsilon')$, is given by an empirical fitting function adapted from Driver et al. (2008). The fraction of photons generated in stars, which does not escape, is $1 - f_{\rm esc}(\epsilon')$. In the RDF09 model, these photons are considered to be lost. In the FRD10 model, discussed in the next section, these photons are re-emitted in the IR band.

RDF09 considers different combinations between the SFR and IMF. We use their best-fitting EBL model (model B with a single power law for the mass-luminosity and mass-temperature relations) to calculate the SED. Model B is based on the SFR described in Cole et al. (2001)[10] and the modified 'Salpeter A' IMF, $dN/dM \propto M^{-\kappa}$ with $\kappa = 1.5$ for $M < 0.5$ $M_\odot$ and $\kappa = 2.35$ for $M > 0.5$ $M_\odot$.

In the following, we will make use of the comoving EBL energy density, ϵu_ϵ, at a given redshift $z = z_1$, which can be derived from the SED (equation 3.1) as follows:

$$\epsilon u_\epsilon = (1+z_1)^4 \epsilon^2 \frac{dN(\epsilon, z=z_1)}{d\epsilon dV} \ . \qquad (3.2)$$

Note, for the determination of the comoving EBL energy density at $z = z_1$, all occurrences of '$z = 0$' in equation (3.1) have to be replaced by '$z = z_1$'. Fig. 3.1 shows the evolution of ϵu_ϵ with redshift. The dashed lines represent the stellar component and the solid lines show the full EBL with dust re-emission, which is discussed in the following section.

[10] $\psi(z) = [h(a+bz)]/[1+(z/c)^d]$ with fitting parameters from Hopkins & Beacom (2006): $\{a, b, c, d\}$=$\{0.0166, 0.1848, 1.9474, 2.6316\}$

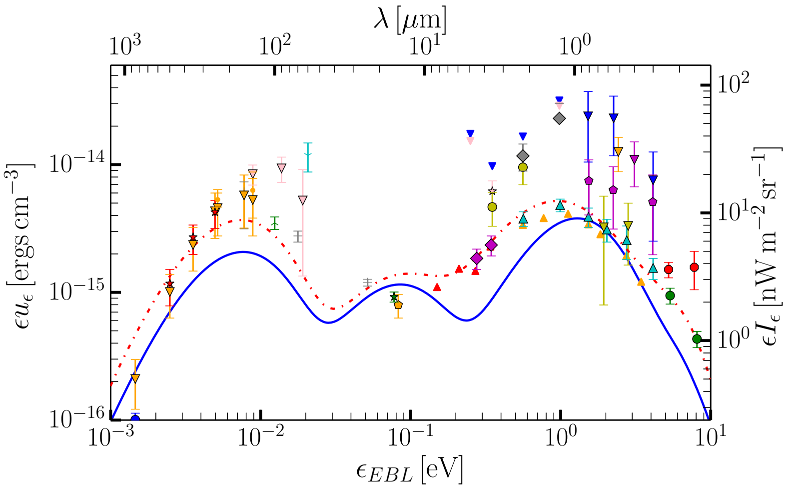

Figure 3.2: Comparison of EBL energy density model spectra with observational data. The solid black line represent our EBL energy density at $z = 0$ and the dashed red line is model by Finke et al. (2010). The symbols represent EBL measurements: green circle - Xu et al. (2005); red octagon - Gardner et al. (2000); blue triangle down - Bernstein (2007); cyan triangle up - Totani et al. (2001); magenta triangle down - Mattila (1990); yellow triangle down - Matsuoka et al. (2011); orange triangle down - Dube et al. (1979); grey triangle down - Levenson et al. (2007); pink triangle up - Keenan et al. (2010); magenta diamond - Ashby et al. (2013); blue square - Arendt & Dwek (2003); orange pentagon - Hopwood et al. (2010); green star - Teplitz et al. (2011); grey plus - Béthermin et al. (2010); cyan triangle down - Finkbeiner et al. (2000); pink triangle down - Matsuura et al. (2011); green triangle up - Berta et al. (2011); orange triangle down - Fixsen et al. (1998); grey triangle down - Pénin et al. (2012); red star - Béthermin et al. (2012); orange dot - Odegard et al. (2007); blue circle - Zemcov et al. (2010).

Table 3.1: Dust parameters

Component	n	f_n	T_n(K)
Warm large grains	1	0.60	40
Hot small grains	2	0.05	70
PAHs	3	0.35	450

3.2.2 Dust component

In order to compute the dust re-emission spectrum, we start with the total number of photons emitted per unit energy and time by a star of radius R given by (as discussed in RDF09)

$$\frac{dN}{d\epsilon dt} = \frac{R^2}{\pi c^2 \hbar^3} \frac{\epsilon^2}{\exp(\epsilon/kT) - 1} \; . \tag{3.3}$$

RDF09 present fitting formulas, which allow us to compute all relevant stellar quantities, such as radius R, temperature T and luminosity L as functions of stellar mass M. The averaged fraction of photons absorbed by the dust is given by $1 - f_{\rm esc}$ (cf. equation 3.1). The absorbed photons are re-radiated in the IR. Assuming quasi-static equilibrium, the total energy absorbed and re-emitted by the dust per unit time interval, $dE_{\rm dust}(M)/dt$, for a star of mass M is given by

$$\frac{dE_{\rm dust}(M)}{dt} = \int_0^\infty (1 - f_{\rm esc}) \; \epsilon \; \frac{dN(\epsilon, M)}{d\epsilon dt} \; d\epsilon \; . \tag{3.4}$$

To compute the dust IR emission spectrum, the interstellar medium is modelled by three major dust components (cf. Desert et al., 1990): (1) large dust grains; (2) small dust gains; and (3) polycyclic aromatic hydrocarbons (PAHs). The superposition of the three associated blackbodies results in the dust IR emission spectrum. The properties of the three blackbodies are indicated in Table 3.1, where n is an arbitrary index, $f_{\rm n}$ is the fraction of absorbed emissivity re-radiated by a particular blackbody at temperature $T_{\rm n}$. Consequently, the total absorbed emissivity is equal to

$$\frac{dE_{\rm dust}(M)}{dt} = \sum_{n=1}^{3} \int_0^\infty \frac{\Omega_n(M) \epsilon^3}{\exp(\epsilon/kT_n)} d\epsilon \; , \tag{3.5}$$

where the scaling factors $\Omega_n(M)$ can be determined as follows:

$$\Omega_n(M) = f_n \frac{dE_{\rm dust}(M)/dt}{\int_0^\infty \frac{\epsilon^3}{\exp(\epsilon/kT_n)} d\epsilon} \; . \tag{3.6}$$

The dust re-emission term (equation 3.5) is plugged into equation (3.1), resulting in the following integral expression for the comoving EBL energy density measured at redshift $z = z_1$:

$$
\begin{aligned}
\frac{dN(\epsilon, z=z_1)}{d\epsilon dV} =& \mathcal{N} \int_{z=z_1}^{\infty} dz'' \left|\frac{dt}{dz''}\right| \psi(z'') \int_{M_{\min}}^{M_{\max}} dM \xi(M) \\
& \times \int_{\max\{z=z_1, z_d(M,z')\}}^{z''} dz' \left|\frac{dt}{dz'}\right| (1+z') \\
& \left[\sum_{n=1}^{3} \Omega_n(M) \epsilon'^2 \exp(\epsilon'/kT_n) + f_{esc}(\epsilon') \frac{dN(\epsilon', M)}{d\epsilon' dt}\right]
\end{aligned} \tag{3.7}
$$

The solid lines in Fig. 3.1 show the comoving EBL energy densities for a set of redshifts as indicated. Fig. 3.2 compares the EBL spectrum for the present epoch (blue solid line) with observations (symbols) and the FRD10 model (red dashed line). The FRD10 model comprises a more sophisticated stellar evolution model (based on fits to stellar evolution tracks presented in Eggleton et al. 1989), which leads to a slightly higher integrated luminosity of individual stars. Consequently, our model provides a lower limit to the EBL measurements as it employs a slightly underluminous stellar population. This has no effect on our results as we are interested in the *relative differences* of the γ-ray attenuation caused by the fluctuations of the EBL photon densities.

3.2.3 Implementing spatial EBL fluctuations

Galaxies show spatial clustering, which causes spatial fluctuations in the intensity of the EBL. In order to develop a mathematical framework for computing the EBL fluctuations, we start by determining the spatial fluctuations in the SFR. The rationale behind this approach is that (1) the calculation of the EBL in the RDF09 model is based on the integration of the SFR over cosmic time; and (2) spatial differences in the SFR cause spatial differences in the galaxy density. Thus, if a region shows a lower than average SFR, then the galaxy density is lower and thus also the EBL intensity is lower compared to the cosmic mean. For regions of higher than average SFR, the opposite holds true.

For a rough (but sufficient) estimate of the spatial fluctuations in the SFR, we employ a semi-analytical galaxy catalogue based on the Millennium Simulation Run 7 (MR7, Lemson & Virgo Consortium, 2006; Guo et al., 2013), which reproduces the observed galaxy populations reasonably well. We extract the distribution of the SFR within shells of 10 Mpc h^{-1} thickness centred on 1000 seed points which span a regular grid filling the volume of the simulation

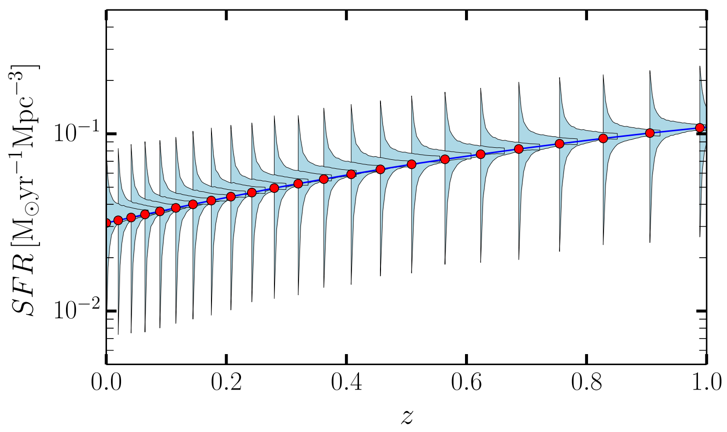

Figure 3.3: The SFR history derived from the semi-analytical galaxy catalogue by Guo et al. (2013) as function of redshift. The red points represent the mean star formation rate in the entire simulation box at the redshifts of the snapshots. The fluctuations are indicated as vertical, "trumpet-shaped", shaded regions delineated by the lower 5 and upper 95 percentiles of the distribution of SFRs in shells of various radii (redshifts) about 1000 centres located on a regular grid within the simulation box.

box. The 5th and 95th percentiles of the distribution of SFRs in each shell give a measure of the scatter in the SFR as a function of the distance to the location of the observer.

The determination of the scatter is repeated for all snapshots, which comprise galaxies ($z \lesssim 10$). The comoving shell radii, R_i, can be converted into a redshift separation, $z_\mathrm{i} = z - z_\mathrm{snap}$, by using the distance-redshift relation, $cz_\mathrm{i} = H(z_\mathrm{snap})\ a(z_\mathrm{snap})\ R_\mathrm{i}$, where z_snap is the redshift of the snapshot, R_i is the comoving distance, and $H(z)$ and $a(z)$ are the Hubble parameter and the scalefactor at that redshift. Fig. 3.3 shows the mean SFR in the simulation box for the snapshots between $z = 0$ and $z = 1$ (red circles) and the scatter as a function of z (blue 'trumpets'). The trumpet shape is easily explained: Locally within $R_\mathrm{i} \lesssim 100$ Mpc/h ($z_\mathrm{i} \lesssim 0.03$) the scatter in the SFR is large, but as the radii of the shells increase, the scatter of the SFR reduces, which is simply a volume effect. To obtain a time-independent approximation for the spatial scatter of the SFR, we fit polynomials to the trumpet shapes of all redshifts simultaneously: one polynomial for the upper 95 percentile margin and another polynomial for the lower 5 percentile margin.

Adding the upper or lower margins to the smooth SFR at a given redshift

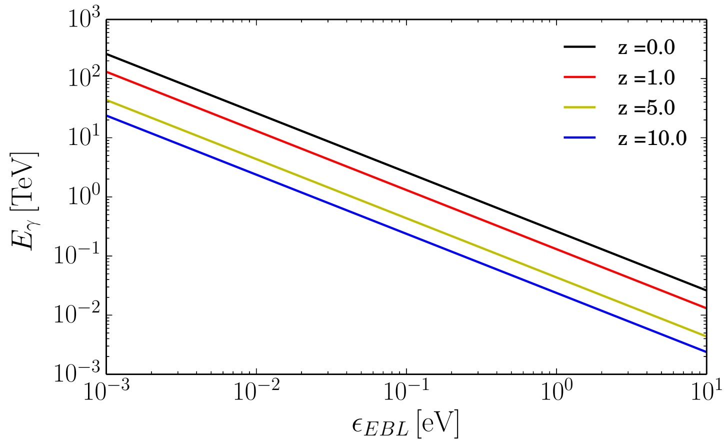

Figure 3.4: Limits for $\gamma + \gamma' \rightarrow e^- e^+$ pair production for various redshifts. The lines represent the $s_0 = 1$ condition (Gould & Schréder, 1967) as a function of γ-ray, E_γ and EBL photon energy, ϵ_{EBL}. For each given redshift pair production is possible in the area above the line.

allows us to model the EBL intensity in overdense and underdense regions, respectively. The continuous use of the upper margin of the SFR for the computation of the local EBL intensity along the path of a γ-ray models a γ-ray traversing the Universe within a cylinder of enhanced galaxy (SFR) densities. In contrast, a continuous use of the lower margin of the SFR mimics a γ-ray within a cylinder of reduced galaxy (SFR) densities. These are the two extreme cases, which we employ to determine the upper and lower limits of γ-ray attenuation.

3.3 ABSORPTION OF γ-RAY SPECTRA

The total cross-section, σ, for electron pair production, $\gamma + \gamma \rightarrow e^+ + e^-$ (cf. Gould & Schréder, 1967), is

$$\sigma = \frac{1}{2}\pi r_0^2 (1 - \beta^4) \left[(3 - \beta^4) \ln \frac{1 + \beta}{1 - \beta} - 2\beta(2 - \beta^2) \right], \qquad (3.8)$$

where $\beta = \sqrt{1 - \frac{1}{s}}$ is the electron and positron velocity, r_0 is electron radius and $s = \frac{s_0}{2}(1 - \cos\theta)$ is square energy of the centre of mass, where $s_0 = \left(\frac{\epsilon E}{m^2 c^4}\right)$. According to equation (3.8), pair production can occur only if $s > 1$. Fig. 3.4 shows the $s = 1$ lines as a function of the γ-ray and EBL photon energies at different redshifts. Pair production is possible in the regions above the

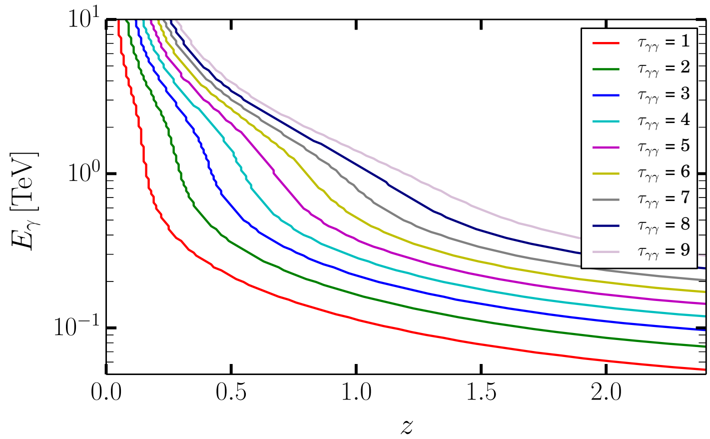

Figure 3.5: $E - z$ contours for values of $\tau_{\gamma\gamma} = 1 - 9$ based on the EBL energy density predicted by our model. Each line is labeled by the corresponding τ. The bottom line for $\tau_{\gamma\gamma} = 1$ defines the γ-ray horizon which separates γ-ray transparent (below) and γ-ray opaque (above) areas.

lines. At $z = 0$, for instance, γ-rays above ~ 261 TeV can produce e^-, e^+ pairs through interactions with EBL photons of the entire range shown ($10^{-3} \lesssim \epsilon_{EBL} \lesssim 10$ eV). In contrast, the EBL is transparent to the γ-ray photons below ~ 0.02 TeV.

Based on the total cross-section, equation (3.8), we calculate the optical depth, $\tau_{\gamma\gamma}$, as a function of γ-ray energy, E, and redshift, z (cf. Razzaque et al., 2009), as follows:

$$\tau_{\gamma\gamma}(E_\gamma, z) = c\pi r_0^2 \left(\frac{m_e^2 c^4}{E_\gamma}\right)^2 \int_0^z \frac{dz_1}{(1+z_1)^2} \left|\frac{dt}{dz_1}\right| \times \int_{m_e^2 c^4/E_\gamma(1+z_1)}^{\infty} d\epsilon_1 \frac{u_{\epsilon_1}}{\epsilon_1^3} \overline{\varphi}[s_0(\epsilon_1)] \ , \tag{3.9}$$

where $s = E_\gamma(1+z_1)\epsilon_1/2m_e^2 c^4$, $\varphi[s_0(\epsilon_1)] = \int_1^{s_0(\epsilon)} s\overline{\sigma}(s)ds$ and$\overline{\sigma}(s) = \frac{2\sigma(s)}{\pi r_0^2}$, $s_0 = E_\gamma(1+z_1)/m_e^2 c^4$.

As expected, $\tau_{\gamma\gamma}(E_\gamma, z)$ increases with z, i.e. the γ-ray emission from a source at a larger distance will be attenuated more strongly. For nearby sources, τ is usually < 1, in which case the Universe becomes optically thin for γ-rays. Still, at very high γ-ray energies, the optical depth can be larger than 1, leading to an optically thick Universe. For a given E_γ, the redshift at which $\tau_{\gamma\gamma} = 1$ defines the γ-ray horizon (Fazio & Stecker, 1970). Fig. 3.5

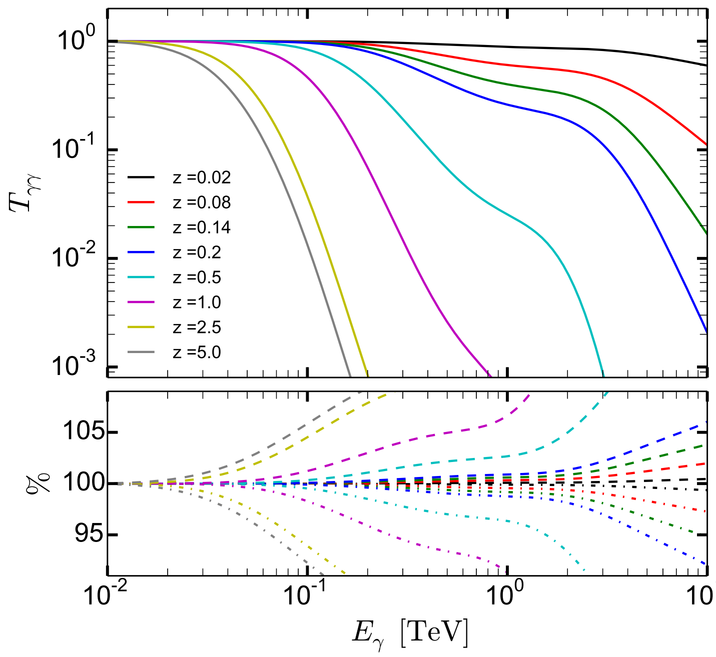

Figure 3.6: *Upper panel*: *gamma*-ray transmissivity as a function of γ-ray energy at different redshifts. *Lower panel*: The relative difference between the mean γ-ray transmissivity and the upper and lower limits due to EBL fluctuations as a function of observed γ-ray energy. The lines above and below the horizontal 100 per cent demarcation correspond to the lower and upper limits of the EBL fluctuations, respectively.

shows the $E - z$ contours for values of $\tau_{\gamma\gamma} = 1 - 9$ based on the EBL energy density predicted by our model.

The transmissivity, $T_{\gamma\gamma}$, is defined as the probability to observe γ-rays with energy, E_γ, from a source at redshift z. It can be calculated by

$$T_{\gamma\gamma}(E_\gamma, z) = e^{-\tau_{\gamma\gamma}(E_\gamma, z)} \ . \tag{3.10}$$

The upper panel in Fig. 3.6 shows the transmissivity as predicted by our EBL model for different redshifts. The graphs in the lower panel are discussed in the next section.

3.4 RESULTS

We use the EBL spectrum discussed in Section 3.2 as our fiducial model for the mean EBL density. Upper and lower EBL density limits are implemented as discussed in Section 3.2.3 corresponding to γ-rays travelling through overdense and underdense regions along the entire path from the source to the observer. We first discuss the impact of the spatial fluctuations of the SFR on the EBL spectrum. The results are used to determine the mean, the upper and the lower limits of the γ-ray transmissivity, which, in turn, is employed to deabsorb VHE spectra of observed blazars. At the end of this section, we present a speculation on how the spectra of very high redshift blazars would be affected by the fluctuations in the EBL.

3.4.1 Fluctuations in the SFR and EBL

Equation (3.7) is the core of the model presented here. Basically, it integrates over the cosmic SFR to obtain the comoving EBL energy density at $z = z_1$. The SFR is subject to spatial fluctuations, which we include in a statistical manner, as illustrated in Fig. 3.3. The integration of the upper and lower limits of the SFR allows us to compute the EBL intensity in overdense and underdense regions, respectively. We find that the EBL intensity changes by ± 1 per cent over the entire frequency range, depending on whether the observer is located in an overdense or an underdense region. This relatively small change is expected since the majority of EBL photons arrive from shells with large radii, which reflect the average luminosity of the Universe. However, cumulative effects for γ-rays traversing the Universe along predominantly overdense or underdense paths may still alter the γ-ray attenuation. The following section investigates whether cumulative effects are significant

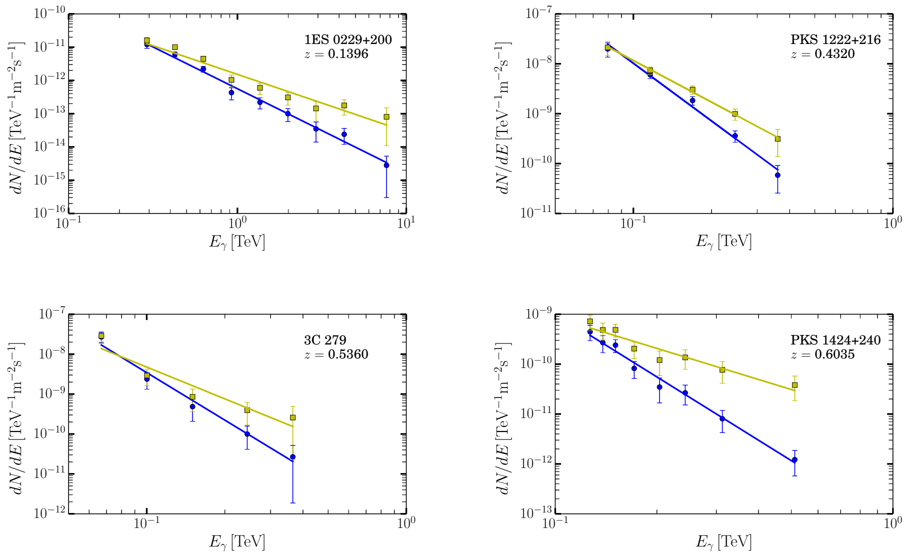

Figure 3.7: Observed γ-ray fluxes of blazars indicated as blue circles and deabsorbed counterparts shown as yellow squares. The blue and yellow lines are power law fits ($dN/dE \propto E^{-\Gamma}$) to the observed and the deabsorbed data points, respectively. The Γs as obtained from the power law fits are given in Table 3.2.

3.4.2 Fluctuations in the γ-rays transmissivity

The lower panel of Fig. 3.6 displays the relative difference between the upper and the lower limits of the transmissivities obtained by plugging in the lower and upper limits of the EBL density in equation (3.9). Choosing the upper (lower) SFR limit for every integration step mimics the cumulative effect of γ-rays travelling through overdense (underdense) regions along the entire path from the source to the observer. It turns out that spatial fluctuations of the EBL intensity have a negligible impact on the transmissivity for γ-ray sources with $z < 0.5$ and $E_\gamma < 1\,\mathrm{TeV}$ ($\lesssim 2$ per cent). But for larger energies and redshifts, we find increasing deviations from the mean transmissivity. For instance, sources at $z > 0.5$ with γ-ray energies $E_\gamma > 0.1\,\mathrm{TeV}$ show a change of up to ± 10 per cent in the transmissivity.

Table 3.2: Logarithmic slope of deabsorbed blazar spectra

Blazar	Redshift	Observed Γ	Deabsorbed Γ
PKS 1424 + 240[‡]	0.6035	4.26	$2.07^{2.05}_{2.08}$
PKS 1222 + 216[†]	0.432	3.84	$2.77^{2.75}_{2.78}$
lES 0229 + 200[⋆]	0.1396	2.51	$1.72^{1.71}_{1.73}$
3C 279[•]	0.536	3.94	$2.66^{2.64}_{2.67}$

[‡]Archambault et al. (2014), [†]Kushwaha et al. (2014), [⋆]Aharonian et al. (2007) and [•]Albert et al. (2008) *Note*: The superscripts and subscripts in column 4 represent the upper and lower Γ based on the upper and lower transmissivity limits of the EBL fluctuation model.

3.4.3 Impact on deabsorption of γ-ray spectra

Knowing the transmissivity allows us to determine the deabsorbed γ-ray flux of the observed VHE blazar spectra as follows:

$$\left[\frac{dN}{dE}\right]_{\text{deabsorbed}} = \exp[\tau(z, E)] \left[\frac{dN}{dE}\right]_{\text{observed}} \tag{3.11}$$

Deabsorbed spectra provide valuable insights into the intrinsic blazar physics. Fig. 3.7 shows the deabsorbed spectra for a sample of four different VHE sources at different redshifts. The lines present power-law fits to the observed (blue) and deabsorbed (green) data points. Table 3.2 gives the exponents of the deabsorbed spectra, which are slightly larger (spectra are steeper) than reported in the literature. This is a result of the slightly underluminous stellar population used in our model.

Employing the upper and lower limits of the transmissivity due to fluctuations in the EBL causes marginal differences in the deabsorbed data points. The ranges of the exponents of the respective power-law fits are indicated in the fourth column of Table 3.2. The exponents differ by ~ 1 per cent. This leads to the conclusion that fluctuations in the EBL intensity have a marginal impact on the slope of the spectra for the redshift range covered by the blazar sample considered here.

3.4.4 Impact on high redshift γ-ray spectra

As a final speculative outlook, we calculate the maximum impact of the EBL fluctuations on γ-ray sources at larger redshifts than observed to date. As a starting point, we use the deabsorbed spectrum of lES0229 + 200 (cf. Fig.

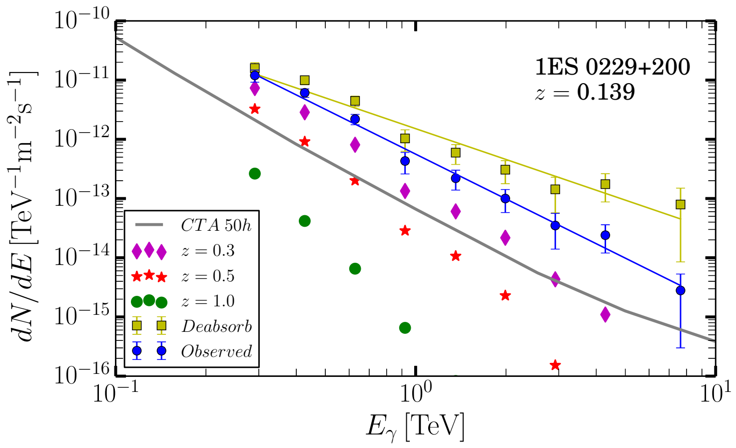

Figure 3.8: The blue circles and yellow squares represent observed and the deabsorbed γ-ray fluxes for PKS $1222 + 200$. The lines are power law fits to the data points. The magenta, green and red dots would be the observed fluxes if the source were located at $z = 0.3$, 0.5, and 1.0, respectively. The grey solid line is the predicted CTA sensitivity for 50 hour observation. It is interesting to note that the slope of the quasars and the sensitivity limit of CTA are very similar.

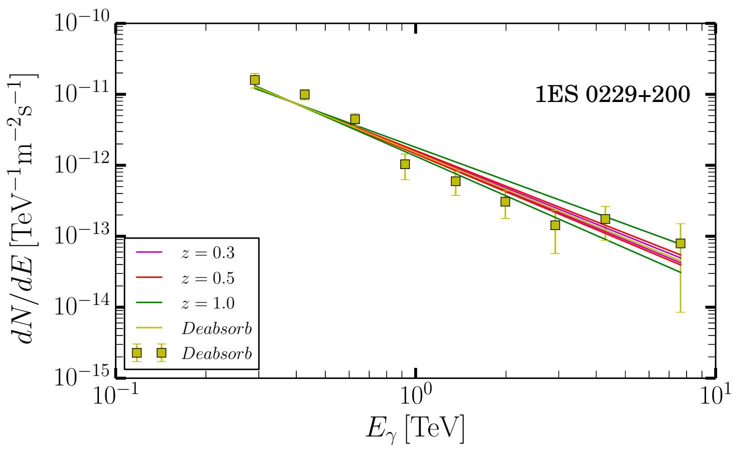

Figure 3.9: The yellow squares show the deabsorbed γ-ray fluxes with measurement errors for PKS $1222+200$. The magenta, green and red lines indicate the upper and lower limits due to EBL fluctuations if the source is shifted to $z = 0.3$, 0.5, and 1.0 and subsequently deabsorbed assuming the γ-rays travel through over and under dense regions along the entire path from the source to the observer.

Table 3.3: Deabsorbed slopes of blazar shifted to different z

Blazar	Redshift	Observed Γ	Deabsorbed Γ
1ES 0229+200	0.3	3.70	$1.72^{1.69}_{1.74}$
	0.5	5.56	$1.72^{1.66}_{1.77}$
	1.0	11.63	$1.72^{1.55}_{1.85}$

3.7), which is a nearby high-γ-ray energy source. We then shift this spectrum to various redshifts by 'absorbing' it, i.e. multiplying it by $\exp[-\tau(z, E)_{\mathrm{mean}}]$. This is the reverse process to deabsorbing it.

Fig. 3.8 shows the absorbed data points. Purple diamonds, red stars and green circles correspond to redshifts $z = 0.3$, 0.5, and 1.0, respectively. For comparison, we copy the observed and the deabsorbed data as already displayed in Fig. 3.7. The grey line represents the sensitivity limit for $50\,h$ observations with the Cherenkov Telescope Array (CTA). The third column of Table 3.3 gives the slopes of the absorbed (observable) data for the three redshifts.

For γ-ray sources at increasing redshifts, the high-energy tails of the spectra drop below the detection limit at decreasing energies. The spectrum of the source shifted to $z = 0.5$, for instance, drops below the CTA sensitivity for γ-ray energies above 700 GeV. It is interesting to note that the slope of the spectrum is very similar to the slope of the sensitivity limit. Thus, a slight change in the slope of the observed spectrum, possibly due to fluctuations in the EBL, can have an effect on the detectability of the γ-ray source.

The fourth column of Table 3.3 gives the slopes of the deabsorbed γ-ray spectra. Upper and lower limits are based on deabsorption for γ-rays propagating through overdense or underdense regions along the entire path from the source to the observer. Concretely, the absorbed (i.e. observable) data points are deabsorbed by multiplying with $\exp[\tau(z, E)_{\mathrm{mean}}]$, $\exp[\tau(z, E)_{\mathrm{upper}}]$ and $\exp[\tau(z, E)_{\mathrm{lower}}]]$. The deabsorbed data are fit to be power laws. Fig. 3.9 compares the ranges of the respective slopes to the intrinsic errors of the observation. The figure indicates that the change in the slope even for the most extreme cases is comparable to the intrinsic error of current measurements.

3.5 CONCLUSION

Understanding the evolution of the EBL is crucial for the interpretation of γ-ray observations (and also for setting constraints on galaxy evolution models). We employ a simple model introduced by RDF09 and include dust re-emission following FRD10 to describe the evolution of the EBL spectrum. The use of oversimplified stellar evolution models results in spectra that are at the lower bound of current EBL measurements and theoretical predictions. This does not affect our conclusions since we are interested in *relative differences* between EBL in high and low luminosity density environments.

As an extension of current EBL models, we include EBL intensity fluctuations, which are assumed to be the result of spatial fluctuations in the SFR. The statistical description of the spatial fluctuations of the SFR is derived from the semi-analytical galaxy catalogue based on MR7. The modified EBL model allows us to investigate the impact of EBL fluctuations on the attenuation of VHE γ-ray spectra due to $\gamma + \gamma' \rightarrow e^+ + e^-$ pair production. As mentioned above, contributions of AGNs are ignored. However, despite the relatively small contribution of AGNs to the overall EBL spectrum, the strong clustering of AGNs at high redshifts (e.g. Porciani et al., 2004; Coil et al., 2007; Ross et al., 2009) may slightly enhance EBL fluctuations at early times. Testing this conjecture requires the implementation of an AGN model, which is beyond the scope of this work.

The overall outcome of our study is that, in general, the impact of EBL fluctuations on the slope of VHE γ-ray spectra is negligible. A deabsorption procedure that includes this effect deviates by less than 1 per cent from deabsorption based on mean EBL intensities.

Chapter 4

DETAILED MODELLING OF THE EBL ALONG VHE γ-RAY PATHS

This work has been published in Monthly Notices of the Royal Astronomical Society, Kudoda & Faltenbacher Volume 481, Issue 1, 21 November 2018, Pages 405-413. The corresponding author of the work is Ayman Kudoda, No content was modified aside from necessary formatting.

Abstract

Interactions between the extragalactic background light (EBL) and very high-energy (VHE; $E > 10$ GeV) γ-rays from cosmological sources alter their γ-ray spectrum. The stronger absorption of harder γ-rays causes a steepening of the observed γ-ray spectrum at the high-energy tail, which can be expressed by an increase of the power index. The effect provides a link between high-energy astrophysics and the evolution of galaxies. In this work we develop a new hybrid EBL model by augmenting our previous analytic model with information from semi-analytic galaxy catalogues. The model allows us to study the γ-ray opacities of individual γ-ray paths through the (simulated) universe and evaluate the effect of local fluctuations in the EBL intensity along each path. We confirm an order of magnitude fluctuations in the local EBL (based on the cumulative light from model galaxy distributions within spheres of 50 h^{-1}Mpc). However, the effect of these fluctuations on the VHEγ-ray opacity is insignificant due to the overall very small contribution of the local EBL to the total EBL. We also investigate the effect that a galaxy crossing the line of sight of the γ-ray source may have on the VHE spectrum. We find that galaxies with stellar masses of $M > 10^{11}$ $\mathrm{M}_{\odot}$ could have a significant effect on the γ-ray absorption. It is unlikely that the observed variation in the spectral index is caused by the proximity of single galaxies to the γ-ray paths as these are extremely rare.

4.1 INRODUCTION

The extragalactic background light (EBL) is the integrated diffuse light from stars and active galactic nuclei (AGNs) emitted through the history of the Universe redshifted to longer wavelengths due to cosmic expansion. The spectrum of the EBL lies between the ultraviolet (UV) and far-infrared (FIR) with two distinct peaks: a first peak at $\sim 1\ \mu$m due to direct stellar emission and a second peak at 100m caused by stellar light that has been absorbed and re-emitted by the intragalactic dust. Since the EBL carries information of the star formation history of the Universe, its measurements can be used to provide constraints on star formation models and the baryonic matter content of the Universe (Dwek, 2001).

Direct measurements of the EBL are difficult because of strong foreground contamination by Galactic and zodiacal light. Nevertheless, efforts have been made to provide upper and lower limits on the EBL using intensity measurements of the sky and deep galaxy counts, respectively (see Dwek, 2001; Dwek & Krennrich, 2013, and references therein). However, setting lower limits based on galaxy counts is less reliable at longer wavelengths since unresolved galaxies become a source of confusion. Furthermore, constraining the EBL in the $10 - 70\,\mu$m range is complicated by the emission from the interplanetary dust (Kelsall et al., 1998).

On the other hand, indirect measurements of the EBL can be obtained by studying the spectral attenuation of distant γ-ray sources. Cosmic γ-rays can be absorbed along the way through pair production, $\gamma + \gamma' \rightarrow e^{+} + e^{-}$, where γ' indicates an EBL photon. This process causes spectral steepening of blazar spectra in the very high-energy (VHE;$E > 10$ GeV) regime (Abramowski et al., 2013). Since the attenuation depends on the γ-ray energy and the EBL density along the line of sight, it can be used to constrain the EBL. This method requires an understanding of the γ-ray source spectrum, which is still a matter under discussion (e.g., Stecker et al., 1996; Dwek & Krennrich, 2005; Aharonian et al., 2006; Mazin & Raue, 2007; Albert et al., 2008). Thus, it is difficult to differentiate between the source-inherent effects and the signature of the EBL on the observed spectrum (Mazin & Raue, 2007).

As illustration of the above, we replicate a figure from Sinha et al. (2014) (Fig. 4.1) that shows a positive correlation between the spectral index (Γ) of the high-frequency peaked BL Lac (HBL) sources and redshift, suggesting that more distant sources have a higher probability of interacting with the EBL along the path leading to the steepening of the VHE spectra. The authors excluded extreme HBLs for homogeneity purposes, which brings out more clearly the observed intrinsic systematic spectral hardening within this blazar class (see also Ackermann et al., 2011). However, even with this homogeneous sample there still is a large scatter in the Γ for sources at the same redshift. Various models of blazar emission mechanisms indicate that blazars have a broad range of γ-ray peak frequencies, and therefore varying VHE spectral indices. In this work, we investigate a possible contribution from the EBL fluctuations to the scatter of the observed spectral indices.

Several models have been developed to derive an overall spectrum of the local EBL and its evolution. These models use different strategies to determine the evolution of the comoving luminosity density as a function of redshift. The most recent models can be classified into four types: 'backward' evolution models, 'forward' evolution models, 'cosmic chemical' evolution models, and 'semi-analytic' models (Dwek, 2001).

Backward evolution models begin with the observed present day luminosity functions for galaxy populations in the local Universe and extrapolate them to higher redshift (e.g. Malkan & Stecker, 1998; Rowan-Robinson, 2001; Stecker et al., 2006). Forward evolution models start with early structure formation scenarios to predict the galactic evolution forward in time (e.g. Dwek & et al., 1998; Razzaque et al., 2009; Finke et al., 2010; Kudoda & Faltenbacher, 2017, , hereafter referred to as KF17). Cosmic chemical evolution models consider basic galaxy ingredients such as gas, metallicity, and radiation content and follow their evolution in a large comoving volume element (e.g. Pei & Fall, 1995; Pei et al., 1999). Semi-analytic models apply physically motivated descriptions and recipes to simulate galaxy formation and evolution (e.g. Kauffmann et al., 1993; Cole et al., 1994; Somerville & Primack, 1999; Gilmore et al., 2012). Semi-analytic models are a more challenging approach, but they provide a better insight into the complex physical processes involved in the production of the EBL.

The standard γ-ray absorption models assume spatially homogeneous EBL densities. However, the spatial galaxy distribution is inhomogeneous on small scales; thus one expects the EBL to fluctuate to a certain degree as well. To what extent fluctuations affect the γ-ray transmissivity is not fully understood. The effect of inhomogeneous EBL densities on γ-ray opacities has been explored by Furniss et al. (2015); Kudoda & Faltenbacher (2016); Kudoda & Faltenbacher (2017) and Abdalla & Böttcher (2017). KF17 predicted maximum changes of ± 10 per cent in the γ-ray transmissivity, which is in agreement with the results reported by Furniss et al. (2015) and Abdalla & Böttcher (2017). A change of ± 10 per cent in the γ-ray transmissivity, however, translates into only marginal differences in the power-law slopes of the absorbed γ-ray spectra ($\lesssim \pm 1$ per cent).

In KF17, we developed a purely analytical framework for computing the EBL fluctuation based on the phenomenologically determined variance of the star formation rate (SFR). In this work we develop a new technique to model the EBL (which may be adaptable for other problems as well) by combining the forward and semi-analytic approaches in order to study the impact of the local environment on the overall EBL spectrum and its effect on the γ-ray opacity of the universe. The forward approach, borrowed from KF17, will be used to model the isotropic contribution to the local EBL from galaxies at large distances, while the semi-analytical galaxy catalogues from the Millennium database (Lemson & Virgo Consortium, 2006; Guo et al., 2013) will be used to create a light cylinder through the Universe to simulate the γ-ray path with a more realistic distribution of galaxies close to the line of sight. Combining the two approaches allows us to model γ-rays on individual paths through a locally inhomogeneous EBL.

The structure of the paper is set as follows. We detail the new EBL model in Section 4.2. The results of the EBL model and comparison with our previous EBL model are presented in Section 4.3. The calculations of the γ-ray opacity are discussed in Section 4.3.2. The case of a galaxy encounter with the γ-ray path is shown in Section 4.4. Finally, we summarize and give a brief conclusion in Section 4.5. In this work we used the WMAP7 cosmological parameters (Ω_m, Ω_b, Ω_Λ, h) = (0.272, 0.0455, 0.728, 0.701 km/s/Mpc).

4.2 MODELLING THE EBL

This work focuses on the effect of the stochasticity of local EBL fluctuations on the absorption of VHE γ-rays. We employ a semi-analytical galaxy catalogue to model the local EBL fluctuations. The spatial information of semi-analytical galaxy positions allows us to investigate the γ-ray absorption along individual γ-ray paths and evaluate the effects of different environments (EBL energy density along the line of sight). Since the universe can be considered homogeneous on scales $\gtrsim 100$ Mpc, it implies that the EBL originating for sources with large distances to the γ-ray paths can be considered homogeneous. However, if the γ-rays pass over or underdense structures such as galaxy clusters or voids, the EBL is expected to take on values higher or lower than the average values.

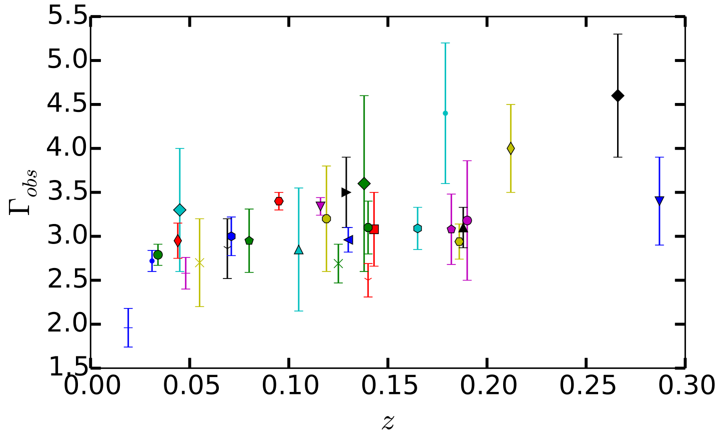

Figure 4.1: Observed spectral indices Γ of HBL as a function of redshift (data obtained from table 1 in Sinha et al. (2014)) excluding extreme HBLS and those with uncertain redshifts.

Consequently, we divide the computation of our EBL model into two parts: the local EBL contribution (within a radius$< 50\,h^{-1}$ Mpc) derived directly from the semi-analytical galaxy positions and brightness and the contribution from a homogeneous, analytically modelled EBL background ($> 50\,h^{-1}$ Mpcc).

4.2.1 The local EBL contribution

The EBL differential specific flux at wavelength λ_0, $\mathrm{dF}_\nu(\lambda_o)$, arriving from sources contained by a comoving volume element $\mathrm{dV}_c(\mathrm{z})$ at redshift z and wavelength λ can be computed as (e.g. Mo et al., 2010)

$$\mathrm{dF}_\nu(\lambda_o) = (1+z)\frac{\mathcal{L}_\nu(\lambda, z)\mathrm{d}V_c(z)}{4\pi d_L(z)^2}, \tag{4.1}$$

where $\mathcal{L}_\nu(\lambda, z)$ and d_L are the comoving specific luminosity density of the sources and their luminosity distance, respectively. Since this formula is used only for distances $\leq 50\,h^{-1}$ Mpc here we ignore the factor $(1+z)$ for the computation of the local EBL contribution.

4.2.1.1 The light-cone cylinder

To investigate the impact of the ambient luminous structures on different γ-ray paths, we use the semi-analytical galaxy catalogue MR7 (Lemson & Virgo Consortium, 2006; Guo et al., 2013) and construct a rectangular volume with

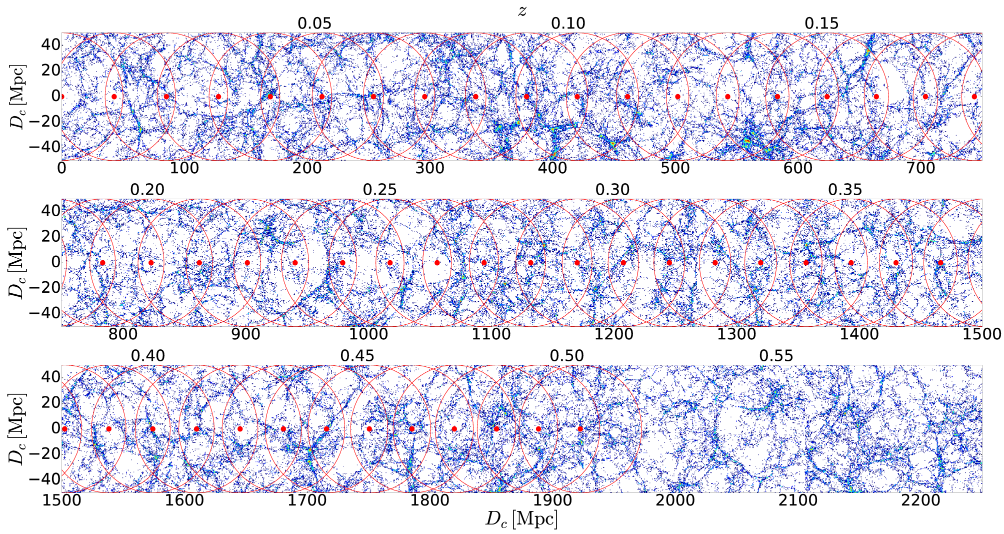

Figure 4.2: Example of the galaxy distribution within a cylinder enclosing an individual γ-ray path with comoving radius of $50\,h^{-1}$ Mpc from $z = 0$ up to $z = 0.5$. The red points in the middle of the cylinder represent the locations where the local EBL density from a sphere of radius 50 h^{-1}Mpc (red circles) was computed. Note that here we are plotting a 10 Mpc slice of the cylinder.

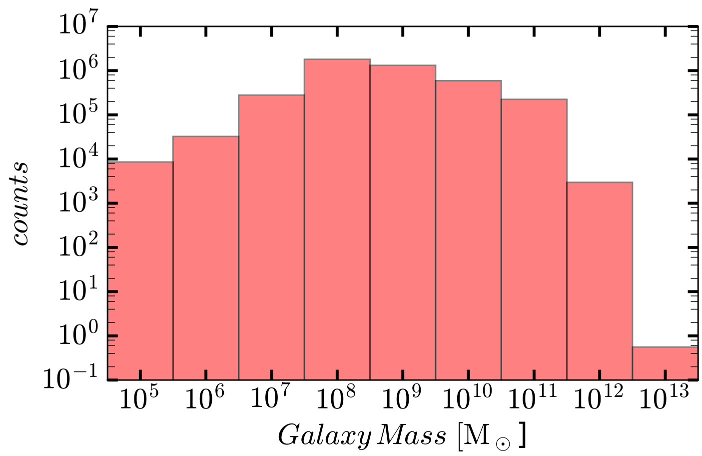

Figure 4.3: The mean galaxy stellar mass distribution within all the 961 cylinders considered. The volume of a cylinder is 15.7×10^6 $(h^{-1}$ Mpc$)^3$.

two dimensions coincident with two edges of the simulation cube and the third dimension extending into redshift space. In essence this is a rectangular section of the cosmic light cone. The MR7 data provides 62 snapshots of a $500^3\,h^{-1}$ Mpc^3 comoving simulation volume from redshift $z = 50$ up to $z = 0$. We draw a total of 961 parallel γ-ray paths (with cylinders with a radius $R = 50\,h^{-1}$ Mpc around them) separated by ~ 15 Mpc through the light cone starting from $z = 0$ up to $z = 0.5$ ($\simeq 2000\,h^{-1}$ Mpc)).

In order to avoid periodic repetition of structures within the light cones we randomly rotate the simulation cubes before stitching them together. More precisely, we cut a slice from each snapshot with a thickness equal to the comoving distance between two consecutive snapshots and place the slices at the comoving distance corresponding to their redshifts. Fig. 4.2 shows an example of the resulting cylinders, where the red dots represent the chosen points (separated by $dz = 0.01$) to calculate the light intensity from the local galaxies located in a sphere with radius of 50 h^{-1} Mpc (plotted as red circles in the figure). The mean distribution of the stellar mass component of the galaxies in all cylinders is shown in Fig. 4.3. The stellar mass of most galaxies in the cylinders lies between 10^7 and 10^{11} $M_\odot$.

To assign a spectrum to every galaxy in the cylinders, we use the galaxy properties age, metallicity, and stellar mass (all listed in the MR7 catalogue) together with the stellar population synthesis library BC03 (Bruzual & Charlot, 2003), assuming each galaxy has only a single stellar population. BC03 uses PADOVA 1994 stellar evolutionary tracks and Chabrier (2003) initial mass functions (IMFs) to determine the high-resolution spectral evolution of stellar populations with different metallicities and ages. Fig. 4.4 shows the dust-free spectrum normalized with solar luminosity ($L_\odot$) at different ages.

To get the total spectrum of the individual galaxies and estimate the light absorbed by the dust, we apply an empirical formula for the light escape fraction from (Razzaque et al., 2009) on the BC03 spectra and generate the stellar component spectrum. The dust content is modelled by three components: large dust grains, small dust gains, and polycyclic aromatic hydrocarbons (PAHs) with the temperatures 40, 70 and 450 K, respectively (Finke et al., 2010). In order to get the dust spectrum we integrate the total energy density of the photons absorbed by the dust and distribute it over three blackbodies representing the three dust components with the fractions0.60, 0.05, and 0.35, respectively. The full spectrum is then obtained by combining the stellar and the dust spectrum. Fig. 4.5 shows dust-free stellar and dust+stellar spectral

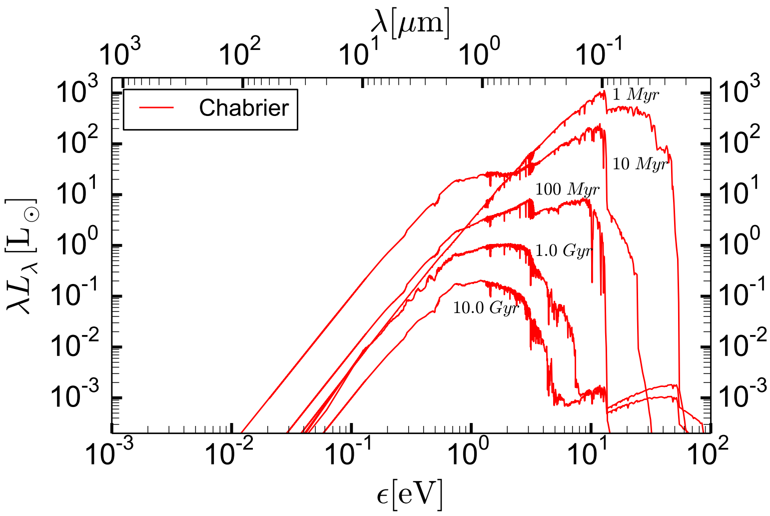

Figure 4.4: The Bruzual & Charlot (2003) dust free spectrum using Padova 1994 evolutionary tracks with Chabrier IMFs at different ages.

energy distributions (SEDs) of the stellar population normalized to $M_\odot$ at an age of 5 Gyr and solar metallicity.

In order to calculate the local contribution of the EBL at the sampling points (the red dots in Fig. 4.2) we derive the EBL intensity by utilizing equation (4.1) and add the contribution of the light from all galaxies within the 50 h^{-1} Mpc comoving sphere. In this way we produce the local EBL spectrum for all sampling points along the line of sight.

4.2.2 The homogeneous EBL background

For the homogeneous EBL background (beyond 50 Mpc) we use our previous EBL forward model (KF17), considering only the contribution from main-sequence stars to the EBL stellar component. The EBL at $z = z_1$ is derived by integrating the contributions from stars of all masses formed throughout the history of the Universe from $z = 10$ to $z = z_1$. The number of photons N emitted from a star with mass $M_\star$ at a specific energy interval $d\epsilon$ and time dt is modelled as blackbody radiation at a given temperature $T_\star$ and radius $R_\star$ from the spherical surface of the star. An IMF $[\xi(M)]$ is then employed to model the mass distribution of the stars. A further element for the integration

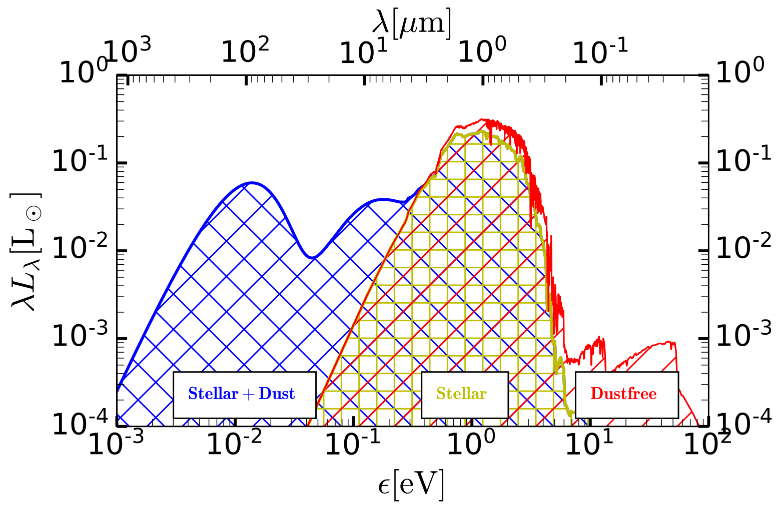

Figure 4.5: Illustration of the composition of a galaxy spectrum normalized with solar luminosity. The dust free model at 5 Gyr from (Bruzual & Charlot, 2003) in red. The yellow represents the stellar emission, while the blue lines is the total spectrum (stellar + dust extinction).

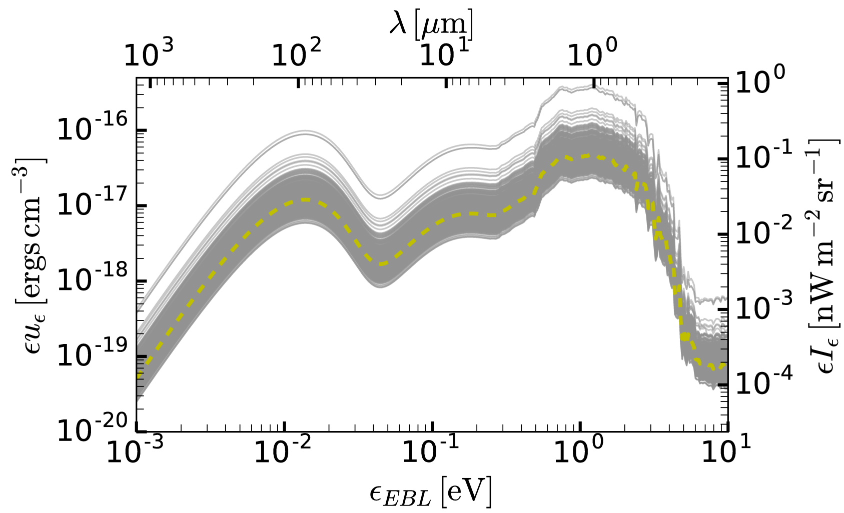

Figure 4.6: The local EBL spectra in different spheres at $z = 0$ (grey lines). The yellow dashed line represents the median local EBL in one sphere as an example. The observed fluctuations between different spheres can be explained by the variation in the number of galaxies or large structures in each sphere and their distances from the centre of the sphere. In other words, the lines reflect the variation of the distance of the large structures from the line of sight.

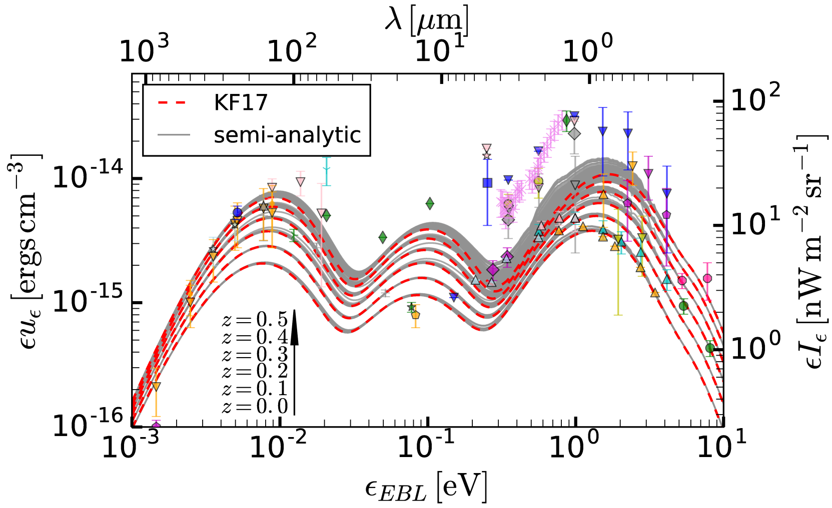

Figure 4.7: The total EBL intensity at different redshifts (grey lines). The red dash-lines represent the analytic KF17 model. The symbols represent EBL measurements: green circle (Xu et al., 2005); red octagon (Gardner et al., 2000); blue triangle down (Bernstein, 2007); cyan triangle up (Totani et al., 2001); magenta triangle down (Mattila, 1990); yellow triangle down (Matsuoka et al., 2011); orange triangle down (Dube et al., 1979); Grey triangle down (Levenson et al., 2007); pink triangle up (Keenan et al., 2010); magenta diamond (Ashby et al., 2013); blue square (Arendt & Dwek, 2003); orange pentagon (Hopwood et al., 2010); green star (Teplitz et al., 2011); Grey plus (Béthermin et al., 2010); cyan triangle down (Finkbeiner et al., 2000); pink triangle down (Matsuura et al., 2011); green triangle up (Berta et al., 2011); Orange triangle down (Fixsen et al., 1998); Grey triangle down (Pénin et al., 2012); red star (Béthermin et al., 2012); Orange dot (Odegard et al., 2007); blue circle (Zemcov et al., 2010); the yellow x (Matsumoto et al., 2005); green diamonds (Kashlinsky & Odenwald, 2000).

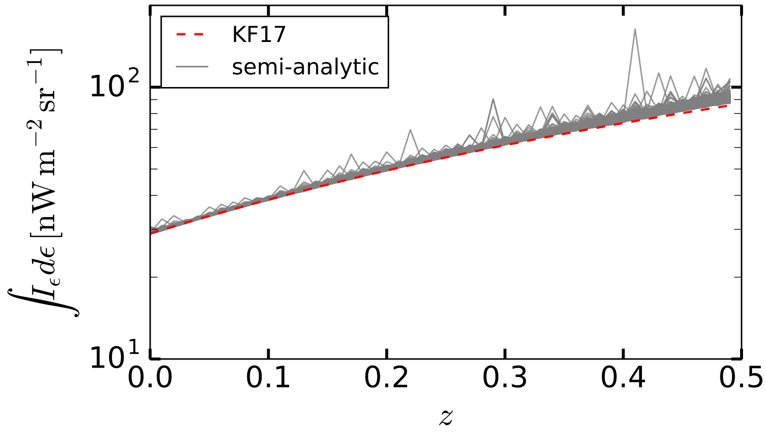

Figure 4.8: The grey lines show the total EBL intensity along the various γ-ray paths (961 cylinders) starting from $z = 0$ up to $z = 0.5$. The red dash-doted line is the pure analytic approach KF17 from Kudoda & Faltenbacher (2017), the red dashed line shows an example of the integrated total EBL intensity in one cylinder

.

of the EBL is the global SFR ($\psi(z)$),

$$\begin{aligned}\frac{dN(\epsilon, z = z_i)_{star}}{d\epsilon dV} =& \mathcal{N} \int_{z=z_i}^{\infty} dz'' \left|\frac{dt}{dz''}\right| \psi(z'') \int_{M_{\min}}^{M_{\max}} dM \xi(M) \\ &\times \int_{\max\{z=0, z_d(M,z')\}}^{z''} dz' \left|\frac{dt}{dz'}\right| \\ &f_{\rm esc}(\epsilon') \frac{dN(\epsilon', M)}{d\epsilon' dt}(1+z'), \end{aligned} \tag{4.2}$$

where $\mathcal{N}$ is the normalization factor for the IMF $\xi(M)$, M_{min} and M_{max} are 0.1 $M_\odot$ and 100 $M_\odot$, $\epsilon' = \epsilon(1+z')$ is the redshifted energy of the EBL photons, z_d is the redshift when the star evolves away from the main sequence, and $\frac{dN(\epsilon',M)}{d\epsilon' dt}$ is the total number of emitted photons per time per energy interval. The averaged photon escape fraction from a galaxy, $f_{\rm esc}(\epsilon')$, is given by an empirical fitting function adapted from Driver et al. (2008). The fraction of photons generated in stars which do not escape is $1 - f_{\rm esc}(\epsilon')$.

To compute the dust component ($\frac{dN(\epsilon,z=0)_{dust}}{d\epsilon dV}$), we followed the recipe discussed in the previous section by replacing the third integral in equation (4.2) with

$$\times \int_{\max\{z=z_1, z_d(M,z')\}}^{z''} dz' \left|\frac{dt}{dz'}\right| (1+z') \sum_{n=1}^{3} \frac{\Omega_n(M)\epsilon'^2}{\exp(\epsilon'/kT_n)}, \tag{4.3}$$

where n is an arbitrary index and Ω_n are the scaling factors of the fraction of starlight reradiated by a particular blackbody at temperature T_n. Combining the stellar and dust components, we can obtain the full spectrum.

4.2.3 The total EBL spectrum

Finally, we derive the total EBL intensity by adding the local contribution at z_i to the homogeneous contribution $z_i - 0.01$, which is approximately the redshift corresponding to a 50 h^{-1}Mpc comoving distance (the radius of the sphere used to compute the local EBL contribution). The comoving radius of the observable Universe is roughly 14.26 Gpc, which is roughly two orders of magnitude larger than the radius of the sphere used for the computation of the local EBL contribution. Therefore, one would expect the light intensity of the homogeneous background to be roughly two orders of magnitude larger than the intensity from the local contribution. Since the analytic background model only considers main-sequence stars and assumes a redshift-independent IMF and dust absorption to determine the EBL density, this results in an EBL density lower than the observed one.

The inclusion of the post-main-sequence stars in the local EBL increases the EBL density slightly compared to the analytical model but this contribution is not sufficient to outweigh the shortfall of EBL contribution from the analytical model.

4.3 RESULTS

In this section we first present the results of our hybrid EBL model and a comparison with our previous pure forward analytic EBL model. We then discuss the fluctuations of the γ-ray opacity using the EBL density along the different γ-ray paths.

4.3.1 EBL spectra

We apply the method described in Section 4.2 to calculate the EBL energy density, that is model the contribution of the local EBL and the homogeneous

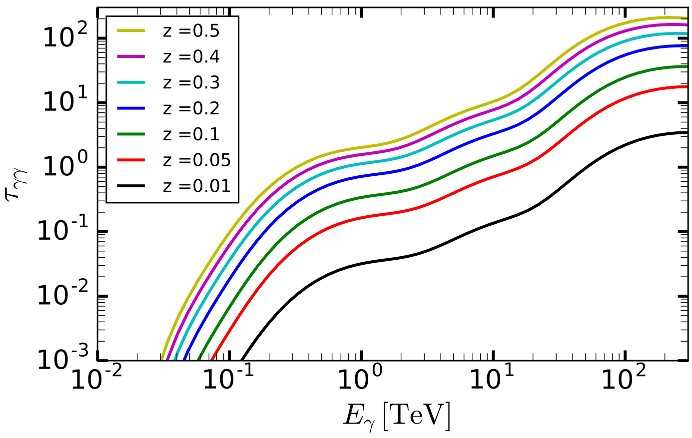

Figure 4.9: The γ-ray opacity averaged over all γ-ray paths at different redshifts.

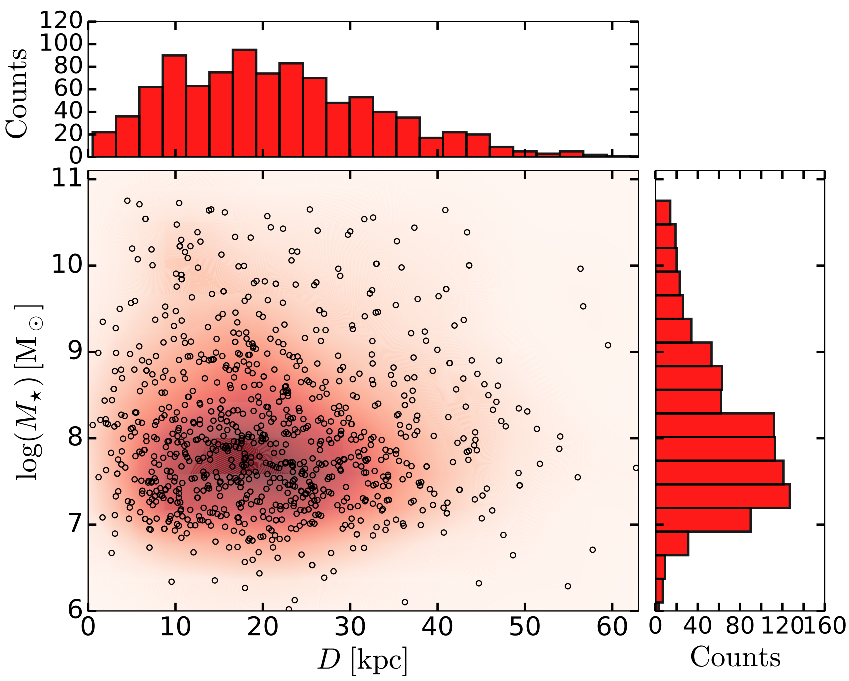

Figure 4.10: The distribution of the distances and stellar masses of the galaxies closest to the individual γ-ray path (one galaxy per γ-ray path).

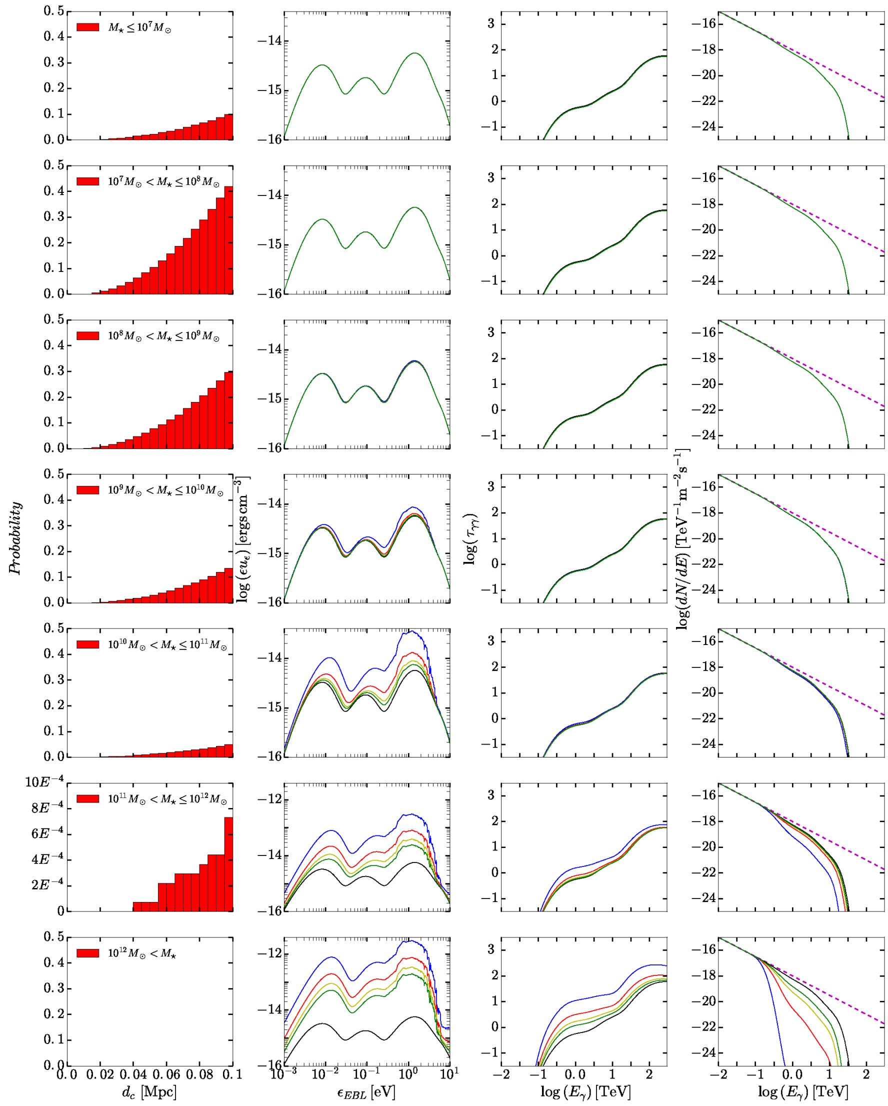

Figure 4.11: Effect of close encounter between the γ-ray path and an intervening galaxy on the EBL energy density, the γ-ray opacity and the VHE γ-ray spectrum. The intervening galaxy is assumed to be located at a distance corresponding to $z = 0.15$. The first column from the left shows the probability distribution of finding a galaxy at a specific radius (derived from the relative positions of the semi-analytical galaxy population and the assumed γ-ray paths), where the rows from top to bottom represent different stellar mass bins. The second column shows the impact on the EBL energy density when we insert a galaxy at 20, 40, 60 and 80 kpc from the line of sight represented by blue, red, yellow and green lines, respectively. For comparison the EBL energy density at $z = 0.15$ without intervening galaxy is shown by the black line. Assuming the γ-ray source at $z = 0.16$, the third column gives the opacities corresponding to the different EBL spectra shown in the second column. The last column presents the impact of the altered opacities on the shape of VHE spectra with intrinsic power law index of $\Gamma = -1.5$ at $z = 0.16$. The dashed magenta line indicates the intrinsic VHE spectrum without EBL absorption.

background separately. Fig. 4.6 shows the local EBL spectra from the 961 spheres at $z = 0$ as grey lines. The median of the spectra is indicated by the yellow dashed line. We observe an EBL intensity variation of one order of magnitude between the spheres, which is a result of the different galaxy content within the individual $50\,h^{-1}$Mpc spheres. We observe a steep decline of the local EBL intensity above 4 eV. This is due to the prevalence of galaxies with old stellar populations (see Fig. 4.4).

In Fig. 4.7 we show the hybrid total EBL spectra (the summation of the local contribution and the homogeneous background) within all light-cone cylinders at different redshifts as grey lines and compare them with the EBL intensity from our previous pure analytic model (KF17), displayed as red dashed lines and observations given by the symbols. The total EBL intensity increases with redshift, which is a consequence of the increasing number density of galaxies in physical coordinates. The total EBL spectrum at $z = 0$ is ± 1 per cent the spectrum in the KF17 model. This is the result of the more comprehensive simple stellar population (SSP) evolution model used to determine the emission from the semi-analytical galaxies employed for the estimation of the local EBL here.

The magnitudes of the total EBL intensity derived from our model are at the lower limit of the observations but roughly in agreement with the data points by Totani et al. (2001) and Fixsen et al. (1998). The low model EBL intensities are caused by the oversimplified treatment of the stellar component employed for the calculation of the homogeneous background. Since our main focus is the impact of the EBL fluctuations on γ-ray opacity, an exact matching of the observed EBL magnitudes is not necessary.

The fluctuations in the total EBL, that is the variation of the magnitudes of the model EBL spectra for a specific redshift (bundles of grey lines in Fig. 4.7), are small compared to the fluctuations in the local EBL (Fig. 4.6) because the isotropic background is more than ~ 100 times brighter than the local contributions. The fluctuations between ~ 0.004 and 4 eV are more visible as a result of the local EBL spectrum shape (see Fig. 4.6) where older galaxies dominate the spectrum.

Fig. 4.8 shows the evolution of the total integrated EBL spectrum ($\int I_\epsilon d\epsilon$ from 0.001 to 10 eV) as a function of redshift. Each grey line displays the integrated EBL intensity along an individual γ-ray path. As expected the amplitude of the fluctuations here also increases with redshift for the same reason mentioned above. The red dashed line depicts the KF17 model and indicates good agreement between the new semi-analytical approach and the KF17 model.

4.3.2 γ-ray opacity

Based on the total cross-section σ for pair production in the photon-photon interaction described in (cf. Gould & Schréder, 1967), we calculate the γ-ray opacity $\tau_{\gamma\gamma}$ as a function of the γ-ray energy E_γ and redshift, z (cf. Razzaque et al., 2009):

$$\tau_{\gamma\gamma}(E_\gamma, z) = c\pi r_0^2 \left(\frac{m_e^2 c^4}{E_\gamma}\right)^2 \int_0^z \frac{dz_1}{(1+z_1)^2} \left|\frac{dt}{dz_1}\right| \times \int_{m_e^2c^4/E_\gamma(1+z_1)}^{\infty} d\epsilon_1 \frac{u_{\epsilon_1}}{\epsilon_1^3} \overline{\varphi}[s_0(\epsilon_1)] \,, \tag{4.4}$$

where r_0 is the classical electron radius, $s = E_\gamma(1+z_1)\epsilon_1/2m_e^2c^4$ is the centre-of-momentum energy square, $\varphi[s_0(\epsilon_1)] = \int_1^{s_0(\epsilon)} \frac{2s\sigma(s)}{\pi r_0^2} ds$, and $s_0 = E_\gamma(1+z_1)\epsilon_1/m_e^2c^4$.

Using the above integral we determine the optical depth as function of γ-ray energy for different redshifts. Fig. 4.9 shows the γ-ray opacity in the range $0.01-300$ TeV for the 961 γ-ray paths as a function of the γ-ray source redshift. The opacity increases rapidly above 1 TeV, implying that γ-ray photons at the tail of the spectrum are most attenuated. The overall opacity also increases with redshifts, showing that γ-rays from distance sources experience more attenuation along their path. In addition, the resulting opacities for all γ-ray paths overlap each other at all redshifts. This means that the small EBL fluctuations along the γ-ray path, shown in Fig. 4.8 as grey zigzag lines, are smoothed out over redshift, suggesting an average opacity along vast distances. We can also say that the different structures along the various γ-ray paths have no impact on the total EBL density and the consequent opacity over long distances. The absence of fluctuations on the total EBL densities and opacities along all possible γ-ray paths simulated here agrees with the purely analytical results in KF17 where the variation in the EBL and the opacity was only ± 1 per cent.

In conclusion, we find that the γ-ray opacities along the different γ-ray paths simulated here do not show significant fluctuations.

Because of the finite number of γ-ray paths used here in combination with the relatively low number densities of massive galaxies (see Fig. 4.10), which substantially enhance the local EBL photon density, we were not able to explore close encounters between massive galaxies and the γ-ray paths in a comprehensive manner. Therefore, in the following section we investigate close encounters of galaxies with γ-ray paths by manually moving a model galaxy into the line of sight.

4.4 THE IMPACT OF CLOSE GALAXY ENCOUNTERS

In this section we study the effect of galaxy encounters with the γ-ray path on EBL energy density, opacity and γ-ray spectral index. To obtain an insight into the frequency of close galaxy-γ-ray encounters, we select for each γ-ray path the galaxy with the minimal perpendicular distance to the line of sight. Fig. 4.10 shows the mass distribution of the 961 selected galaxies as a function of distance from their corresponding γ-ray paths. The stellar mass of most of these galaxies falls in the range of $10^7 - 10^8$ $M_\odot$ between 10 and 30 kpc from the line of sight. No galaxy with mass $\gtrsim 10^{11}$ is found at a distance less than 60 kpc from the γ-ray path. This is consistent with the overall stellar mass distribution shown in Fig. 4.3, which indicates a stellar mass range of the model galaxies from 10^7 to 10^{10} $M_\odot$. In general, massive galaxies are rarely found very close to the γ-ray paths simulated here.

However, one also has to consider the gravitational lensing effect caused by an intervening galaxy, which counteracts the steepening of the VHE γ-ray spectrum if the line of sight goes directly through the visible part of the intervening galaxy (Barnacka et al., 2014). The deciding factor here is the impact relative to the Einstein radius r_E, which characterizes the strength of the gravitational lensing. The Einstein radius depends on the mass of the encountering galaxy and the angular distances from the γ-ray source to the observer, from the γ-ray source to the encountering galaxy, and from the encountering galaxy to the observer. The lensing effect is significant if the γ-ray passes through one $r_E \sim 5$ kpc of the intervening galaxy. Therefore, in this work we choose the distance between the γ-ray path and the intervening galaxy to be $\gtrsim 20$ kpc so that we cover the effect of the encounter outside the lensing radius.

In order to quantify the effect of a close encounter we now insert a galaxy close to the γ-ray path manually with a very simple model. In principle, this will allow us to vary the distance, mass, and redshift of the encountering galaxy, and investigate their importance. Fig. 4.11 summarizes the effects of the presence of a galaxy near the line of sight at $z = 0.15$ with the γ-ray source at $z = 0.16$. There are no changes in the opacities if we change the encountering galaxy's redshift. Each row in the figure represents different stellar mass bins starting from $M < 10^7$ $M_\odot$ at the top to $M > 10^{13}$ $M_\odot$ at the bottom with a logarithmic mass bin. The first column shows the probability of finding a galaxy within a given perpendicular distance from the line of sight. To compute the probability, we sum all galaxies at certain mass and radial bins along all lines of sight and divide them by the total number of galaxies inside a maximum radius of 0.1 Mpc. Using the total number of galaxies for normalization instead of the number of galaxies in each mass bin separately enables us to easily compare the relative radial probability distribution of the galaxies in each mass bin. The second column displays the impact of a close galaxy encounter with the line of sight on the EBL at different distances (20, 40, 60, 80 kpc). The third column gives the effect on the corresponding γ-ray opacity due to the EBL, and the last column shows the absorbed VHE γ-ray spectrum assuming an intrinsic $\Gamma = -1.5$ (displayed in black).

We find that the EBL density does not change much if the encountering galaxy has a stellar mass less than 10^8 $M_\odot$, even for a very close encounter (e.g. as close as ~ 20 kpc), whereas if the galaxy has stellar mass greater than 10^9 $M_\odot$ the impact can be significant depending on the distance from the line of sight. Large galaxies with stellar masses $\sim 10^{11}$ $M_\odot$ have a substantial effect on the spectrum even at relatively large distances (e.g. ~ 80 kpc) from the line of sight. However, the impact on the opacity can only be observed if the galaxy's stellar mass is higher than 10^{10} $M_\odot$.

Table 4.1 shows the spectral index (Γ) fitted at two γ-ray (E_γ) energy ranges ($0.01 < E_\gamma \leq 0.33$ TeV and $0.33 < E_\gamma \leq 10.8$ TeV) for different galaxy masses and distances. The last row in the table shows the spectral index for this model where there is no galaxy inserted near the γ-ray path. The effects of a galaxy encounter with the γ-ray path are significant only in the highest energy range.

A steepening of the spectral index Γ due to a galaxy located close to the γ-ray path can only be seen if the galaxy's stellar mass is larger than 10^{10} $M_\odot$. The significance of the effect varies with the γ-ray energy: For $E_\gamma < 0.33$ TeV, there is no observable change in Γ; for the $0.33 < E_\gamma \leq 10.8$ TeV range a galaxy with stellar mass 5×10^{11} $M_\odot$ causes a clearly visible steepening of the γ-ray spectrum if it is close to the line of sight ($\lesssim 40$ kpc). Although the probability of finding galaxies with stellar mass $> 10^{12}$ $M_\odot$ is extremely low,

Table 4.1: The spectral index Γs for different masses of galaxies at different distances

Mass [$M_\odot$]	Energy [TeV]	$\Gamma_{20\,\mathrm{kpc}}$	$\Gamma_{40\,\mathrm{kpc}}$	$\Gamma_{60\,\mathrm{kpc}}$	$\Gamma_{80\,\mathrm{kpc}}$
5×10^6	$0.01 \leq E_\gamma \leq 0.33$	1.50	1.50	1.50	1.50
	$0.33 < E_\gamma \leq 10.8$	1.53	1.53	1.53	1.53
5×10^7	$0.01 \leq E_\gamma \leq 0.33$	1.50	1.50	1.50	1.50
	$0.33 < E_\gamma \leq 10.8$	1.53	1.53	1.53	1.53
5×10^8	$0.01 \leq E_\gamma \leq 0.33$	1.50	1.50	1.50	1.50
	$0.33 < E_\gamma \leq 10.8$	1.53	1.53	1.53	1.53
5×10^9	$0.01 \leq E_\gamma \leq 0.33$	1.50	1.50	1.50	1.50
	$0.33 < E_\gamma \leq 10.8$	1.53	1.53	1.53	1.53
5×10^{10}	$0.01 \leq E_\gamma \leq 0.33$	1.50	1.50	1.50	1.50
	$0.33 < E_\gamma \leq 10.8$	1.54	1.53	1.53	1.53
5×10^{11}	$0.01 \leq E_\gamma \leq 0.33$	1.50	1.50	1.50	1.50
	$0.33 < E_\gamma \leq 10.8$	1.62	1.55	1.54	1.54
5×10^{12}	$0.01 \leq E_\gamma \leq 0.33$	1.53	1.51	1.50	1.50
	$0.33 < E_\gamma \leq 10.8$	2.39	1.75	1.63	1.59
No galaxy	$0.01 \leq E_\gamma \leq 0.33$	1.50			
	$0.33 < E_\gamma \leq 10.8$	1.53			

they could have an enormous effect on the γ-ray spectrum even if they are located as far as ~ 80 kpc form the line of sight. The scatter in the observed spectral indices Γ of the VHE γ-ray sources displayed in Fig. 4.1 cannot be caused by galaxy proximity to the γ-ray paths as they are too infrequent to cause the amount of scatter observed.

4.5 SUMMARY AND CONCLUSION

With this work we introduce a new hybrid EBL model combining semi-analytic and forward evolution approaches to determine the EBL and its fluctuations in a realistic manner. Instances of the local EBL are calculated at the centre of 50 h^{-1}Mpc spheres as the cumulative intensity of all galaxies within those spheres. The galaxy properties are obtained from the MR7 galaxy catalogue. The spectra of individual galaxies are generated using those galaxy properties and the stellar population synthesis spectral library BC03. The EBL originating from all sources outside the 50 h^{-1}Mpc spheres is assumed to be homogeneous and calculated analytically following KF17. We find one order of magnitude fluctuations in the local EBL. However, when we compute the total EBL by adding the homogeneous background contribution the variation is less than ~ 1 per cent. This is expected as the local EBL contribution is only a small fraction of the total EBL intensity.

Based on the hybrid model, we calculate the EBL along ~ 1000 γ-ray paths up to $z = 0.5$; that is, enveloping the γ-ray we construct light-cone cylinders of 50 h^{-1}Mpc comoving radius through the MR7 simulation volume within which we compute the local EBL based on the local galaxy content. The EBL beyond the cylinder is determined analytically for every time-step. The hybrid EBL model approach then allows us to integrate the VHE γ-ray absorption along the γ-ray paths and determine the change of the observed γ-ray spectral index due to the preferential absorption of VHE γ-rays by the EBL photons.

The integrated opacities agree with the observed steepening of the hard γ-ray spectra as a function of redshift. But, we find only negligible variations of the opacities along the different γ-ray paths. Thus, our hybrid model which takes into account the contribution of individual galaxies close to the γ-ray path cannot account for the scatter in the spectral index seen in Fig. 4.1.

To cover very close encounters of galaxies with γ-ray paths (which are not apparent in our statistical sample), we manually insert an individual galaxy of different stellar mass 5×10^6 $M_\odot$ to 5×10^{12} $M_\odot$) very close to the line of sight. We then compute γ-ray absorption and the increase of the spectral index Γ, which is set to be $\Gamma = -1.5$ without absorption. We find that the presence of a single galaxy with stellar mass $< 10^9$ $M_\odot$ has no measurable impact on Γ independent of its distance to the line of sight. On the other hand, high-mass galaxies with $10^{10} - 10^{12}$ $M_\odot$ at distances less than 50 kpc from the line of sight cause a clearly visible steepening of the VHE γ-ray spectrum. Given the future increase of the number of observed VHE γ-ray sources (roughly a factor of 10 with the coming Cherenkov Telescope Array, CTA), these encounters may become more important.

Chapter 5

EVALUATING THE POWER SPECTRUM OF THE EXTRAGALACTIC BACKGROUND LIGHT

This work is in preparation for publication.

Abstract

In this work we discuss a model of the extragalactic background light (EBL) which is based on the representation of the EBL intensity contrast in Fourier space. In particular, we describe the EBL and its fluctuations by computing its three dimensional power spectrum, a concept which is well known from the description of cosmic density fields. The EBL itself is derived from a semi-analytical galaxy catalogue based on the Millenium dark matter simulation. The amplitude of the EBL fluctuations is about four orders of magnitude lower than those of the corresponding matter fluctuations. We find that on scales $\lesssim 10$ Mpc the amplitudes of the EBL power spectrum are six orders of magnitude lower than the corresponding amplitudes of the matter power spectrum. An obvious explanation for this behaviour is the $1/r^2$ law for the light distribution around point sources (i.e. galaxies) which blurs the spatial EBL intensity distribution compared to the matter density field. We find a substantial increase of the amplitudes on scales of $\gtrsim 100$ Mpc, which corresponds to the size of large voids and super-clusters. At these scales the amplitudes of the EBL power spectrum are four orders of magnitude lower than the corresponding amplitudes of the matter power spectrum. Comparing the power spectra of the EBL and the underlying matter distribution we determine the EBL-matter bias factor as a function of wave number k. Knowing the bias factor between EBL and matter distribution gives way for a theoretical interpretation of possible future EBL fluctuation measurements. It also allows one to model the distribution of light and matter in a realistic and efficient way.

5.1 INTRODUCTION

The spectrum of the extragalactic background light (EBL) spans from ultraviolet to infrared wavelengths. However, the foreground emission from our Galaxy and the zodiacal light from our solar system in this range complicate its measurements. Measuring the EBL directly is a daunting task, but one can measure the fluctuation to set limits on the intensity (Hauser & Dwek, 2001; Dwek & Krennrich, 2013).

The EBL traces radiation from the formation and evolution of structure in the Universe since the epoch of recombination. Thus, measurements of the EBL spectrum may serve to constrain models of the star formation history of the Universe. It has been established that most of the EBL is produced by discrete galactic or primordial stellar sources (Dwek & Krennrich, 2013). EBL source models, therefore, should predict the fluctuations in their number. Fluctuations in the EBL reflect number density fluctuations of the sources, i.e. their clustering properties driven by the underlying distribution of gravitating matter.

Several studies of EBL fluctuations have been conducted, the first being in the optical band by Shectman (1973, 1974), and Kashlinsky et al. (1996a) in the infrared using the COBE DIRBE maps (see Kashlinsky et al., 2018, for a review on infrared fluctuations). Based on these studies the spectrum in the optical band has a strong dependence on the luminosity density of the Universe with a similar covariance structure as the large scale galaxy distribution. The minimum fluctuations in the infrared is found to be 10 per cent,which is much larger than seen in the galaxy distribution. More recently, Kashlinsky et al. (2012) analyzed the 3.6 and 4.5 μm bands from Spitzer Extended Deep Survey and confirmed infrared EBL fluctuations more than 10 times larger as expected from known galaxy populations on 1° angular scales.

In a previous study (Kudoda & Faltenbacher, 2017) we have shown based on a statistical approach that the spatial fluctuations of the star formation rate produce ± 1 per cent fluctuations of the EBL. In this work we employ a power spectrum approach to model the spatial fluctuations of the EBL based on the underlying cosmic matter density field. The comparison of a realistically modeled EBL (Kudoda & Faltenbacher, 2018) and the underlying matter power spectra allows us to derive a scale dependent bias factor, $b(k)$, between EBL and matter distribution. We determine $b(k)$ in a heuristical manner which allows us to analyze the statistical properties of the EBL in view of the underlying matter distribution. This approach also provides an efficient way to generate realistic EBL distributions from known cosmic density fields without the necessity to model the galaxy population. More specifically, with the known bias function one can use any N-body simulation, compute its Fourier spectrum, multiply the amplitudes with the bias function and superimpose the altered waves to generate a realization of associated EBL distribution.

The structure of this paper is as follows. Theoretical background is given in Section 5.2. In Section 5.3 the EBL model is presented. The EBL power spectrum calculation is given in Section 5.4. Finally, we discuss and give a brief conclusion in Section 5.6. We used the WMAP7 cosmological parameters $(\Omega_m, \Omega_b, \Omega_\Lambda, h) = (0.272, 0.0455, 0.728, 0.701$ km/s/Mpc) throughout this work.

5.2 THEORETICAL BACKGROUND

5.2.1 Cosmic density field

In the standard paradigm of the large scale structure formation, the initial density fluctuations, which are the seeds for subsequent structure formation, are grown and amplified by gravity. The origin of these fluctuations is believed to be quantum fluctuations magnified to macroscopic scales by inflation. The large structures are reflections of these initial conditions of the cosmic density field. To fully describe the cosmic density field one needs to determine the density, ρ, or equivalently, the density contrast $\delta(x) = \rho(x)/\overline{\rho} - 1$ at any point in space. However, this is infeasible due to the infinite number of field values. An alternative is to consider the Fourier representation of the density field or the density contrast. The amplitudes of the plane waves allow to investigate the statistics of the Universe in a global (non localized) manner at sufficiently large scale. Fortunately, the density distribution of the Universe can be represented by a Gaussian[11] random field. In a statistical sense, the density field of the Universe is fully determined by its power spectrum.

5.2.2 Power spectrum of Gaussian random fields

It turns out that a homogeneous and isotropic Gaussian random field is a good approximation to describe the linear (or primordial, i.e. before gravitational evolution causes an exchange of information between the basic wave modes)

[11] The field $\delta(\overrightarrow{r}) = \frac{V}{(2\pi)^3} \int \delta_{\overrightarrow{k}} e^{-i\overrightarrow{k}.\overrightarrow{r}} d^3k$ is called a Gaussian field when the phases $\delta_{\overrightarrow{k}} = |\delta_{\overrightarrow{k}}| e^{i\phi_{\overrightarrow{k}}}$ of the different Fourier components are uncorrelated.

density fluctuations of the Universe (e.g. Bardeen et al., 1986). Thus, the cosmological principle which states that the Universe ought to be statistically homogeneous and isotropic at sufficiently large scale, is obeyed. The power spectrum $P(k)$ is related to basic wave modes by the following expression:

$$P(k) = \langle |\delta(k)|^2 \rangle, \tag{5.1}$$

where $\delta(k)$ is the Fourier transformation of the density contrast, $\delta(x)$, and k is the Fourier mode or wavenumber. For a Gaussian random field the power spectrum entails the complete statistical information of the density distribution.[12].

The power spectrum is directly predicted from the theory of standard cosmology. The primordial power spectrum is assumed to follow a power-law ($p(k) \propto k^n$, where $n \sim 1$ is found for inflationary models, Baugh, 2000). The evolution of the shape of power spectrum on different scales depends on the growth of the fluctuation with the corresponding wavelengths (Baugh, 2000). During linear evolution all fluctuation grow independently. In the non linear regime the waves of different wavelength do interact.

5.2.3 Bias between galaxy and matter distribution

Observation of distribution of galaxies is needed to constrain the cosmological models that predict the distribution of total matter (dark matter) in the Universe. For this, we need some kind of relation between the observed distribution of galaxies and dark matter. The simplest relation is to assume that density fluctuations of both galaxies and dark matter are identical ($\delta_{galaxy}(x) = \delta_{dark\ matter}(x)$) on some scale x.

However, the number density of galaxy clusters is much less compared to the number density of the galaxies. Therefore, one expects a strong bias in the density field of clusters of galaxies than in the galaxies density field (Kaiser, 1984). More generally Davis et al. (1985) extended this hypothesis as a bias between galaxy and dark matter. The simplest form of their hypothesis is called a linear bias:

$$\delta_{galaxy}(x) = b\, \delta_{dark\ matter}(x), \tag{5.2}$$

[12] The statistical properties of the density field can also be determined by the two point correlation function $\xi(r)$. The two point correlation function is the Fourier transformation of the power spectrum, and is given as: $\xi(r) = \frac{1}{2\pi^2} \int_0^\infty k^2 P(k) \frac{\sin(kr)}{kr} dk$.

where b is a constant bias that is independent of scale.

The relation between galaxy distribution and matter field is more complex and may have dependencies other than density (such as merger history and gas temperature etc.), which impact the bias factor, resulting in a nonlinear scale and time dependencies. Also different galaxy populations can have different relations[13] (Strauss et al., 2000). In order to compute the bias ratio using the power spectrum, a square root must be introduced as given in Coles & Erdogdu (2007):

$$P_{galaxy}(k) = b^2(k)P_{matter}(k), \tag{5.3}$$

5.2.4 Bias between EBL intensity and matter distribution

In this work we focus on the relation between the distribution of photons and the matter field. The spatial distribution properties of light sources correlate with the emitted background photons to a certain degree. However, the light distribution around point secures (i.e. galaxies) follows a $1/r^2$ profile. This correlation is expected to be smoother than the galaxy distribution on small scales. Furthermore, any processes which cause a bias between the overall gravitating matter and the galaxy distribution, such as radiative and feedback processes may cause a deviation of photon and matter fields (Baugh, 2000). In order to describe the deviation phenomenologically, we will compare the power spectra of both components.

If we use a sample that is drawn randomly from a Gaussian distribution field, it is expected to be homogeneous, implying a flat power spectrum. Therefore, if the density of the EBL photons is homogeneously distributed in the Universe, as it is commonly assumed (Dwek, 2001; Hauser & Dwek, 2001; Dwek & Krennrich, 2013), it should produce a flat power spectrum.

5.3 THE EBL MODEL

In order to model the EBL we used a mock galaxy catalogue by Guo et al. (2013), which is based on the Millennium simulation run 7 (MR7). The MR7 is a cosmological N-body simulation that uses a customized version of GAlaxies with Dark matter and Gas intEracT 2 (GADGET2; Lemson & Virgo

[13]More generally, the form of the bias can be written as: $\delta_{galaxy}(x) = f(\delta_{dark-matter}(x)) + \epsilon$, where f is a bias function and ϵ expresses the dependence on physical variables.

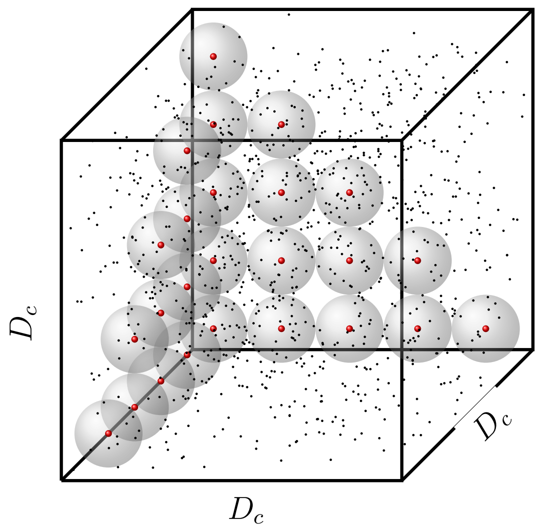

Figure 5.1: Schematic representation of the MR7 simulation box with grid points (red points). The blue points represents galaxies in the simulation box. The gray spheres represent the 50Mpc spheres used in the calculation of the EBL around each point in the grid.

Consortium, 2006). The MR7 simulate 2160^3 dark matter particles (with $m_p = 8.61 \times 10^8\, M_\odot$) within $(500\,\mathrm{Mpc/h})^3$ box. Simulation outputs are stored in 62 snapshots between redshift $z = 50$ and $z = 0$. The Millennium simulation web-portal provides dark matter halo catalogues and associated *merger trees*. In addition, mock galaxy catalogues can be obtained, which are based on a sophisticated semi-analytic model (Guo et al., 2013). The galaxy catalogues comprise comprehensive information of the individual galaxies, such as star formation history, gas content, color composition etc. Unfortunately, the galaxy spectra are not publicly available, therefore, we generate the spectra based on the information of the stellar population as described in the subsequent paragraph.

To determine the overall EBL spectrum, we generate the spectrum of individual galaxies in the MR7 catalogue, assuming that each galaxy contains a single stellar population. Using the stellar population synthesis library BC03 (Bruzual & Charlot, 2003), we select a stellar spectrum (absorption free) for each galaxy according to its age and metallicities; and normalize the spectrum by its stellar mass. In order to model the dust absorption/remission, we apply the empirical formula presented in Razzaque et al. (2009) and estimate the amount of light absorbed by the dust. Thereafter, we redistribute the energy absorbed by the dust into three black-bodies with temperatures of 40, 70, and

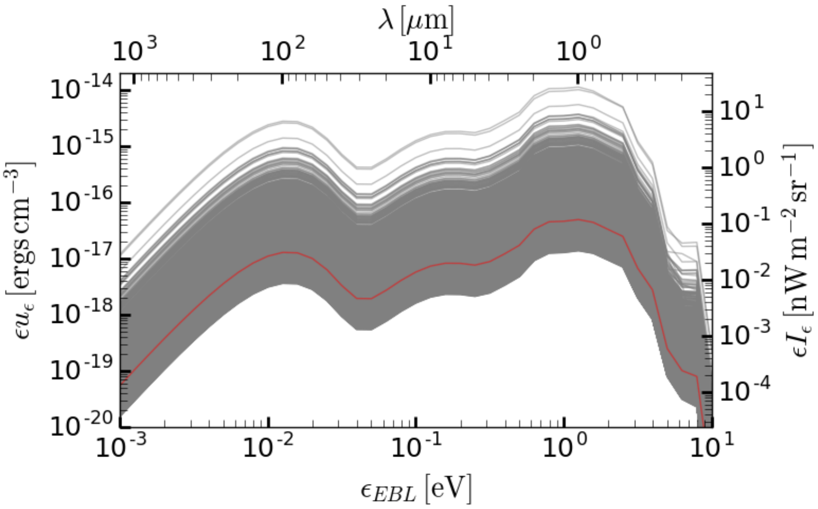

Figure 5.2: The local EBL spectra from the 1,000,000 points in the grid. The red line is the median spectrum.

450 K respectively, as representations of the dust components (i.e., large; small dust gains; and polycyclic aromatic hydrocarbons (PAHs)).

After determining the spectrum emitted from each galaxy in the simulation box, we choose a 3D grid ($100 \times 100 \times 100$) inside the $(500\,\mathrm{Mpc/h})^3$, at $z = 0.0$ and compute the flux received within spheres of certain radii R_s at each point of the grid. Figure 5.1 shows a schematic of the grid points. Figure 5.2 shows the local EBL spectra for all the $1,000,000$ points computed using $R_s = 50\,\mathrm{Mpc/h}$ spheres, assuming periodic boundary condition. A homogeneous EBL background spectrum, computed following Kudoda & Faltenbacher (2018), is then added to the local flux to drive the total EBL spectrum for all grid points at $z = 0.0$.

5.4 THE EBL POWER SPECTRUM

In order to compute the power spectrum, which will be used to compute the bias factor $b(k) = \sqrt{P_{EBL}(k)/P_{matter}(k)}$, we use the bolometric EBL intensity ($I_{\mathrm{bol,point}}$) for all points in the grid by integrating each EBL spectrum over the energy:

$$I_{\mathrm{bol,point}} = \int_{0.001\,\mathrm{eV}}^{10\,\mathrm{eV}} I_{\epsilon,point} d\epsilon, \tag{5.4}$$

This is done to reduce the computational cost, since our aim is to present a proof of concept rather than a detailed modelling of the EBL spectrum. The approach is, however, extendable to the spectrum in an obvious manner.

In the next step, we then compute the bolometric EBL contrast (δ) of all the grid points as:

$$\delta_{EBL}(x) = \frac{I_{i\ \mathrm{bol,point}}}{\overline{I}_{\mathrm{bol}}} - 1, \tag{5.5}$$

where $\overline{I} = \frac{\sum_{i=1}^{1000000} I_{i\ \mathrm{bol,point}}}{1{,}000{,}000}$ and x gives the coordinates of the individual grid points. The Fourier representation of the bolometric EBL contrast, $\delta_{EBL}(k)$ is then employed to compute the 3D power spectrum:

$$P_{EBL}(k) = \langle |\delta_{EBL}(k)|^2 \rangle. \tag{5.6}$$

Convergence test

The adaption of 50 Mpc as radius for the light collecting spheres within which the individual galaxies are used, allows us to consider the local EBL as a smoothing scale. In order to understand how this smoothing scale affects the power spectrum, we perform a convergence test. For this purpose the power spectrum is computed using the local EBL intensity only (without adding the homogeneous background). Figure 5.3 shows the power spectrum for the local EBL using different spheres radii (5, 25, 50, and 100 Mpc).

If the EBL distribution were homogeneous (as assumed in most of the EBL models), one expects an entirely flat power spectrum. However, Fig. 5.3 shows that there exist two regimes where the power is approximately constant: one for scales larger than 100 Mpc and the other for scales below 10 Mpc. The power on large scales is about 3 orders of magnitude larger than the power on small scale. The origin of the large scales power comes from super-clusters and void structures which are known to extend to $\gtrsim$ 100 Mpc. The drop of power for scales $\lesssim$ 10 Mpc is most likely caused by the superposition of light emission profiles around point sources. The choice of 50 Mpc light collecting radii seems to be justified as it converges at the small scales $\lesssim$ 10Mpc and still does not 'blur' the power associated with the super structures.

5.5 THE EBL BIAS FUNCTION

In order to determine our heuristic EBL bias function

$$b(k) = \sqrt{\frac{P_{EBL}(k)}{P_{matter}(k)}}, \tag{5.7}$$

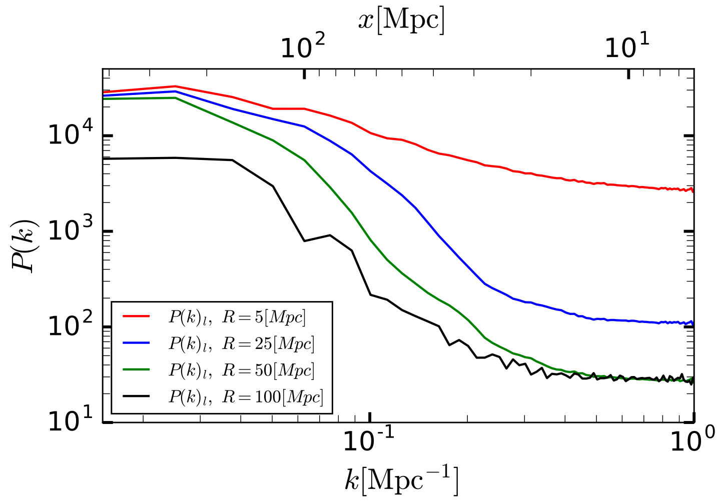

Figure 5.3: The power spectrum of the local EBL for four different radii 5, 25, 50, and 100 Mpc in red, blue, green, and black lines, respectively.

we employ the total EBL, i.e. including the light coming from galaxies beyond the radius of the spheres within which we determine the local EBL intensity directly. In accordance with the convergence study above, we use a light collecting radius of 50 Mpc and add a homogeneous background following Kudoda & Faltenbacher (2017), to get the total EBL at $z = 0$. A side effect of using a radius of 50 Mpc is that from a cosmological perspective the radius it is not large enough to necessitate the consideration of the retardation of light, i.e. we do not need to consider time delay of light arrival due to large distances.

Following the method described above, we use the total bolometric EBL to compute the power spectrum $p(k)_{EBL}$ at $z = 0$, which we then compare to the well established matter and the galaxy power spectrum. To determine the galaxy power spectrum, we compute the galaxies mass density contrast, by binning the mass of each galaxy in $(5\,\mathrm{Mpc/h})^3$ cells, and drive the 3D power spectrum of the masses of the galaxies $P(k)_g$. The top panel in figure 5.4 compares the EBL, galaxy, and total matter distribution power spectra, the EBL power spectrum is scaled by a factor of 10^4. Since the dark matter distribution for the MR7 is not publicly available, we have used the power spectrum by Smith et al. (2003). The authors used a cosmological N-body simulations to simulate the nonlinear evolution of the matter power spectrum.

The lower panel of figure 5.4 shows the scale dependent bias, $b(k)$, between the light distribution and the total mass distribution as a solid green line and

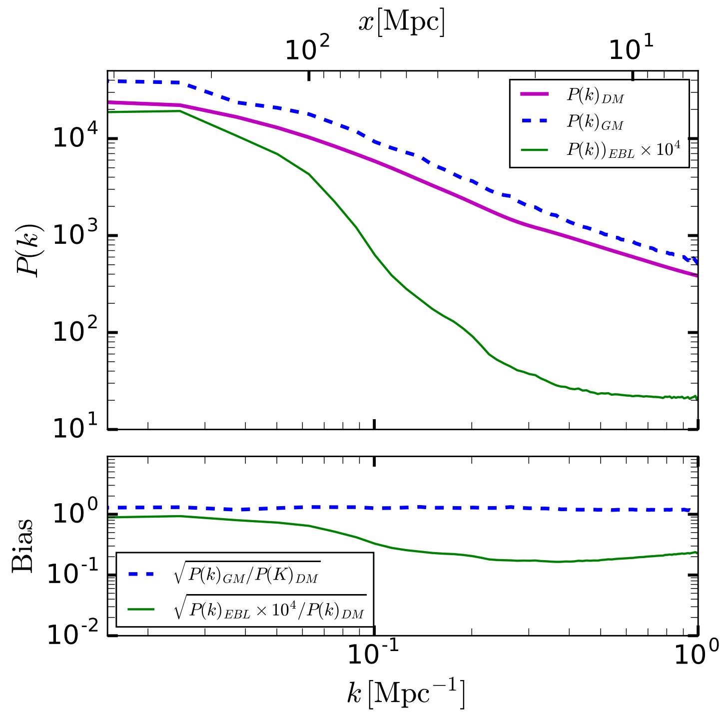

Figure 5.4: Top panel: the power spectrum expected by ΛCDM model (purple line), the power spectra for the galaxy and total EBL photon are in blue dashed-line and green line (multiplied by a factor of 10000), respectively. Bottom panel: show the bias between the galaxy distribution and dark matter (ΛCDM) in blue dashed line, and EBL and dark matter in green line.

between the galaxy masses distribution and the total mass distributions as a dashed blue line.

5.6 DISCUSSION AND CONCLUSION

Current EBL models usually assume that the EBL is homogeneous. As a consequence one expects the power spectrum associated with the EBL intensity distribution to be flat, i.e. showing the same amplitudes independent of wavenumber k. Computing the power spectrum based on a realistic EBL model which takes the contributions of individual galaxies within a cosmological simulation into account, we find that the amplitude of the fluctuation of the EBL is four to five order of magnitudes (less clustering and this almost homogeneous) less than the amplitude of the fluctuations on the corresponding matter distribution (see Fig. 5.4). At scales $\gtrsim 100\,\mathrm{Mpc}$ the EBL power spectrum is four orders of magnitude lower than the power spectrum of the large scale matter distribution. In addition, the slope of the EBL power spectrum is almost the same as the corresponding matter power spectrum at these scales. In contrast, on scales $\lesssim 10\,\mathrm{Mpc}$ the amplitudes of the EBL power spectrum are much smaller (roughly six orders of magnitude less) than those of the matter power spectrum. Moreover, the power spectrum at small scales is flat.

Here we have a strong negative bias which is a result of the $1/r^2$ profile of the light distribution about point sources (i.e. galaxies). The two regimes are connected by a steeply falling curve. Thus, we find that the EBL is clustered on very large scales in a similar way as the overall matter distribution and is much less clustered than the matter distribution on small scales.

The EBL power spectrum, as computed above, can be used to model the EBL photon distribution in a realistic manner including its fluctuations without having to model the underlying galaxy distribution. In practice, at first one would generate a random realization of the matter density based on the matter density power spectrum which is routinely done to set up cosmological N-body simulations. In a second step one would prune the individual amplitudes of the matter power spectrum according to the bias function displayed in Fig. 5.4. Finally, the Fourier transformation of the pruned amplitudes would give the EBL photon intensity field associated with the matter distribution of that particular realization. In particular, the EBL intensity associated with super-structures, such as large voids or super-clusters, is captured by this approach without the need for determining the underlying galaxy distribution.

The analysis presented so far shows the potential to increase our understanding of the connection between the EBL and the underlying matter distribution. In future, the increasing sensitivity of instruments may allow astronomers to observe the EBL fluctuations in a direct or indirect way. Then our analysis can serve as a cornerstone of the theoretical interpretation of the observations.

Chapter 6

CONCLUSION

The extragalactic background light (EBL), spanning from ultraviolet to infrared wavelengths, captures the redshifted radiation emitted from all stellar sources since the recombination era. Understanding the production and evolution of the EBL is crucial for many aspects of cosmology and astrophysics. For instance, for setting constraints on galaxy evolution models and the interpretation of γ-ray observations. This requires an accurate measurements of the EBL density. However, the faintness of the EBL (1% of the night sky brightness) in addition to foreground emission form our Galaxy and zodiacal light makes its direct measurement extremely challenging. Fortunately, we can indirectly constrain its density through analysis of the EBL fluctuations.

The EBL also plays a significant role in the propagation of high energy γ rays emitted from extragalactic sources (such as blazars). γ-ray photons interact with the EBL en-route to Earth, affecting number of photons observed. This interaction results in attenuation of the intrinsic γ-ray spectrum through pair-production, thereby causing the observed spectrum to differ significantly from the emitted one. The level of the attenuation of the γ-ray is strongly controlled by the intensity of the EBL along their way to the Earth. However, since the intrinsic VHE spectrum of blazars is still not fully understood, determining the EBL provides an indirect tool to shed light on their spectrum. Conversely, we can derive limits on the EBL density by assuming an intrinsic VHE spectrum.

In recent years, thanks to the advancement in detecting techniques (from ground and space), our knowledge of the γ-ray sky and high energy astrophysics has substantially improved. The increasing number of observed VHE sources provides us a bigger sample to study the signature of the EBL on their spectra (seen as steepening of the VHE spectrum). With an eye to the

Cherenkov Telescope Array (CTA) and other future γ-ray observations and also to galaxy surveys, an accurate determination of the EBL fluctuation may prove to be a powerful tool in cosmology to obtain insight into the workings of our Universe.

In this thesis I focus on modeling the fluctuations in the EBL density throughout the Universe, and on evaluation of the impact of the EBL fluctuations on the VHE γ-ray from cosmological sources. This study is divided in to three parts: first we look at the spatial EBL fluctuations in the Universe; second, the impact of structures close to the γ-ray path on the EBL fluctuation and thus the γ-ray opacity; last we investigate the correlation between the EBL distribution and the underlying matter.

In Chapter 1 I present the standard cosmological framework briefly and summarize the main ingredients of the formation and evolution of the Universe from the ΛCDM model point of view. I also discuss the different parts of the diffuse extragalactic background radiation spectrum.

In Chapter 2 of this thesis I provide an extensive review on the production, measurements, and modelling of the EBL and its use as a cosmological probe. I also provide a review of γ-ray astronomy: production, and interaction mechanisms, and astrophysical γ-ray sources. Special attention is given to Blazars, the most ubiquitous VHE source detected in the extragalactic sky, and their VHE γ-ray spectrum. Finally, I discuss the link between the EBL and the γ rays, and mention some of the challenges linking the EBL and VHE γ-ray astronomy.

In Chapter 3 I describe the EBL model that I developed extending the model proposed by Razzaque et al. (2009) in the range of (0.1 − 10 eV) to a full EBL spectrum in the range (0.001 − 10 eV) following the model by Finke et al. (2010). The new model implements the fluctuations in the EBL analytically based on the spatial fluctuations in the SFR that were derived from the semi-analytic galaxy catalog by Guo et al. (2013).

We find that the fluctuations of the SFR density in small volumes, 25 Mpc radius, can reach up to ±50% of the mean SFR density. By introducing the SFR upper and lower limits on the EBL model, we compute the respective upper and lower EBL density limits at different redshifts, which turns out to be small (±1%). We use the upper and lower EBL limits at different redshifts to compute the γ-ray transmissivity at different redshifts, and find that the variation in the transmissivity to minor. It turns out that spatial fluctuations of the EBL intensity have negligible impact on the transmissivity for γ-ray sources with $z < 0.5$ and $E_\gamma < 1\,\mathrm{TeV}$ ($\lesssim 2\%$). For higher energies and redshifts, however, we find increasing deviations from the mean transmissivity. For instance, sources at $z > 0.5$ with γ-ray energies $E_\gamma > 0.1\,\mathrm{TeV}$ show a change of up to $\pm 10\%$ in the transmissivity. However, the impact of the is transmissivity variation on the spectral index of the γ-ray spectrum is $\sim 1\%$. This leads to the conclusion that fluctuations in the EBL intensity have marginal impact on the slope of the spectra for the redshift range covered by the blazar sample considered here. From opacity calculations we see that the higher the γ-ray energies the higher the effect of the fluctuations.

In Chapter 4 I introduce a new EBL, hybrid, model, where we combine two modelling approaches: forward and semi-analytic. The goal is to study the impact of the stochastic effect of the large scale structures on the γ-ray path. In order to achieve this goal we construct ~ 1000 cosmological cylinders (γ-ray paths) with a thickness of 100 Mpc from $z = 0$ up to $z = 0.5$ using the MR7 galaxy catalog. The total EBL through these paths is computed in two steps the EBL within the cylinders (local) and a homogeneous background (using our previous EBL model (Kudoda & Faltenbacher, 2018)). We use the BC03 stellar library to assign different stellar spectrum for each galaxy in each cylinder according to its age and metallicities and employ their stellar mass for normalization. Thereafter, we use an empirical result to determine the dust absorption, and redistributed the dust absorbed energy into three black body spectra representing different dust populations. We use the inverse square law to compute the flux from all galaxies within 50 Mpc at the centre of the cylinders. At discrete points with $dz = 0.01$ through each cylinder are chosen to compute the local EBL. We add to each point (at $z = z_{point}$) the corresponding background spectrum (at $z = z_{point} + 0.1$). One order of magnitude difference between different cylinders at the same redshift is confirmed. However, when we added the background the differences become insignificant, because the background is three orders of magnitude higher than the local flux (within 50 Mpc spheres). Due to the minor difference in the EBL between the paths, the opacities (along all the paths) overlapped and no significant difference are found between the γ-ray paths.

In addition, I present an investigation of the effects of a close encounter between the γ-ray path and an intervening galaxy on the spectral index Γ of the VHE sources. This was done by inserting an artificial galaxy spectrum close to the γ-ray path. We studied the different scenarios by changing the distance from the γ-ray path (20, 40, 60 and 80 kpc) and the mass of the inserted galaxy between 5×10^6 $M_\odot$ and 5×10^{12} $M_\odot$. No significant effects were observed on Γ when the stellar mass of the intervening galaxy is less than 10^9 $M_\odot$. However, very high stellar mass galaxies could have a significant attenuation on the VHE spectral index even at distances of 50 kpc from the line-of-sight.

In Chapter 5 I investigate the EBL fluctuations in a different way from the previous two methods. In this method I determine the bolometric EBL density fluctuations in space and compute the 3D power spectrum of the EBL density contrast. Based on this the correlation with the underlying matter (dark matter) distribution in the Universe is investigated. For this, we follow the EBL model described in Chapter 4. Then we compute the local EBL using spheres distributed (in a grid of $100 \times 100 \times 100$) within MR7 simulation box at $z = 0$ (instead of light cones), to obtain the total EBL spectrum we add a homogeneous background to all grid points. The bolometric intensity is then computed by integrating these spectra over the energy. To quantify the relation between the distributions of the EBL and the underlying matter at different scales (k), we compute the bias between the power spectra of the EBL and the overall matter distribution as predicted by the ΛCDM model.

We confirm that the EBL is almost homogeneous, the amplitudes of the power spectrum are more than four orders of magnitude smaller compared to the amplitudes associated with the matter fluctuations. Thus the EBL shows a much lesser degree of clustering compared to the matter distribution in the universe. Regarding the scale dependence of the EBL power spectrum, we find that fluctuations on large scales ($\sim$ 100 Mpc) are two orders of magnitude larger than on small scales, i.e. $<$ 10 Mpc. On small scales the power spectrum is flat, implying a homogeneous distribution of the EBL photons which is caused by the $1/r^2$ profile about the light sources. The EBL power spectrum provides a realistic way to model the light distribution based on the outcome of N body dark matter simulations. This way, the matter and corresponding light distribution can be approximated without the need to model the light emitting galaxy distribution. If one is interested only in modelling the EBL including its fluctuations then the power spectrum can be used directly to generate a realization of the EBL.

6.1 FUTURE WORK

Although the work presented here provides a comprehensive analytical and numerical method to constrain and evaluate the EBL fluctuations, the small amplitudes of the EBL fluctuations and their effect of the VHE γ-ray spectrum from distant sources, is not enough to resolve the EBL crisis. Therefore, in the near future we plan to investigate the effects of the secondary γ-ray production from the first generation electron-positron pairs based on a Monte Carlo approach.

In detail, VHE γ rays from distant sources such as blazars or γ-ray bursts interact with the EBL photons, which on small scales are not distributed homogeneously. Since the cosmic electron density follows the large scale structure, it is expected that the production of secondary γ rays, by annihilation of a primary positrons for instance, will trace the large scale structure. Then, from an observational perspective, the size of the γ-ray halo around the primary source would allow us to make estimates of the integrated density along the path of the γ-ray. Pair production and electron-positron annihilation will be the main physical processes to consider in our Monte Carlo simulation which will use the EBL as computed in the first part as input data.

Bibliography

Abdalla H., Böttcher M., 2017, ApJ, 835, 237

Abdo A. A., et al., 2011a, ApJ, 726, 43

Abdo A. A., et al., 2011b, ApJ, 727, 129

Abdo A. A., et al., 2011c, ApJ, 736, 131

Abel T., Bryan G. L., Norman M. L., 2000, ApJ, 540, 39

Abel T., Bryan G. L., Norman M. L., 2002, Science, 295, 93

Abramowski A., H.E.S.S. Collaboration et al. 2013, A&A, 550, A4

Ackermann M., Ajello M., Allafort A., et al. 2011, ApJ, 743, 171

Ackermann M., et al., 2015, ApJ, 799, 86

Aharonian F. A., 2000, New A, 5, 377

Aharonian F., Akhperjanian A. G., et al. 2006, Nature, 440, 1018

Aharonian F., et al., 2007, A&A, 475, L9

Aharonian F. A., Khangulyan D., Costamante L., 2008, MNRAS, 387, 1206

Ajello M., et al., 2008, ApJ, 689, 666

Albert J., et al., 2008, Science, 320, 1752

Albrecht Unsöld B. B., 2002, The New Cosmos: An Introduction to Astronomy and Astrophysics, 5 edn. Springer-Verlag Berlin Heidelberg, http://gen.lib.rus.ec/book/index.php?md5=462b699cd52c1f39c4d73c26062d5166

Alexander J. K., Brown L. W., Clark T. A., Stone R. G., Weber R. R., 1969, ApJ, 157, L163

Alexander D. M., et al., 2003, AJ, 126, 539

Archambault S., et al., 2014, The Astrophysical Journal Letters, 785, L16

Arendt R. G., Dwek E., 2003, ApJ, 585, 305

Arendt R. G., et al., 1998, ApJ, 508, 74

Ashby M., et al., 2013, The Astrophysical Journal, 769, 80

Atwood W. B., et al., 2009, ApJ, 697, 1071

Bardeen J. M., Bond J. R., Kaiser N., Szalay A. S., 1986, ApJ, 304, 15

Barnacka A., Böttcher M., Sushch I., 2014, ApJ, 790, 147

Bartelmann M., 2008, in Röser S., ed., Reviews in Modern Astronomy Vol. 20, Reviews in Modern Astronomy. p. 92, doi:10.1002/9783527622993.ch5

Baugh C., 2000, Correlation Function and Power Spectra in Cosmology. Bristol: Institute of Physics Publishing, p. 2136, doi:10.1888/0333750888/2136

Baugh C. M., Lacey C. G., Frenk C. S., Granato G. L., Silva L., Bressan A., Benson A. J., Cole S., 2005, MNRAS, 356, 1191

Beckmann V., Shrader C. R., 2012, Active Galactic Nuclei. John Wiley & Sons

Beichman C. A., Helou G., 1991, ApJ, 370, L1

Bernstein R., 2000, Extragalactic Background Light. Bristol: Institute of Physics Publishing, p. 2639, doi:10.1888/0333750888/2639

Bernstein R. A., 2007, ApJ, 666, 663

Bernstein R. A., Freedman W. L., Madore B. F., 2002a, ApJ, 571, 56

Bernstein R. A., Freedman W. L., Madore B. F., 2002b, ApJ, 571, 85

Bernstein R. A., Freedman W. L., Madore B. F., 2002c, ApJ, 571, 107

Berta S., et al., 2011, A&A, 532, A49

Béthermin M., Dole H., Beelen A., Aussel H., 2010, A&A, 512, A78

Béthermin M., et al., 2012, A&A, 542, A58

Bhat P. N., 1999, International Cosmic Ray Conference, 5, 191

Bhattacharya D., et al., 1997, in Dermer C. D., Strickman M. S., Kurfess J. D., eds, American Institute of Physics Conference Series Vol. 410, Proceedings of the Fourth Compton Symposium. pp 1626–1630, doi:10.1063/1.54023

Bignami G. F., et al., 1975, Space Science Instrumentation, 1, 245

Biller S. D., et al., 1998, Physical Review Letters, 80, 2992

Blain A. W., Longair M. S., 1993, MNRAS, 264, 509

Blain A. W., Jameson A., Smail I., Longair M. S., Kneib J.-P., Ivison R. J., 1999, MNRAS, 309, 715

Blandford R. D., Levinson A., 1995, ApJ, 441, 79

Blumenthal G. R., Gould R. J., 1970, Reviews of Modern Physics, 42, 237

Bond J. R., Carr B. J., Hogan C. J., 1986, ApJ, 306, 428

Böttcher M., Reimer A., Marscher A. P., 2009, ApJ, 703, 1168

Breit G., Wheeler J. A., 1934, Phys. Rev., 46, 1087

Bridle A. H., 1967, MNRAS, 136, 219

Bromm V., Coppi P. S., Larson R. B., 1999, ApJ, 527, L5

Brown T. M., Kimble R. A., Ferguson H. C., Gardner J. P., Collins N. R., Hill R. S., 2000, AJ, 120, 1153

Bruzual G., Charlot S., 2003, MNRAS, 344, 1000

Burrows A., Liebert J., 1993, Reviews of Modern Physics, 65, 301

Calzetti D., Heckman T. M., 1999, ApJ, 519, 27

Calzetti D., Armus L., Bohlin R. C., Kinney A. L., Koornneef J., Storchi-Bergmann T., 2000, ApJ, 533, 682

Cen R., Ostriker J. P., 1993, ApJ, 417, 415

Chabrier G., 2003, PASP, 115, 763

Charlot S., Fall S. M., 2000, ApJ, 539, 718

Chary R., Elbaz D., 2001, ApJ, 556, 562

Clark T. A., Brown L. W., Alexander J. K., 1970, Nature, 228, 847

Coil A. L., Hennawi J. F., Newman J. A., Cooper M. C., Davis M., 2007, ApJ, 654, 115

Cole S., Aragon-Salamanca A., Frenk C. S., Navarro J. F., Zepf S. E., 1994, MNRAS, 271, 781

Cole S., Lacey C. G., Baugh C. M., Frenk C. S., 2000, MNRAS, 319, 168

Cole S., Norberg P., Baugh C. M., et al. F., 2001, MNRAS, 326, 255

Coles P., Erdogdu P., 2007, J. Cosmology Astropart. Phys., 10, 007

Conselice C. J., 2003, ApJS, 147, 1

Cortina J., Goebel F., Schweizer T., for the MAGIC Collaboration 2009, arXiv e-prints,

Costamante L., 2013, International Journal of Modern Physics D, 22, 30025

Dale D. A., Helou G., 2002, ApJ, 576, 159

Davis M., Efstathiou G., Frenk C. S., White S. D. M., 1985, ApJ, 292, 371

De Lucia G., Blaizot J., 2007, MNRAS, 375, 2

Derdeyn S. M., Ehrmann C. H., Fichtel C. E., Kniffen D. A., Ross R. W., 1972, Nuclear Instruments and Methods, 98, 557

Dermer C. D., 2007, in Ritz S., Michelson P., Meegan C. A., eds, American Institute of Physics Conference Series Vol. 921, The First GLAST Symposium. pp 122–126 (arXiv:0704.2888), doi:10.1063/1.2757282

Dermer C. D., Schlickeiser R., 1993, ApJ, 416, 458

Dermer C. D., Schlickeiser R., Mastichiadis A., 1992, A&A, 256, L27

Dermer C. D., Sturner S. J., Schlickeiser R., 1997, ApJS, 109, 103

Desert F.-X., Boulanger F., Puget J. L., 1990, A&A, 237, 215

Devriendt J. E. G., Guiderdoni B., 2000, A&A, 363, 851

Devriendt J. E. G., Guiderdoni B., Sadat R., 1999, A&A, 350, 381

Díaz A. D., 2011, PhD thesis, University of Seville

Dicke R. H., Peebles P. J. E., Roll P. G., Wilkinson D. T., 1965, ApJ, 142, 414

Domínguez A. e. a., 2011, MNRAS, 410, 2556

Domínguez A., Sánchez-Conde M. A., Prada F., 2011, J. Cosmology Astropart. Phys., 11, 020

Driver S. P., Popescu C. C., Tuffs R. J., Graham A. W., Liske J., Baldry I., 2008, ApJ, 678, L101

Dube R. R., Wickes W. C., Wilkinson D. T., 1979, ApJ, 232, 333

Dwek E., 1998, ApJ, 501, 643

Dwek E., 2001, in "The Extragalactic Infrared Background and its Cosmological Implications". p. 389

Dwek E., Arendt R. G., 1998, ApJ, 508, L9

Dwek E., Krennrich F., 2005, ApJ, 618, 657

Dwek E., Krennrich F., 2013, Astroparticle Physics, 43, 112

Dwek E., Slavin J., 1994, ApJ, 436, 696

Dwek E., et al. 1998, ApJ, 508, 106

Edelstein J., Bowyer S., Lampton M., 2000, ApJ, 539, 187

Eggleton P. P., Fitchett M. J., Tout C. A., 1989, ApJ, 347, 998

Einstein A., 1915, Sitzungsberichte der Königlich Preußischen Akademie der Wissenschaften (Berlin), Seite 778-786.,

Essey W., Kusenko A., 2010, Astroparticle Physics, 33, 81

FRAS M. R., 2007, State of The Universe 2007: New Images, Discoveries and Events, 1 edn. Springer Praxis Books, Springer-Verlag New York, `http://gen.lib.rus.ec/book/index.php?md5=c221971901219a55b8deccb4c97d2de8`

Fall S. M., Efstathiou G., 1980, MNRAS, 193, 189

Fazio G. G., Stecker F. W., 1970, Nature, 226, 135

Fermi LAT Collaboration 2010, ApJ, 720, 435

Fields B. D., Pavlidou V., Prodanović T., 2010, ApJ, 722, L199

Finkbeiner D. P., Davis M., Schlegel D. J., 2000, ApJ, 544, 81

Finke J. D., Razzaque S., Dermer C. D., 2010, The Astrophysical Journal, 712, 238

Fixsen D. J., Dwek E., Mather J. C., Bennett C. L., Shafer R. A., 1998, ApJ, 508, 123

Fontanot F., Somerville R. S., 2011, MNRAS, 416, 2962

Fontanot F., Monaco P., Silva L., Grazian A., 2007, MNRAS, 382, 903

Fontanot F., Somerville R. S., Silva L., Monaco P., Skibba R., 2009, MNRAS, 392, 553

Franceschini A., Mazzei P., de Zotti G., Danese L., 1994, ApJ, 427, 140

Friedmann A., 1922, Zeitschrift fur Physik, 10, 377

Funk B., Magnussen N., Meyer H., Rhode W., Westerhoff S., Wiebel-Sooth B., 1998, Astroparticle Physics, 9, 97

Furniss A., et al., 2013, ApJ, 768, L31

Furniss A., Sutter P. M., Primack J. R., Domínguez A., 2015, MNRAS, 446, 2267

Gardner J. P., Brown T. M., Ferguson H. C., 2000, ApJ, 542, L79

Gehrels N., Fichtel C. E., Fishman G. J., Kurfess J. D., Schonfelder V., 1993, Scientific American, 269, 68

Ghisellini G., Madau P., 1996, MNRAS, 280, 67

Giacconi R., Gursky H., Paolini F. R., Rossi B. B., 1962, Physical Review Letters, 9, 439

Giacconi R., et al., 2002, ApJS, 139, 369

Gilmore R. C., Madau P., Primack J. R., Somerville R. S., 2008, in Aharonian F. A., Hofmann W., Rieger F., eds, American Institute of Physics Conference Series Vol. 1085, American Institute of Physics Conference Series. pp 577–580 (`arXiv:0811.1984`), doi:10.1063/1.3076738

Gilmore R. C., Somerville R. S., Primack J. R., Domínguez A., 2012, Monthly Notices of the Royal Astronomical Society, 422, 3189

Gordon K. D., Misselt K. A., Witt A. N., Clayton G. C., 2001, ApJ, 551, 269

Gould R. J., Schréder G. P., 1967, Physical Review, 155, 1404

Granato G. L., Lacey C. G., Silva L., Bressan A., Baugh C. M., Cole S., Frenk C. S., 2000, ApJ, 542, 710

Guiderdoni B., Rocca-Volmerange B., 1987, A&A, 186, 1

Guiderdoni B., Hivon E., Bouchet F. R., Maffei B., 1998, MNRAS, 295, 877

Gunn J. E., Gott III J. R., 1972, ApJ, 176, 1

Guo Q., White S., Angulo R. E., Henriques B., Lemson G., Boylan-Kolchin M., Thomas P., Short C., 2013, MNRAS, 428, 1351

Guy J., Renault C., Aharonian F. A., Rivoal M., Tavernet J.-P., 2000, A&A, 359, 419

Haarsma D. B., Partridge R. B., 1998, ApJ, 503, L5

Hacking P. B., Soifer B. T., 1991, ApJ, 367, L49

Harris J., Chadwick P. M., 2014, J. Cosmology Astropart. Phys., 10, 018

Hasinger G., 2004, Nuclear Physics B Proceedings Supplements, 132, 86

Hauser M. G., 1995, in Calzetti D., Livio M., Madau P., eds, Extragalactic Background Radiation Meeting. pp 135–144

Hauser M. G., Dwek E., 2001, Acta Astron., 39, 249

Helou G., 1991, in Duric N., Crane P. C., eds, Astronomical Society of the Pacific Conference Series Vol. 18, The Interpretation of Modern Synthesis Observations of Spiral Galaxies. pp 125–133

Hermann G., 1997, in Giraud-Heraud Y., Tran Thanh van J., eds, Very High Energy Phenomena in the Universe; Moriond Workshop. p. 141

Hogg D. W., 1999, arXiv e-prints, pp astro–ph/9905116

Hopkins A. M., Beacom J. F., 2006, ApJ, 651, 142

Hopkins A. M., Irwin M. J., Connolly A. J., 2001, ApJ, 558, L31

Hopwood R., et al., 2010, ApJ, 716, L45

Horns D., Meyer M., 2012, J. Cosmology Astropart. Phys., 2, 033

Hubble E., 1929, Proceedings of the National Academy of Science, 15, 168

Kaiser N., 1984, ApJ, 284, L9

Kashlinsky A., 2005, Phys. Rep., 409, 361

Kashlinsky A., Odenwald S., 2000, ApJ, 528, 74

Kashlinsky A., Mather J. C., Odenwald S., Hauser M. G., 1996a, in Dwek E., ed., American Institute of Physics Conference Series Vol. 348, American Institute of Physics Conference Series. pp 115–121 (arXiv:astro-ph/9604180)

Kashlinsky A., Mather J. C., Odenwald S., Hauser M. G., 1996b, ApJ, 470, 681

Kashlinsky A., Mather J. C., Odenwald S., 1996c, ApJ, 473, L9

Kashlinsky A., Arendt R. G., Ashby M. L. N., Fazio G. G., Mather J., Moseley S. H., 2012, ApJ, 753, 63

Kashlinsky A., Arendt R. G., Atrio-Barandela F., Cappelluti N., Ferrara A., Hasinger G., 2018, Reviews of Modern Physics, 90, 025006

Kauffmann G., White S. D. M., Guiderdoni B., 1993, MNRAS, 264, 201

Kauffmann G., Colberg J. M., Diaferio A., White S. D. M., 1999, MNRAS, 303, 188

Kawada M., et al., 1994, ApJ, 425, L89

Keenan R. C., Barger A. J., Cowie L. L., Wang W.-H., 2010, ApJ, 723, 40

Kelner S. R., Aharonian F. A., Bugayov V. V., 2006, Phys. Rev. D, 74, 034018

Kelsall T., Weiland J. L., et al. 1998, ApJ, 508, 44

Kennicutt Jr. R. C., 1998, ARA&A, 36, 189

Kennicutt Jr. R. C., Chu Y.-H., 1988, AJ, 95, 720

Kneiske T. M., Bretz T., Mannheim K., Hartmann D. H., 2004, A&A, 413, 807

Krennrich F., et al., 2002, ApJ, 575, L9

Krennrich F., et al., 2004, New A Rev., 48, 345

Kudoda A. M., 2015, Master's thesis, School of Physics, University of the Witwatersrand

Kudoda A. M., Faltenbacher A., 2016, PoS, HEASA2015, 020

Kudoda A. M., Faltenbacher A., 2017, MNRAS, 467, 2896

Kudoda A. M., Faltenbacher A., 2018, MNRAS, 481, 405

Kushwaha P., Sahayanathan S., Lekshmi R., Singh K. P., Bhattacharyya S., Bhattacharya D., 2014, MNRAS, 442, 131

Lacey C., Guiderdoni B., Rocca-Volmerange B., Silk J., 1993, ApJ, 402, 15

Lagache G., et al., 2004, ApJS, 154, 112

Lagache G., Puget J.-L., Dole H., 2005, ARA&A, 43, 727

Leinert C., et al., 1998, A&AS, 127, 1

Lemaître G., 1927, Annales de la Société Scientifique de Bruxelles, 47, 49

Lemaître G., 1931, MNRAS, 91, 483

Lemson G., Virgo Consortium t., 2006, ArXiv Astrophysics e-prints,

Levenson L. R., Wright E. L., Johnson B. D., 2007, ApJ, 666, 34

Longair M. S., 1995, in Calzetti D., Livio M., Madau P., eds, Extragalactic Background Radiation Meeting. pp 223–236

Longair M. S., 2011, High Energy Astrophysics. Volume 1: Particles, photons and their detection, 3rd edn. Cambridge University Press

Lonsdale C. J., 1995, in Calzetti D., Livio M., Madau P., eds, Extragalactic Background Radiation Meeting. pp 145–167

MacCallum G. F. R. E. R. M. M. A. H., 2012, Relativistic cosmology. Cambridge University Press, http://gen.lib.rus.ec/book/index.php?md5=23501bafe2640754dd03841be2ca3c87

Madau P., Pozzetti L., 2000, MNRAS, 312, L9

Madau P., Ferguson H. C., Dickinson M. E., Giavalisco M., Steidel C. C., Fruchter A., 1996, MNRAS, 283, 1388

Malkan M. A., Stecker F. W., 1998, ApJ, 496, 13

Maraschi L., Ghisellini G., Celotti A., 1992, ApJ, 397, L5

Maraston C., 2005, MNRAS, 362, 799

Marscher A. P., Gear W. K., 1985, ApJ, 298, 114

Martin C., Hurwitz M., Bowyer S., 1991, ApJ, 379, 549

Matsuhara H., et al., 2000, A&A, 361, 407

Matsumoto T., Hayakawa S., Matsuo H., Murakami H., Sato S., Lange A. E., Richards P. L., 1988, ApJ, 329, 567

Matsumoto T., et al., 2005, ApJ, 626, 31

Matsuoka Y., Ienaka N., Kawara K., Oyabu S., 2011, ApJ, 736, 119

Matsuura S., et al., 2011, ApJ, 737, 2

Mattila K., 1990, in Bowyer S., Leinert C., eds, IAU Symposium Vol. 139, The Galactic and Extragalactic Background Radiation. pp 257–268

Mattila K., 2003, The Astrophysical Journal, 591, 119

Mazin D., Raue M., 2007, A&A, 471, 439

McDonald P., Scherrer R. J., Walker T. P., 2001, Phys. Rev. D, 63, 023001

Miller G. E., Scalo J. M., 1979, ApJS, 41, 513

Mirzoyan R., et al., 1994, Nuclear Instruments and Methods in Physics Research A, 351, 513

Mo H., van den Bosch F. C., White S., 2010, Galaxy Formation and Evolution. "Cambridge University Press"

Moore B., Katz N., Lake G., Dressler A., Oemler A., 1996, Nature, 379, 613

Mücke A., Protheroe R. J., 2001, Astroparticle Physics, 15, 121

Mücke A., Engel R., Rachen J. P., Protheroe R. J., Stanev T., 2000, Computer Physics Communications, 124, 290

Murthy J., Hall D., Earl M., Henry R. C., Holberg J. B., 1999, ApJ, 522, 904

Odegard N., Arendt R. G., Dwek E., Haffner L. M., Hauser M. G., Reynolds R. J., 2007, ApJ, 667, 11

Olive K. A., Steigman G., Walker T. P., 2000, Phys. Rep., 333, 389

Orr M. R., Krennrich F., Dwek E., 2011, ApJ, 733, 77

Padovani P., Giommi P., 1995, ApJ, 444, 567

Peacock J. A., 1995, in Calzetti D., Livio M., Madau P., eds, Extragalactic Background Radiation Meeting. pp 237–258

Peebles P. J. E., 1993, Principles of Physical Cosmology. Princeton University Press

Pei Y. C., Fall S. M., 1995, ApJ, 454, 69

Pei Y. C., Fall S. M., Hauser M. G., 1999, ApJ, 522, 604

Pénin A., et al., 2012, A&A, 543, A123

Pieri L., Bertone G., Branchini E., 2008, MNRAS, 384, 1627

Planck Collaboration et al., 2014a, A&A, 571, A15

Planck Collaboration et al., 2014b, A&A, 571, A16

Porciani C., Magliocchetti M., Norberg P., 2004, MNRAS, 355, 1010

Prialnik D., 2000, An introduction to the theory of stellar structure and evolution. Cambridge University Press, http://gen.lib.rus.ec/book/index.php?md5=de5463fe63fdbb8a89d04f33a5b9ac58

Primack J. R., Bullock J. S., Somerville R. S., MacMinn D., 1999, Astroparticle Physics, 11, 93

Primack J. R., Bullock J. S., Somerville R. S., 2005, in Aharonian F. A., Völk H. J., Horns D., eds, American Institute of Physics Conference Series Vol. 745, High Energy Gamma-Ray Astronomy. pp 23–33 (arXiv:astro-ph/0502177), doi:10.1063/1.1878394

Purton C. R., 1966, MNRAS, 133, 463

Rachen J. P., Mészáros P., 1998, Phys. Rev. D, 58, 123005

Razzaque S., Dermer C. D., Finke J. D., 2009, The Astrophysical Journal, 697, 483

Rieke G. H., Alonso-Herrero A., Weiner B. J., Pérez-González P. G., Blaylock M., Donley J. L., Marcillac D., 2009, ApJ, 692, 556

Roach F. E., Gordon J. L., 1973, The Light of the Night Sky. D. Reidel Publishing Companym, P.O. Box 17 Dordrecht Holland

Rodighiero G., et al., 2010, A&A, 515, A8

Ross N. P., et al., 2009, ApJ, 697, 1634

Rowan-Robinson M., 2001, New A Rev., 45, 631

Rowan-Robinson M., Hughes J., Vedi K., Walker D. W., 1990, MNRAS, 246, 273

Rybicki G. B., Lightman A. P., 1985, Radiative processes in astrophysics.. John Wiley

Saha L., 2014, PhD thesis, Homi Bhabha National Institute

Salpeter E. E., 1955, ApJ, 121, 161

Santos M. R., Bromm V., Kamionkowski M., 2002, MNRAS, 336, 1082

Saslaw W. C., Zipoy D., 1967, Nature, 216, 976

Schmidt M., et al., 1998, A&A, 329, 495

Schneider R., Ferrara A., Natarajan P., Omukai K., 2002, ApJ, 571, 30

Schroedter M., 2005, ApJ, 628, 617

Sepp T., Gramann M., 2013, arXiv e-prints,

Shectman S. A., 1973, ApJ, 179, 681

Shectman S. A., 1974, ApJ, 188, 233

Siegal-Gaskins J. M., Reesman R., Pavlidou V., Profumo S., Walker T. P., 2011, MNRAS, 415, 1074

Sikora M., Begelman M. C., Rees M. J., 1994, ApJ, 421, 153

Silva L., Granato G. L., Bressan A., Danese L., 1998, ApJ, 509, 103

Simon A. J. B., 1977, MNRAS, 180, 429

Sinha A., Sahayanathan S., Misra R., Godambe S., Acharya B. S., 2014, ApJ, 795, 91

Smith R. E., et al., 2003, MNRAS, 341, 1311

Somerville R. S., Primack J. R., 1999, MNRAS, 310, 1087

Somerville R. S., Primack J. R., Faber S. M., 2001, MNRAS, 320, 504

Somerville R. S., Hopkins P. F., Cox T. J., Robertson B. E., Hernquist L., 2008, MNRAS, 391, 481

Somerville R. S., Gilmore R. C., Primack J. R., Domínguez A., 2012, MNRAS, 423, 1992

Spitzer Jr. L., 1978, JRASC, 72, 349

Spitzer Jr. L., Baade W., 1951, ApJ, 113, 413

Springel V., Hernquist L., 2002, Monthly Notices of the Royal Astronomical Society, 333, 649

Stanev T., Franceschini A., 1998, ApJ, 494, L159

Stecker F. W., de Jager O. C., Salamon M. H., 1992, ApJ, 390, L49

Stecker F. W., de Jager O. C., Salamon M. H., 1996, ApJ, 473, L75

Stecker F. W., Malkan M. A., Scully S. T., 2006, ApJ, 648, 774

Stecker F. W., Scully S. T., Malkan M. A., 2016, ApJ, 827, 6

Strauss M. A., Frenk C. S., Matarrese S., Pen U.-L., 2000, in Courteau S., Willick J., eds, Astronomical Society of the Pacific Conference Series Vol. 201, Cosmic Flows Workshop. p. 371

Strong A. W., Moskalenko I. V., Reimer O., 2000, ApJ, 537, 763

Tan J. C., Silk J., Balland C., 1999, ApJ, 522, 579

Tavecchio F., Bonnoli G., 2016, A&A, 585, A25

Tavecchio F., Roncadelli M., Galanti G., 2015, Physics Letters B, 744, 375

Teplitz H. I., et al., 2011, AJ, 141, 1

Toller G. N., 1983, ApJ, 266, L79

Toomre A., Toomre J., 1972, ApJ, 178, 623

Totani T., Yoshii Y., Maihara T., Iwamuro F., Motohara K., 2001, ApJ, 559, 592

Urry C. M., Padovani P., 1995, PASP, 107, 803

Vassiliev V. V., 2000, Astroparticle Physics, 12, 217

Wall J. V., 1990, in Bowyer S., Leinert C., eds, IAU Symposium Vol. 139, The Galactic and Extragalactic Background Radiation. pp 327–332

Weekes T. C., et al., 1989, ApJ, 342, 379

Weidenspointner G., 1999, PhD thesis, Technical University of Munich

Weinberg S., 1972, Gravitation and Cosmology: Principles and Applications of the General Theory of Relativity. John Wiley

Worsley M. A., et al., 2005, MNRAS, 357, 1281

Xu C., 2000, ApJ, 541, 134

Xu C. K., et al., 2005, The Astrophysical Journal Letters, 619, L95

Yoshii Y., Takahara F., 1988, ApJ, 326, 1

Younger J. D., Hopkins P. F., 2011, MNRAS, 410, 2180

Yuan Q., Huang H.-L., Bi X.-J., Zhang H.-H., 2012, preprint, (arXiv:1212.5866)

Zamorani G., 1995, in Calzetti D., Livio M., Madau P., eds, Extragalactic Background Radiation Meeting. pp 37–50

Zemcov M., Blain A., Halpern M., Levenson L., 2010, The Astrophysical Journal, 721, 424